Mechanical Engineering Series

Hamid Arastoopour
Dimitri Gidaspow
Emad Abbasi

Computational Transport Phenomena of Fluid-Particle Systems

Springer

Mechanical Engineering Series

Series editor
Francis A. Kulacki
Department of Mechanical Engineering, University of Minnesota,
Minneapolis, Minnesota, USA

More information about this series at http://www.springer.com/series/1161

The Mechanical Engineering Series presents advanced level treatment of topics on the cutting edge of mechanical engineering. Designed for use by students, researchers and practicing engineers, the series presents modern developments in mechanical engineering and its innovative applications in applied mechanics, bioengineering, dynamic systems and control, energy, energy conversion and energy systems, fluid mechanics and fluid machinery, heat and mass transfer, manufacturing science and technology, mechanical design, mechanics of materials, micro- and nano-science technology, thermal physics, tribology, and vibration and acoustics. The series features graduate-level texts, professional books, and research monographs in key engineering science concentrations.

Hamid Arastoopour • Dimitri Gidaspow
Emad Abbasi

Computational Transport Phenomena of Fluid-Particle Systems

Springer

Hamid Arastoopour
Wanger Institute for Sustainable Energy Research (WISER)
Illinois Institute of Technology
Chicago, IL, USA

Dimitri Gidaspow
Department of Chemical and Biological Engineering
Illinois Institute of Technology
Chicago, IL, USA

Emad Abbasi
Senior R&D Scientist
Honeywell UOP
Des Plaines, IL, USA

Editor
Margaret M. Murphy
Wanger Institute for Sustainable Energy Research (WISER)
Illinois Institute of Technology
Chicago, IL, USA

ISSN 0941-5122 ISSN 2192-063X (electronic)
Mechanical Engineering Series
ISBN 978-3-319-45488-7 ISBN 978-3-319-45490-0 (eBook)
DOI 10.1007/978-3-319-45490-0

Library of Congress Control Number: 2016962658

Printed on acid-free paper

This Springer imprint is published by Springer Nature
The registered company is Springer International Publishing AG
The registered company address is: Gewerbestrasse 11, 6330 Cham, Switzerland

Preface

The widespread application of transport phenomena of fluid-particle systems and fluidization in industry demands an increase in efficiency and the development of predictive numerical simulations of industrial processes for design and scale-up purposes. In spite of today's advances in computational capability, considerable challenges remain due to the complexity of processes based on fluid-particle flow that require mass, momentum, and energy analyses at the molecular, particle, and process scales. This book is intended to address some of these issues and provide fundamental knowledge and needed design and scale-up tools for graduate students in different branches of science and engineering (i.e., chemical, biological, mechanical, and environmental engineers, etc.) and scientists and engineers already working in areas related to fluid-particle flow systems.

Prior to 1978, research in fluid-particle systems was mainly focused on the development of overall flow measurements and empirical correlation for the main flow parameters. However, during the last three decades, extraordinary advances have been made in the multiphase approach to fluid-particle flow systems that have significantly impacted our approach in the design and scale-up of processes based on fluid-particle transport phenomena. The first attempts in developing Eulerian/Eulerian modeling of fluid-particle systems and fluidization began in the 1960s by J. Davidson, R. Jackson, and S.L. Soo. During the 1980s, several attempts were made in the literature by Illinois Institute of Technology (IIT) researchers and others to obtain a numerical solution for a one-dimensional flow equation and to simulate flow in a vertical pneumatic conveying system. Later, IIT researchers considered each particle size as a separate phase, developed an experimentally verified particle-particle collision theory, introduced it in one-dimensional equations, and successfully compared the calculated flow parameters with experimental data for flow in dilute gas-particle systems. This probably motivated several investigators to develop a theory of particle interaction and collision based on the Chapman and Cowling kinetic theory approach. The kinetic theory approach, which is based on the oscillation of the particles, uses a granular temperature equation to determine the turbulent kinetic energy of the particles, assumes a distribution

function for instantaneous particle velocity, and defines a constitutive equation based on particle collision, interaction, and fluctuation. In fact, the kinetic theory approach for granular flow allows the determination of, for example, particle phase stress, pressure, and viscosity in place of the empirical equations. After this developmental stage of granular theory, there have been several modifications to the constitutive equations such as extension of the kinetic theory for granular flow for mixtures of multi-type particles. However, in a more concentrated fluid-particle flow system, not only should the flow be characterized by a two- or three-dimensional flow equation, but also the formation of large structures such as clusters should be included in modeling of transport phenomena of such flow systems. To solve these microscopic two-fluid model equations, very small grid sizes of less than a few particle diameter are needed. For most processes of practical interest, such fine spatial grids and small time steps require significant computational time. Thus, the effect of the large-scale structures using coarse grids must be accounted for by using approaches such as filtering equations or energy minimization multi-scale (EMMS).

To account for continuous variation in particle property distribution due to phenomena such as chemical reaction, agglomeration, breakage, attrition, and growth at significantly less required computational time, a new approach to solve population balance equations (PBEs) linked with computational fluid dynamics (CFD) is needed. The PBE is a balance equation based on the number density function that accounts for the spatial and temporal evolutions of the particulate phase internal variable distribution function in a single control volume. This equation is an integro-differential equation that involves both integrals and derivatives of the distribution function. The most promising method of solution at the present time to solve CFD-PBE is the method of moments, which is based on solving the distribution function transport equation in terms of its lower-order moments. Some of the variables in PBE need to be calculated from the CFD model, and, in turn, solution of the PBE gives some of the phase properties needed in the CFD model. Therefore, PBE and CFD need to cross-talk via a two-way coupling.

Another approach to simulate a gas-particle flow system is the distinct element method (DEM), which is based on an equation of motion for each individual particle. Thus, in principle, individual particle size, shape, and density can be introduced directly into the governing equations. However, this approach requires huge computational time in simulating commercial-scale processes, which is not the focus of this book.

This book provides a comprehensive approach to address the abovementioned challenges and issues and presents fundamental knowledge and needed design and scale-up tools for gas-solid flows at different flow regimes.

Chapter 1 deals with the derivation of the basic governing equations for conservation of mass, momentum, and energy for multiphase systems.

Chapter 2 provides continuity and momentum conservation equations and constitutive and boundary conditions for fluid-particle flow systems. The conservation equations and constitutive relations are general and can be applied to all regimes of

fluid-particle flow, from a very dilute particle volume fraction to the packed bed regime. The fundamentals of the kinetic theory approach for derivation of constitutive equations for the regimes when particle collision is dominant and the frictional behavior of particles based on soil mechanics principles for dense particle flow are discussed. In addition, the kinetic theory approach has been extended to multi-type particulate flows. Finally, the generalized forms of governing equations and constitutive relations for all particle phase flow regimes are presented in Tables 2.1 and 2.2.

Chapter 3 deals with the effects of the presence of particle clusters in fluid-particle flow modeling and numerical simulation. This chapter also introduces key concepts and the fundamental derivations of two approaches for considering the presence of clusters and large structures that have gained significant attention in the literature: the filtering or subgrid model and the energy minimization multi-scale (EMMS) model. Using these approaches results in simulations that require a manageable computational time.

Chapter 4 provides an introduction to the concept of polydispersity in multiphase systems and the numerical solution of coupled CFD and PBE. Solutions based on the different method of moments (MOM) are also presented, and the finite size domain complete set of trial functions method of moments (FCMOM) and the implementation of FCMOM in a CFD code are discussed in more detail. Finally, the application of FCMOM for three processes of linear growth, homogeneous aggregation, and non-homogeneous aggregation in emulsion flow is presented.

Chapter 5 presents three case studies. Case 1 is CFD modeling and simulation of a pharmaceutical bubbling bed drying process. Case 2 is CFD modeling and simulation of a reactive gas-solid system in the riser section of a circulating fluidized bed (CFB) reactor representing a CO_2 capture process using solid sorbents. Case 3 is similar to Case 2, but with one difference: the density distribution of the solid phase is changing due to chemical reactions.

The authors greatly appreciate several individuals who contributed in different ways to the completion of this book. In particular, the authors would like to acknowledge the original contributions of the following: Professor Matteo Strumendo of Università degli Studi di Padova in development of FCMOM for solution of PBE, Dr. Hadjira Iddir of Universal Oil Products (UOP) for the development of modeling of multi-type particle flow using the kinetic theory approach, Dr. Emad Ghadirian of Gamma Technologies for his contribution in the energy minimization multi-scale (EMMS) approach and formulation of frictional pressure and viscosity for dense particle flow, Dr. Sofiane Benyahia of National Energy Technology Laboratory (NETL) for his contribution to the simulation of gas-solid flows, Dr. Jungkee Jang for the development of the modeling and numerical simulation for the drying process, and Dr. Javad Abbasian for his contribution in the development of rate of reaction for CO_2 sorption.

The research conducted by the authors that is presented in this book is mainly funded by the US Department of Energy. The support and use of the computational facilities of Wanger Institute for Sustainable Energy Research (WISER) of Illinois Institute of Technology (IIT) significantly contributed to the success of the

simulation results presented in this book. The authors would like to thank and greatly appreciate Ms. Margaret M. Murphy, IIT WISER assistant director and program outreach manager, for editing this book.

Chicago, IL, USA Hamid Arastoopour
Chicago, IL, USA Dimitri Gidaspow
Des Plaines, IL, USA Emad Abbasi

Contents

Chapter 1
Conservation Laws for Multiphase Flow

1.1 Introduction

Based on the continuum theory, conservation laws for mass, momentum, and energy for disperse multiphase flow can be derived using the Reynolds transport theorem, as illustrated by Gidaspow (1994). For multiphase flow systems, the only new concept in this approach is the introduction of phasic volume fraction, ε_i. For a single-phase system, $\varepsilon = 1$, these equations must reduce themselves to the equations found in standard transport phenomena books, such as those of Bird et al. (2007). Here, we briefly show how these equations are derived, using a Lagrangian representation.

Assume that a system of constant mass goes through temporal and spatial changes as presented in Fig. 1.1.

The point (x^0, y^0, z^0) represents the spatial coordinates of the particle at some fixed time t^0. Then, the spatial coordinates of the particle at any time are given by functions of

$$x = x(t, x^o, y^o, z^o) \quad y = y(t, x^o, y^o, z^o) \quad z = z(t, x^o, y^o, z^o)$$

In space, we define a property per unit volume $\Im(t,x)$, where t is time and x is the position vector such that (Aris 1962)

$$F(t) = \iiint_{V(t)} \Im(t,x)dV \tag{1.1}$$

$F(t)$ is the system variable quantity that can change with time. The balance made on $F(t)$ gives the Reynolds transport theorem (Aris 1962)

H. Arastoopour et al., *Computational Transport Phenomena of Fluid-Particle Systems*,
Mechanical Engineering Series, DOI 10.1007/978-3-319-45490-0_1

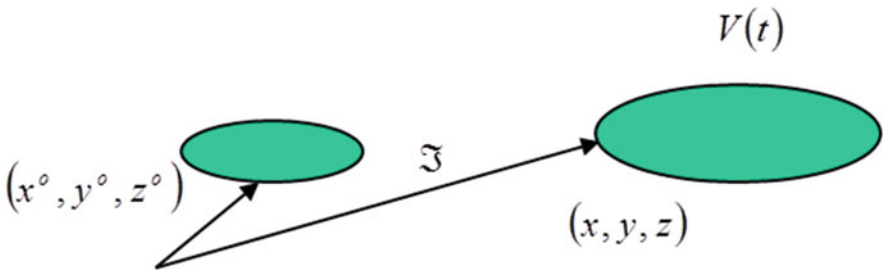

Fig. 1.1 Motion of a system of constant mass

$$\frac{d}{dt}\iiint\limits_{V(t)} \Im(t,x)dV = \iiint\limits_{V(t)} \left(\frac{\partial \Im}{\partial t} + \nabla \cdot \Im v_i\right) dV \tag{1.2}$$

In multiphase flow, the volume occupied by phase i cannot be occupied by other phases at the same position in the space at the same time. This distinction introduces the concept of the volume fraction of phase i, ε_i. The volume of phase i, V_i, in a system of volume V, is (Gidaspow 1977, 1994)

$$V_i = \iiint\limits_{V(t)} \varepsilon_i dV \text{ where } \sum_{i=1}^{n} \varepsilon_i = 1 \tag{1.3}$$

1.2 Conservation of Mass

The mass of phase i can be written as

$$m_i = \iiint\limits_{V(t)} \varepsilon_i \rho_i dV \tag{1.4}$$

For the mass m_i, moving with the velocity v_i, the following balance is valid

$$\frac{dm_i}{dt^i} = \frac{d}{dt^i}\iiint \varepsilon_i \rho_i dV = \iiint m_i' dV \tag{1.5}$$

Application of the Reynolds transport theorem results in the well-known continuity equation for phase i,

$$\frac{\partial(\varepsilon_i \rho_i)}{\partial t} + \nabla \cdot (\varepsilon_i \rho_i v_i) = m_i' \tag{1.6}$$

where m_i' is the rate of production of phase i, by mass transfer or chemical reaction. Conservation of mass requires that (Gidaspow 1994)

$$\sum_{i=1}^{n} m_i' = 0 \tag{1.7}$$

If the fluid is incompressible and there are no phase changes, V_i, the volume of phase i remains constant. Then, application of the Reynolds transport theorem results in the following incompressible continuity equation in multiphase flow

$$\frac{\partial \varepsilon_i}{\partial t} + \nabla \cdot (\varepsilon_i v_i) = 0 \tag{1.8}$$

1.3 Conservation of Momentum

The rate of change in the momentum of a multiphase system moving with the velocity v_i equals the sum of the forces acting on the system including the forces of interaction between the phases. Other forces acting on the system are surface forces, external forces, and momentum exchange due to phase change. Therefore, the momentum balance for phase i can be written as (Bowen 1976; Gidaspow 1994)

$$\frac{d}{dt} \iiint_{V(t)} \rho_i v_i \varepsilon_i dV = \oiint_{S(t)} T_i da + \iiint_{V(t)} \rho_i F_i \varepsilon_i dV + \iiint K_i dV + \iiint m_i' v_i dV \tag{1.9}$$

Application of the Reynolds transport theorem on the right-hand side of the above balance followed by the application of the divergence theorem where,

$$\oiint_{a} T_i da = \iiint_{V} \nabla \cdot T_i dV \tag{1.10}$$

on the left-hand side, gives the three momentum balances for each phase i, as follows

$$\frac{\partial(\rho_i \varepsilon_i v_i)}{\partial t} + \nabla \cdot (\rho_i \varepsilon_i v_i \otimes v_i) = \nabla \cdot T_i + \rho_i \varepsilon_i F_i + K_i + m_i' v_i \tag{1.11}$$

By differentiating and using the continuity equation for phase i, it is easy to show that the momentum balance for phase i can be expressed as

$$\rho_i \varepsilon_i \frac{dv_i}{dt^i} = \nabla \cdot T_i + \rho_i \varepsilon_i F_i + K_i + m_i' v_i \tag{1.12}$$

The term on the left-hand side accounts for acceleration of phase i. The terms on the right-hand side are momentum in-flow due to surface forces, body forces, and interaction forces, respectively.

Therefore, by expressing interaction forces K_i in terms of a friction coefficient β for solid–fluid interaction, the momentum equation for phase k becomes

$$\frac{\partial(\varepsilon_k \rho_k v_k)}{\partial t} + \nabla \cdot \varepsilon_k \rho_k v_k v_k = \nabla \cdot T_k + \varepsilon_k \rho_k F_k + \sum_j \beta_j (v_j - v_k) + m_k' v_k \tag{1.13}$$

The sum of the interaction forces K_i is clearly zero

$$\sum_{i=1}^{n} K_i = 0 \tag{1.14}$$

The stress tensor T_i for phase i is given by

$$T_i = \begin{pmatrix} T_{ixx} & T_{ixy} & T_{ixz} \\ T_{iyx} & T_{iyy} & T_{iyz} \\ T_{izx} & T_{izy} & T_{izz} \end{pmatrix} \tag{1.15}$$

where the elements, say, T_{ixy}, are the ith force in the x direction per unit area of the yth face.

The simplest expression for the stress in an inviscid flow, analogous to the single-phase potential flow theory, is through the definition of a phase pressure p_i, via the identity **I**

$$T_i = -P_i \mathrm{I} \tag{1.16}$$

For incompressible viscous flows, where there are frictional forces due to differences in phase velocities, the traction T is a function of the symmetric gradient of the velocity. The driving force for the transfer of shear is the symmetric gradient of velocity rather than the ordinary gradient because of the need to satisfy invariance under a change of frame of reference under rotation, called objectivity in continuum mechanics, or the Galileo relativity principle. To meet the requirement of objectivity, let

$$T_k = T_k(\nabla^s v_k) \tag{1.17}$$

Linearization of the T_k gives

$$T_k = A_k I + B_k(\nabla^s v_k) \tag{1.18}$$

For incompressible fluids, A_k is chosen to be the negative of the pressure of fluid k, and the derivative of the traction with respect to the symmetric gradient is the viscosity of fluid k, as shown below,

$$A_k = -P_k \tag{1.19}$$

and

$$B_k = 2\mu_k = \frac{\partial T_k}{\partial \nabla^s v_k} \tag{1.20}$$

Using the tensor identity, k-phase stress tensor can be expressed as

$$T_k = -P_k I + 2\mu_k \nabla^s v_k \tag{1.21}$$

For a constant phase viscosity μ_k, the incompressible k-phase ($\varepsilon_k \rho_k =$ constant and consequently $div(\nu_k) = 0$) Navier–Stokes equation can be rewritten as

$$\frac{\partial(\varepsilon_k \rho_k v_k)}{\partial t} + \nabla \cdot \varepsilon_k \rho_k v_k v_k = \varepsilon_k \rho_k F_k + \sum_j \beta_j (v_j - v_k) + m'_k v_k - \nabla P_k + \mu_k \nabla^2 v_k \tag{1.22}$$

For a more general case of compressible viscous flow with negligible phase change, A_k is

$$A_k = -P_k I + \lambda_k \nabla \cdot v_k \tag{1.23}$$

Therefore, the traction for phase k becomes

$$T_k = -P_k I + 2\mu_k \nabla^s v_k + \lambda_k I \nabla \cdot v_k \tag{1.24}$$

where the first term represents the k-phase pressure, the second term represents the k-phase viscous shear, and the third term represents the compression or expansion acting on k-phase by j-phase by deforming the k-velocity field,

with

$$2\mu_k + 3\lambda_k = 0 \tag{1.25}$$

Then, for compressible k-phase in a multiphase system, the Navier–Stokes equation in convective form is given as

$$\varepsilon_k \rho_k \frac{dv_k}{dt^k} = \varepsilon_k \rho_k F_k + \sum_j \beta_j (v_j - v_k) - \nabla P_k + \nabla \left(2\mu_k \nabla^s v_k - \frac{2}{3}\mu_k I \nabla \cdot v_k \right) + m_k' v_k \tag{1.26}$$

1.4 Conservation of Energy

Consider an open system of mass, m_i, that gains mass and thus energy at a rate $\frac{dm_i}{dt^i}$. The energy balance moving with phase i becomes (Gidaspow 1977, 1994)

$$\frac{dU_i'}{dt^i} = \frac{dQ_i}{dt} - P_i \frac{dV_i}{dt^i} + D_{iss} + \left(U_i^n + P_i^n / \rho_i^n \right) \frac{dm_i}{dt^i} \tag{1.27}$$

where

$$U_i' = \iiint_{V(t)} \varepsilon_i \rho_i U_i dV \tag{1.28}$$

and where the rate of heat transfer is related to the flux q_i by relations such as those used by Ishii (1975)

$$-\frac{dQ_i}{dt} = \oiint_{A(t)} q_i \varepsilon_i da = \iiint_{V(t)} (\nabla \cdot \varepsilon_i q_i) dV \tag{1.29}$$

where $A(t)$ is the area enclosing the volume of the system at any instant of time. The differential element of surface area of system i was taken to be simply $\varepsilon_i da$, thus making no distinction between area and volume fraction.

The energy dissipation by means of friction is shown as the dissipation term D_{iss}

$$D_{iss} = \iiint_{V(t)} u_i' dV \tag{1.30}$$

Now, by applying the Reynolds transport theorem to our original energy balance, we obtain

$$\frac{\partial(\varepsilon_i\rho_i U_i)}{\partial t} + \nabla\cdot(\varepsilon_i\rho_i v_i U_i) = -\nabla\cdot\varepsilon_i q_i - P_i\frac{\partial\varepsilon_i}{\partial t} - P_i\nabla\cdot\varepsilon_i v_i + h_i^n m_i' + u_i' \quad (1.31)$$

where $h_i{}^n$ is defined as the net enthalpy per unit mass entering system i at possibly nonequilibrium conditions

$$h_i = U_i + P_i/\rho_i \quad (1.32)$$

The above energy balance could be written in terms of enthalpy as

$$\varepsilon_i\rho_i\frac{dh_i}{dt^i} = -\nabla\cdot\varepsilon_i q_i + \varepsilon_i\frac{dP_i}{dt^i} + m_i'\left(h_i^n\right) + m_i' U_i + u_i' \quad (1.33)$$

Furthermore, the entropy form of the energy equation can be obtained by using the fact that the internal energy of phase i depends upon the entropy of phase i and upon the specific volume of phase i, as the following:

$$T_i\frac{\partial(\varepsilon_i\rho_i S_i)}{\partial t} + T_i\nabla\cdot(\varepsilon_i\rho_i v_i S_i) = -\nabla\cdot\varepsilon_i q_i - P_i\frac{\partial\varepsilon_i}{\partial t} + \left(h_i^n - T_i S_i\right)m_i' + u_i' \quad (1.34)$$

The second law of thermodynamics states that the entropy production for the mixture is zero for reversible processes and is positive for real irreversible processes. The energy equations in entropy form can be added to produce the entropy production for the mixture of i phases. As shown by Gidaspow (1994), some of the early multiphase energy equations violate the second law. Hence, it is necessary to check whether the equations programmed into the commercial computational fluid dynamics (CFD) codes satisfy the second law.

Expressions for entropy production are also needed for the design of energy efficient processes. For example, distillation column design is routinely done using availability analysis (Fitzmorris and Mah 1980), and vapor compression air-conditioning systems (ASHRAE 1977) are routinely designed by minimizing the entropy production for the vapor compression.

1.5 Nomenclature

C_d	Drag coefficient
D_{iss}	Energy dissipation by means of friction, kj/s
d_p	Particle diameter, m
F	Body force, N
h	Enthalpy per unit mass, J/kg
K	Interaction force, N
$\mathbf{I}$	Identity matrix
m	Mass, kg

P Pressure, N/m^2
Q Heat transfer, J
S Entropy, J/K^0
T Stress tensor
t Time, s
V System volume, m^3
$\vec{v}$ Mean velocity vector, m/s
U Overall system energy, J/kg

Greek Symbols

ε Phase volume fraction
β Interphase friction coefficient
μ Viscosity, kg/m·s
λ Bulk viscosity, kg/m·s
ρ Density kg/m^3
$\mathfrak{I}$ General property per unit volume

References

Aris R (1962) Vectors, tensors, and the basic equations of fluid dynamics. Prentice-Hall, Englewood Cliffs

ASHRAE (1977) Handbook of fundamentals. American Society of Heating, Refrigeration, and Air-Conditioning Engineers, Inc., New York

Bird RB, Stewart WE, Lightfoot EN (2007) Transport phenomena. Wiley, New York

Bowen RM (1976) Theory of mixtures. In: Eringen AC (ed) Continuum physics. Academic, London

Fitzmorris RE, Mah RSH (1980) Improving distillation column design using thermodynamic availability analysis. AIChE J 26(2):265–273

Gidaspow D (1977) Fluid-particle systems. In: Proceedings of the NATO advanced study institute on two-phase flows and heat transfer, Istanbul, August 1976, vol 1. Hemisphere Publishing Corporation, New York, pp 115–128

Gidaspow D (1994) Multiphase flow and fluidization: continuum and kinetic theory descriptions. Academic, California

Ishii M (1975) Thermo-fluid dynamic theory of two-phase flow. NASA STI/Recon Technical Report A, 75, 29657

Chapter 2
Conservation and Constitutive Equations for Fluid–Particle Flow Systems

2.1 Introduction

A major computational advance in the calculation of multiphase flow regimes made in the 1980s was the use of computational codes based on the Navier–Stokes equation for solving the governing equations presented in Chap. 1.

The basic momentum balances for the fluid and particulate phases are as follows:

Fluid momentum balance

$$\frac{\partial\left(\rho_f \varepsilon_f v_f\right)}{\partial t} + \nabla \cdot \left(\rho_f \varepsilon_f v_f v_f\right) = \varepsilon_f \rho_f g - \varepsilon_f \nabla P + \nabla \cdot \varepsilon_f \tau_f + \beta\left(v_s - v_f\right) \tag{2.1}$$

Solid momentum balance

$$\frac{\partial\left(\rho_s \varepsilon_s v_s\right)}{\partial t} + \nabla \cdot \left(\rho_s \varepsilon_s v_s v_s\right) = \varepsilon_s \rho_s g - \varepsilon_s \nabla P - \nabla P_s + \nabla \cdot \varepsilon_s \tau_s + \beta\left(v_f - v_s\right) \tag{2.2}$$

where ρ is density, ε is volume fraction, t is time, v is velocity vector, P is pressure, g is gravity acceleration, τ is stress tensor, and β is the interface momentum exchange coefficient.

The summation of volume fractions for all phases is equal to one

$$\varepsilon_f + \varepsilon_s = 1 \tag{2.3}$$

In order to close the conservation equations for the momentum, one needs to calculate the stress tensors and consequently the solid-phase viscosity. Two types of models were used to close the coupled Navier–Stokes equations for both the fluid and disperse particles. The first group of models requires an empirical input of particulate viscosity and gradient of the disperse pressure. The second group of models is based on the kinetic theory of granular flow. These models compute the particulate viscosity and the gradient of the solid pressure as a function of the

H. Arastoopour et al., *Computational Transport Phenomena of Fluid-Particle Systems*, Mechanical Engineering Series, DOI 10.1007/978-3-319-45490-0_2

granular temperature (Arastoopour 2001; Gidaspow 1994; Gidaspow and Jiradilok 2009). The granular temperature is a measure of the random particle kinetic energy per unit mass. It is produced due to "viscous-type dissipation" and consumed due to inelastic collisions. The random granular temperature equation for the particle phase can be expressed as

$$\frac{3}{2}\left[\frac{\partial(\rho_s\varepsilon_s\theta)}{\partial t}+\nabla\cdot(\rho_s\varepsilon_s\theta v_s)\right]=(-P_s\mathbf{I}+\tau_s):\nabla v_s+\nabla\cdot(k_s\nabla\theta)-\gamma+\varphi_{gs} \tag{2.4}$$

$$\text{Accumulation} + \text{net outflow} = \text{production} + \text{conduction} - \text{dissipation} + \text{granular energy exchange between phases}$$

where θ is granular temperature (which is defined as the mean of the squares of particle velocity fluctuation), k_s is granular conductivity, γ is the collisional energy dissipation, and φ_{gs} is the granular energy exchange between phases which is defined as $\varphi_{gs}=-3\beta_{gs}\theta$ for laminar flows (Gidaspow et al. 1991) and $\varphi_{gs}=\beta_{gs}\left(\sqrt{2k_f}\sqrt{3\theta}-2k_f\right)$ for disperse turbulent flows (Sinclair and Mallo 1998). In the latter case, K_f is the turbulent kinetic energy of the fluid and β_{gs} is the gas–solid exchange coefficient.

The stress tensor for each phase is given by a Newtonian-type viscous approximation, as

$$\tau_f=\varepsilon_f\mu_f\left(\nabla v_f+\nabla v_f^T\right)-\frac{2}{3}\varepsilon_f\mu_f\nabla\cdot v_f\mathbf{I} \tag{2.5}$$

$$\tau_s=\varepsilon_s\mu_s\left(\nabla v_s+\nabla v_s^T\right)+\varepsilon_s\left(\xi_s-\frac{2}{3}\mu_s\right)\nabla\cdot v_s\mathbf{I} \tag{2.6}$$

Particle pressure, P_s; shear viscosity, μ_s; and bulk viscosity, ξ_s, are expressed as a function of granular temperature based on the kinetic theory model (Gidaspow 1994).

The constitutive equation for the shear viscosity μ_s consists of three sources, namely, kinetic, collision, and friction, which could be written either in an additive manner or a continuous form as (see Sect. 2.7 for more details)

$$\mu_s=\mu_{kin}+\mu_{col}+\mu_{fr} \tag{2.7}$$

The first two parts are calculated based on the kinetic theory. In dense granular flows, in addition to the kinetic and collisional stresses (described by the kinetic theory), the model should account for the frictional stresses as well, which is dominant in flow regimes denser than the bubbling regime. The frictional behavior

of granular matters is discussed in this chapter based on soil mechanics principles (see Sect. 2.7).

This chapter starts with the derivation of the conservation equation for mass, momentum, and granular temperature based on the kinetic theory approach for uniform and multi-type particles.

2.2 Background on the Kinetic Theory

Originally, the kinetic theory was developed by Chapman and Cowling (1970) for gases to predict the behavior of mass point molecules whose interaction energies are conserved. Nearly three decades ago, this theory was extended to particulate flow where the interactions between particles are not conserved. Savage and Jeffrey (1981) were probably the first to apply the kinetic theory to rapidly deforming material in a form of smooth hard spherical particles to develop the particle phase constitutive equation. In their derivation, to calculate the stress tensor arising from interparticle collisions, they assumed that the collisions between particles were purely elastic.

Although in some granular flows the restitution coefficient is restrained to values close to unity, its deviation from unity results in a significant variation in the properties of granular flow. This was shown first by Jenkins and Savage (1983). They extended the kinetic theory of an idealized granular mixture to predict the rapid deformation of granular material by including energy dissipation during collision for nearly inelastic particles. Later, Lun et al. (1984) developed a theory that predicts the simple shear flow behavior for a wide range of the restitution coefficient.

Many models for granular flow were then developed based on the kinetic theory approach (Jenkins and Richman 1985; Gidaspow 1994). In addition, the kinetic theory has been extended to cohesive and multi-property particle flow (Kim and Arastoopour 2002; Iddir and Arastoopour 2005).

In the particle phase, the frequency distribution of velocities of particles, f, is a function of position, $\mathbf{r}$, and the instantaneous velocity, $\mathbf{c}$, as well as time, t:

$$f = f\left(t, \mathbf{r}, \mathbf{c}\right) \tag{2.8}$$

The six coordinates, the position, $\mathbf{r}$, and the velocity, $\mathbf{c}$, are sufficient to determine the location of a particle, because Newton's second law has six integration constants. The velocity distribution, f, of the particles is often close to the normal distribution, called the Maxwellian distribution in the kinetic theory of gases. For a

Maxwellian distribution, the kinetic viscosity is zero. Particle viscosity is nonzero due to particle interaction and a non-Maxwellian distribution.

The number of particles per unit volume, n, is the integral over the velocity space, **c**:

$$n = \int f d\mathbf{c} \tag{2.9}$$

The mean value of a quantity ϕ, such as mass, momentum, energy, and stress, is defined to be

$$n\langle\varphi\rangle = \int \varphi f d\mathbf{c} \tag{2.10}$$

Hence, the hydrodynamic velocity, **v**, is the integral over all the velocity space, as shown below

$$\mathbf{v} = \frac{1}{n}\int \mathbf{c} f(\mathbf{c}) d\mathbf{c} \tag{2.11}$$

The transport of a quantity ϕ, such as heat, must be invariant under a change of frame. Hence, it cannot be a function of the velocity, **c**. Otherwise, it will have different values in different frames of reference. But **c**–**v** is independent of the frame of reference. Hence, we define **C** as the difference between the instantaneous and the hydrodynamic velocities

$$\mathbf{C} = \mathbf{c} - \mathbf{v} \tag{2.12}$$

In kinetic theory (Chapman and Cowling 1970), this difference is called the peculiar velocity. Its mean is zero, as shown below, since the mean of **c** is equal to **v**:

$$< C > \; = \; < c - v > \; = v - v \; = \; 0 \tag{2.13}$$

This property is the same as that of the turbulent velocity, **v**, defined as the instantaneous minus the average velocity. The flux vector of ϕ is defined as n $<$ **C**ϕ(**C**) $>$. For example, if $\phi \; = \; E$, the internal energy, then the conduction flux, q, becomes $\boldsymbol{q} = n<E\boldsymbol{C}>$.

Since momentum is the mass, m, times the velocity, C, the kinetic stress tensor, $\mathbf{P}_k$ is as follows:

$$P_k = \; n < \mathbf{C}m\mathbf{C} > \; = \rho < \mathbf{CC} > \tag{2.14}$$

The hydrostatic pressure, p, is the mean of the sum of the normal components of the stress tensor, **p**,

$$\mathbf{p} = 1/3\left(p_{xx} + p_{yy} + p_{zz}\right) \tag{2.15}$$

In the kinetic theory of gases, the thermal temperature, T, is defined as the average of the random kinetic energy, with the conversion factor of the Boltzmann constant from Joules to degrees Kelvin, as shown,

$$k_B T = 1/3\, m < C^2{}_x + C^2{}_y + C^2{}_z > \tag{2.16}$$

where the subscript of the peculiar velocity, **C**, indicates the component of **C** in the x, y, and z directions, respectively. The Boltzmann constant has the value

$$k_B = 1.3805 \times 10^{-23}\, J/K \tag{2.17}$$

The ideal gas law constant equals the very small Boltzmann constant, due to the small mass of the molecule, m, times the large value of the Avogadro's number, 6.023×10^{23}, the number of molecules per mole. Converting from Joules to calories gives the gas law constant of 1.987 cal/g-mole-deg K.

Elimination of the squares of the peculiar velocities in

$$P = 1/\,3\, nm < \mathbf{C}^2 > \tag{2.18}$$

and in the definition of temperature (Eq. 2.16) gives the ideal gas law equation of state

$$P = n\, k_B T = (N/V)\, RT \tag{2.19}$$

where N is the number of moles, V is the volume, and R is the universal gas constant.

The granular temperature is defined as the random kinetic energy of the particles without the conversion of Joules to degrees. Equation (2.16) suggests that it can be defined in two ways: similar to Eq. (2.16) or as kinetic energy per unit mass. Let θ be the granular temperature for uniform size particles, the random kinetic energy per unit mass. Then,

$$\theta = 1/3\langle \mathbf{C}^2 \rangle = 1/(3n) \int_{-\infty}^{\infty} \int_{-\infty}^{\infty} \int_{-\infty}^{\infty} \left(C_x^2 + C_y^2 + C_z^2\right) dC_x dC_y dC_z \tag{2.20}$$

in three dimensions. In two dimensions, we would have only two random velocities, and we would divide $< \mathbf{C}^2 >$ by two. In one dimension, we have only one random velocity, and the granular temperature is then simply the variance of the measured instantaneous velocities. However, this behavior is not the same as the three-dimensional granular temperature shown in Eq. (2.20). The units of the granular temperature are $(\text{m/sec})^2$.

The equation of state for particles can be obtained by eliminating $< \mathbf{C}^2 >$ between Eqs. (2.18) and (2.19). This gives

$$p_s = nm\theta \tag{2.21}$$

where the subscript, s, was added to emphasize that it is the solid pressure. The variable nm is the bulk density. In terms of the volume fraction of solids, ε_s and the solid density, ρ_s the ideal equation of state for particles becomes

$$p_s = \varepsilon_s \rho_s \theta \tag{2.22}$$

The more complete equation of state for particles, containing the collisional contribution, has been verified experimentally by Gidaspow and Huilin (1998).

2.2.1 Boltzmann Integral–Differential Equation

The Boltzmann equation for the frequency distribution, f (Gidaspow 1994), can be written as

$$\frac{\partial f}{\partial t} + \mathbf{c} \cdot \frac{\partial f}{\partial \mathbf{r}} + \mathbf{F} \frac{\partial f}{\partial \mathbf{c}} = \left(\frac{\partial f}{\partial t} \right)_{coll} \tag{2.23}$$

where $\mathbf{c}$ and $\mathbf{r}$ were regarded as independent coordinates and where Newton's law of motion was

$$\frac{Force}{Unit\ mass} \mathbf{F} = \frac{d\mathbf{c}}{dt} \tag{2.24}$$

For binary collisions of rigid particles, the right-hand side of the Boltzmann equation (2.23) assumes the form

$$\left(\frac{\partial f}{\partial t} \right)_{coll\ binary} = \int\int \left(f^{(2)} \mathbf{c}'_{12} \cdot \mathbf{k} - f^{(2)} \mathbf{c}_{12} \cdot \mathbf{k} \right) d_{12}^2 d\mathbf{k} d\mathbf{c}_1 \tag{2.25}$$

where the primes indicate the quantities after particle interaction–collision and $f^{(2)}$ is the product of the respective single-particle distributions. Hence, the Boltzmann equation is an integral–differential equation. Because of its nonlinearity, it must be solved by iteration. For the first approximation, one takes the Maxwellian distribution. The second approximation, as shown in detail in Chapman and Cowling (1970), will give rise to a Navier–Stokes-type equation. This is done efficiently using an altered form of the Boltzmann operator, as presented below,

$$\mathbf{C} = \mathbf{c} - \mathbf{v}(t, \mathbf{r}) \tag{2.26}$$

Changing the coordinates from **c** to **C**,

$$f(t, \mathbf{r}, \mathbf{c}) = f_C(t, \mathbf{r}, \mathbf{C}) \tag{2.27}$$

Applying chain rule to Eqs. (2.25–2.27), the Boltzmann equation can be expressed as

$$\frac{Df}{Dt} + \mathbf{C}\frac{\partial f}{\partial \mathbf{r}} + \left(\mathbf{F} - \frac{D\mathbf{v}}{Dt}\right)\frac{\partial f}{\partial \mathbf{C}} - \frac{\partial f}{\partial \mathbf{C}}\mathbf{C} : \frac{\partial \mathbf{v}}{\partial \mathbf{r}} = \left(\frac{\partial f}{\partial t}\right)_{coll} \tag{2.28}$$

A transport equation for a quantity ψ can be obtained starting with the Boltzmann equation by multiplying it by ψ (Eq. 2.29) and integrating over **c** (Eq. 2.30),

$$\int \psi\left(\frac{\partial f}{\partial t} + \mathbf{c}\cdot\frac{\partial f}{\partial \mathbf{r}} + \mathbf{F}\cdot\frac{\partial f}{\partial \mathbf{c}}\right)d\mathbf{c} = \int \psi\left(\frac{\partial f}{\partial t}\right)_{coll} d\mathbf{c} \tag{2.29}$$

$$\frac{\partial n\langle\psi\rangle}{\partial t} + \frac{\partial}{\partial \mathbf{r}}\cdot n\langle\psi\mathbf{c}\rangle - n\left[\left\langle\frac{\partial\psi}{\partial t}\right\rangle + \left\langle\mathbf{c}\cdot\frac{\partial\psi}{\partial \mathbf{r}}\right\rangle + \mathbf{F}\cdot\left\langle\frac{\partial\psi}{\partial \mathbf{c}}\right\rangle\right] = \int \psi\left(\frac{\partial f}{\partial t}\right)_{coll} d\mathbf{c} \tag{2.30}$$

Now, we need to find the single-particle distribution function *f(r,* **c**, t*)* and the pair distribution function $f^{(2)}(\mathbf{r_1}, \mathbf{c_1}; \mathbf{r_2}, \mathbf{c_2};$ t*)*. Here, we take the Maxwellian velocity distribution function as the single-particle distribution (Savage and Jeffrey 1981; Jenkins and Savage 1983; Ding and Gidaspow 1990)

$$f(\mathbf{r}, \mathbf{c}, t) = \frac{n}{(2\pi\theta)^{\frac{3}{2}}}\exp\left[-\frac{(\mathbf{c} - \mathbf{v})^2}{2\theta}\right] \tag{2.31}$$

and the Enskog assumption for the pair distribution function is used next (Chapman and Cowling 1970; Lun et al. 1984; Ding and Gidaspow 1990). That is,

$$f^{(2)}(\mathrm{r}_1,\ \mathrm{c}_1;\ \mathrm{r}_2,\ \mathrm{c}_2;\ \mathrm{t}) = g_0(\varepsilon_s) f_1\left(\mathbf{r} - \tfrac{1}{2}d_p\mathbf{k}, \mathbf{c}_1; t\right) f_2\left(\mathbf{r} + \tfrac{1}{2}d_p\mathbf{k}, \mathbf{c}_2; t\right) \tag{2.32}$$

where g_o is the equilibrium radial distribution function (Savage and Jeffrey 1981).

Detailed derivation of the equations can be found elsewhere (Ding and Gidaspow 1990; Gidaspow 1994).

2.3 Conservation Laws with No Particle Interaction and Collisions

By substituting for ψ mass, momentum, and energy, the corresponding conservation laws are easily obtained from Maxwell's equation (2.30). For a case with no particle interaction/collisional contribution,

$$\frac{\partial n\langle\psi\rangle}{\partial t} + \nabla n\langle\psi\mathbf{c}\rangle - n\mathbf{F}\left\langle\frac{\partial\psi}{\partial\mathbf{c}}\right\rangle = 0 \tag{2.33}$$

2.3.1 Conservation of Mass

Let $\psi = m$, since $nm = \varepsilon_s\rho_s = \rho$

$$\frac{\partial}{\partial t}(\varepsilon_s\rho_s) + \nabla\cdot(\varepsilon_s\rho_s\mathbf{v}_s) = 0 \tag{2.34}$$

2.3.2 Conservation of Momentum

Let $\psi = m\mathbf{c}$

$$n\langle\mathbf{c}\psi\rangle = nm\langle\mathbf{cc}\rangle = \rho\langle(\mathbf{C}+\mathbf{v})(\mathbf{C}+\mathbf{v})\rangle = \rho\int\left[\mathbf{CC}+2\mathbf{Cv}+\mathbf{v}^2\right]fd\mathbf{c} = \mathbf{P}_k + \rho\mathbf{vv}$$

Since $\mathbf{P}_k = \rho\langle\mathbf{CC}\rangle$ and $\langle\mathbf{C}\rangle = 0$

$$\frac{\partial}{\partial t}(\varepsilon_s\rho_s\mathbf{v}_s) + \nabla(\mathbf{P}_k + \varepsilon_s\rho_s\mathbf{v}_s\mathbf{v}_s) = \varepsilon_s\rho_s\mathbf{F}_s \tag{2.35}$$

2.3.3 Conservation of Solid-Phase Fluctuating Energy

Let $\psi = \frac{1}{2}m\mathbf{c}^2$

$$\begin{aligned} n\langle\mathbf{c}\psi\rangle &= \frac{nm}{2}\langle\mathbf{c}^2\mathbf{c}\rangle = \frac{1}{2}\rho\langle\left(\mathbf{CC}+2\mathbf{Cv}+\mathbf{v}^2\right)(\mathbf{C}+\mathbf{v})\rangle \\ &= \frac{1}{2}\rho\int\left[\mathbf{C}^2\mathbf{C}+\left(\mathbf{v}^2+\mathbf{C}^2+2\mathbf{CC}\right)\mathbf{v}\right]fd\mathbf{c} \end{aligned} \tag{2.36}$$

Note: $\mathbf{q}_k = \frac{1}{2}\rho\int\mathbf{C}^2\mathbf{C}f\mathbf{c} = \frac{1}{2}nm\langle\mathbf{C}^2\mathbf{C}\rangle$

and since $\theta = \frac{1}{3}\langle \mathbf{C}^2 \rangle$

$$n\langle \psi \mathbf{c} \rangle = \mathbf{q}_k + \mathbf{v}\left(\frac{1}{2}\rho \mathbf{v}^2 + \frac{3\theta\rho}{2}\right) + \mathbf{P}_k \mathbf{v} \tag{2.37}$$

$$\frac{\partial\left(\frac{3}{2}\theta\rho + \frac{1}{2}\rho \mathbf{v}^2\right)}{\partial t} + \nabla \cdot \left[\mathbf{q}_k + \mathbf{v}\left(\frac{3}{2}\theta\rho + \frac{1}{2}\rho \mathbf{v}^2\right) + \mathbf{P}_k \mathbf{v}\right] = \rho \mathbf{F} \mathbf{v} \tag{2.38}$$

It is easy to derive the conservation equation for the fluctuating energy from Eq. (2.38) as

$$\frac{3}{2}\left[\frac{\partial}{\partial t}(\varepsilon_s \rho_s \theta) + \nabla.(\varepsilon_s \rho_s \mathbf{v}\theta)\right] = -\nabla \cdot \mathbf{q}_k - \mathbf{P}_k : \nabla \cdot \mathbf{v} \tag{2.39}$$

where $\mathbf{P}_k = \rho\langle \mathbf{CC} \rangle$.

Similarly, we can obtain the equations for the stress tensor $\langle \mathbf{CC} \rangle$. This equation is similar to the Reynolds stress equations in single-phase turbulent flow. However, in the Reynolds stress equation, the average is over a time interval. Here, the averaging is over the velocity space. These averages are not equal as experimentally shown by Tartan and Gidaspow (2004). If we include rotation (Goldshtein and Shapiro 1995) in addition to the translation presented here, we can obtain a balance for the rotational temperature, as in single-phase fluids (Condiff et al. 1965).

2.4 Conservation Laws with Particle Interaction and Collisions

In the previous section, we presented the inviscid conservation equations by neglecting the collisional part of Eq. (2.16). In order to derive the equations that include the solid viscosity and solid stresses, we use the approach of Ding and Gidaspow (1990) and start with the Boltzmann equation (Eq. 2.16), with a nonzero source term, considering only binary collisions between hard and smooth but inelastic particles. In this case, the right-hand side of the Boltzmann equation is similar to Eq. (2.18) that gives the collisional rate of change of the mean of ψ.

By defining the external forces, **F**, as the sum of the gravity, the aerodynamic drag, and the buoyancy (which appears through the pressure gradient in Eq. (2.40) (Ding and Gidaspow 1990),

$$\mathbf{F} = g + \frac{D}{m}\left(\mathbf{v}_g - \mathbf{v}_s\right) - \frac{1}{\rho_s}\nabla p \tag{2.40}$$

where D is the drag force coefficient, and, by combining Eqs. (2.25 and 2.30), one can derive the momentum equation $(\psi = m\mathbf{c})$,

$$\frac{\partial}{\partial t}(\varepsilon_s\rho_s\mathbf{v}_s) + \nabla(\varepsilon_s\rho_s\mathbf{v}_s\mathbf{v}_s) = -\varepsilon_s\nabla p + \varepsilon_s\rho_s g + \beta\left(\mathbf{v}_g - \mathbf{v}_s\right) + \nabla.(\tau_k + \tau_c) \quad (2.41)$$

In Eq. (2.41),

$$\beta = \varepsilon_s\rho_s\frac{D}{m} \quad (2.42)$$

τ_k and τ_c are the kinetic part and collisional part of the total stress tensor, $\boldsymbol{\tau_s}$, respectively.

Similarly, we can derive the equation for the fluctuating energy of the solid phase (granular temperature) using the momentum equation and taking $\psi = \frac{1}{2}m\mathbf{c}^2$ and $\theta = \frac{1}{3}\langle\mathbf{C}^2\rangle$,

$$\frac{3}{2}\left[\frac{\partial}{\partial t}(\varepsilon_s\rho_s\theta) + \nabla.(\varepsilon_s\rho_s\mathbf{v}\theta)\right] = \tau_s : \nabla\cdot\mathbf{v}_s - \nabla\cdot\mathbf{q} - \gamma + \beta\langle C_{gi}C_i - C_iC_i\rangle \quad (2.43)$$

On the right-hand side of Eq. (2.43), the first term represents the energy production due to the deformation work, the second term is the energy transfer, γ is the collisional energy dissipation due to inelastic collisions, and the last term is the net rate of transfer of fluctuation energy between the two phases. The correlation between the gas-phase fluctuation velocity and the solid-phase fluctuation velocity φ_{gs} is negligible when the particle response time, $\tau_p = m/D$, is much larger than the timescale characteristic of the mean fluid motion (Ding and Gidaspow 1990). This assumption is valid when the particles are heavy and large. Therefore, the equation for the fluctuating energy of the solid phase becomes

$$\frac{3}{2}\left[\frac{\partial}{\partial t}(\varepsilon_s\rho_s\theta) + \nabla.(\varepsilon_s\rho_s\mathbf{v}\theta)\right] = \tau_s : \nabla\cdot\mathbf{v}_s - \nabla\cdot\mathbf{q} - \gamma \quad (2.44)$$

To close the conservation equations for the momentum and the granular temperature, we need to calculate the τ_k, τ_c,γ, q that are functions of the collisional integral (Eq. 2.25).

As shown earlier, the stress tensor for each phase is given by a Newtonian-type viscous approximation

$$\tau_f = \varepsilon_f\mu_f\left(\nabla v_f + \nabla v_f^T\right) - \frac{2}{3}\varepsilon_f\mu_f\nabla\cdot v_f\mathbf{I} \quad (2.45)$$

$$\tau_s = \varepsilon_s\mu_s\left(\nabla v_s + \nabla v_s^T\right) + \varepsilon_s\left(\xi_s - \frac{2}{3}\mu_s\right)\nabla\cdot v_s\mathbf{I} \quad (2.46)$$

Particle pressure, P_s; shear viscosity, μ_s; and bulk viscosity, ξ_s, are expressed as a function of granular temperature (Gidaspow 1994). Here, we show only how to obtain the viscosity of the particulate phase in a dilute system.

Let the momentum flux be

$$Q = \rho v \langle v \rangle \tag{2.47}$$

(Momentum/volume × average of oscillating velocity)

Then, for a constant density ρ, the change in momentum flux is

$$\Delta Q = l\rho \langle v \rangle \frac{dv}{dx} \tag{2.48}$$

The viscosity for fully developed incompressible flow is defined by

$$\text{Shear } = \mu \frac{dv}{dx} \tag{2.49}$$

The momentum transport ΔQ equals the force per unit area

$$\Delta Q = \text{ Shear} \tag{2.50}$$

Therefore, the viscosity assumes the form

$$\mu = l\rho \langle v \rangle \tag{2.51}$$

From Eq. (2.51), it can be seen that

$$\mu = \rho D \tag{2.52}$$

as in the kinetic theory of gases. Therefore, an equation for the collisional viscosity may be expressed as

$$\mu = \left(\frac{1}{3\sqrt{\pi}} \right) \rho_p d_p \sqrt{\theta} \tag{2.53}$$

Kinematic viscosity = mean free path × fluctuating velocity

For smooth rigid spherical molecules of diameter d_p,

$$\mu_l = \frac{5}{16 d_p^2} \left(\frac{k_B m T}{\pi} \right)^{1/2} \tag{2.54}$$

where $m = \rho_p \frac{\pi}{6} d_p^3$

To convert T to granular temperature θ, let $\frac{k_B}{m} = 1$. Thus,

$$\text{DILUTE} \quad \mu_s = \frac{5\sqrt{\pi}}{96} \rho_p d_p \theta^{1/2} \tag{2.55}$$

The interpretation is as follows:

$$\text{DILUTE} \quad \mu_s = \frac{5\sqrt{\pi}}{96} \cdot (\rho_p \varepsilon_s) \cdot \left(\frac{d_p}{\varepsilon_s}\right) \cdot \theta^{1/2} \tag{2.56}$$

VISCOSITY = constant × bulk density × mean free path × oscillation velocity

Detailed derivation for the rest of the constitutive equation in a dense system for the particle pressure, P_s; shear viscosity, μ_s; and bulk viscosity, ξ_s, as a function of granular temperature, can be found elsewhere (Ding and Gidaspow 1990; Gidaspow 1994) and are

$$P_s = \varepsilon_s \rho_s \theta + 2\rho_s (1+e) \varepsilon_s^2 g_0 \theta \tag{2.57}$$

$$\mu_s = \frac{4}{5}\varepsilon_s \rho_s d_p g_0 (1+e)\left(\frac{\theta}{\pi}\right)^{1/2} + \frac{10\rho_s d_p \sqrt{\theta\pi}}{96\varepsilon_s (1+e) g_0}\left[1 + \frac{4}{5} g_0 \varepsilon_s (1+e)\right]^2 \tag{2.58}$$

$$\zeta_s = \frac{4}{3}\varepsilon_s \rho_s d_p g_0 (1+e)\left(\frac{\theta}{\pi}\right)^{1/2} \tag{2.59}$$

where d_p is the diameter of particle, e is the restitution coefficient, and g_0 is the radial distribution function. The radial distribution function expressing the statistics of the spatial arrangement of the particles is given by a geometric approximation, the Bagnold's equation,

$$g_0 = \left[1 - \left(\frac{\varepsilon_s}{\varepsilon_{s,\max}}\right)^{1/3}\right]^{-1} \tag{2.60}$$

The granular conductivity, k_s consists of the kinetic part due to the elastic particles derived from dilute kinetic theory of gases (Chapman and Cowling 1970) and the collisional part due to the inelastic collision of particles as reviewed by Gidaspow (1994):

$$k_s = \frac{150\rho_s d_p \sqrt{\theta\pi}}{384(1+e)g_0}\left[1 + \frac{6}{5}\varepsilon_s g_0 (1+e)\right]^2 + 2\rho_s \varepsilon_s^2 d_p (1+e) g_0 \sqrt{\frac{\theta}{\pi}} \tag{2.61}$$

The energy dissipation due to inelastic collision of particles, first evaluated by Savage and his colleagues, is

$$\gamma = \frac{12(1-e^2)g_0}{d_p\sqrt{\pi}} \rho_s \varepsilon_s^2 \theta^{3/2} \tag{2.62}$$

In this analysis, it is assumed that the interaction force between fluid and particles is due only to drag. Discussion of the drag models will be presented in Chap. 3.

2.5 Boundary Conditions

At the inlet and outlet, all properties should be defined based on the specific physics and assumption of the problem. For the gas phase, no-slip and non-penetrating wall conditions may be considered. For the solid phase, the slip boundary condition is the recommended boundary condition (Johnson and Jackson 1987):

$$\overline{\tau}_s = -\frac{\pi}{6}\sqrt{3\phi}\,\frac{\varepsilon_s}{\varepsilon_{s,\max}}\rho_s g_0 \sqrt{\theta_s}\,\vec{v}_{s,para} \tag{2.63}$$

where $\vec{v}_{s,para}$ is the particle slip velocity parallel to the wall. ϕ is the specularity coefficient between the particle and the wall, which is defined as the average fraction of relative tangential momentum transferred between the particle and the wall during a collision. The specularity coefficient varies from zero (smooth walls) to one (rough walls). A proper value based on the particles and wall properties should be assumed. For a specularity coefficient tending toward zero, a free slip boundary condition for the solids tangential velocity is imposed at a smooth wall boundary as explained by Benyahia et al. (2005).

Johnson and Jackson (1987) proposed the following wall boundary condition for the total granular heat flux as

$$q_s = \frac{\pi}{6}\sqrt{3\phi}\,\frac{\varepsilon_s}{\varepsilon_{s,\max}}\rho_s g_0 \sqrt{\theta_s}\,\vec{v}_{s,para}\cdot\vec{v}_{s,para} - \frac{\pi}{4}\sqrt{3}\frac{\varepsilon_s}{\varepsilon_{s,\max}}\left(1-e_{sw}^2\right)\rho_s g_0 \theta_s^{3/2} \tag{2.64}$$

The dissipation of solids turbulent kinetic energy by collisions with the wall is specified by the particle–wall restitution coefficient, e_{sw}. A high value of specularity coefficient implies high production at the wall, and a value of e_{sw} close to unity implies low dissipation of granular energy at the wall. It is expected that the specularity coefficient and the particle–wall restitution coefficient need to be calibrated for a given gas/particle flow system because the specularity coefficient cannot be measured and e_{sw} can be measured only with some difficulty (Benyahia et al. 2005). Equations (2.63) and (2.64) could be written as

$$v_{s,w} = -\frac{6\mu_s \varepsilon_{s,\max}}{\sqrt{3}\pi\varphi\rho_s\varepsilon_s g_0\sqrt{\theta}}\,\frac{\partial v_{s,w}}{\partial x} \tag{2.65}$$

$$\theta_w = -\frac{\kappa\theta}{\gamma_w}\,\frac{\partial\theta_w}{\partial x} + \frac{\sqrt{3}\pi\varphi\rho_s\varepsilon_s v_{s,slip}^2 g_0\theta^{3/2}}{6\varepsilon_{s,\max}\gamma_w} \tag{2.66}$$

where

$$\gamma_w = \frac{\sqrt{3}\pi\left(1-e_{sw}^2\right)\varepsilon_s\rho_s g_0\theta^{3/2}}{4\varepsilon_{s,\max}} \tag{2.67}$$

2.6 Modeling of Multi-Type Particle Flow Using the Kinetic Theory Approach

Fluid–particle systems are composed of particles of different properties, in which segregation by size or density may occur during the flow, as was shown by Arastoopour et al. (1982). The researchers developed a hydrodynamic model for a mixture of gas and a multisize solid phase. They applied it to simulate one-dimensional flow in a vertical pneumatic conveying line. They showed that the particle size has a great effect on the pressure drop and choking velocity and that particles segregate along the vertical transport line.

The experiment of Savage and Sayed (1984) showed the stresses in shear cell for a mono-size mixture of polystyrenes beads were about five times higher than those for a binary mixture. Jenkins and Mancini (1987) extended the kinetic theory of dense gases to a binary mixture of idealized granular material for the low dissipation case. Jenkins and Mancini (1989) presented an extension of the kinetic theory for a binary mixture of smooth nearly elastic spheres. Alam et al. (2002) and Alam and Luding (2003) generalized the model of Willits and Arnarson (1999) for a mixture of particles having different mass and size. However, the model proposed by Alam et al. (2002) was limited to energy non-equipartition. Zamankhan (1995) concluded that energy non-equipartition must be included in mixtures with different particle properties. Wildman and Parker (2002) and Feitosa and Menon (2002) experimentally confirmed the coexistence of two granular temperatures when the binary mixture was exposed to external vibrations. Huilin et al. (2000) developed a model for two-size particles with different granular temperatures; however, they used an approach that takes the arithmetic average of the particle properties in the collisional operator and the momentum source vanished. Garzó and Dufty (2002) solved the kinetic equation for systems away from equilibrium. This approach could capture not only the energy non-equipartition but also the flow behavior for a wide range of restitution coefficients. Such a model is restricted to dilute systems where the radial distribution function is close to unity. Iddir and Arastoopour (2005) and Iddir et al. (2005) extended the kinetic theory to a multi-type (size and/or density) mixture, assuming a non-Maxwellian velocity distribution and energy non-equipartition. Each particle type is represented by a phase, with an average velocity and a fluctuating energy or granular temperature. This means that the interaction between the different type particle phases is at the interface. They assumed that the deviation from the Maxwellian velocity distribution is in each individual particulate phase; however, they assumed Maxwellian velocity distribution at the interface. Then they solved the Boltzmann's equation for each particulate phase using the Chapman–Enskog procedure by adding a perturbation to the Maxwellian velocity distribution function. In a similar analysis, Willits and Arnarson (1999) solved the Boltzmann's equation based on Maxwellian reference state and the revised Enskog equation. Although the range of applicability of Iddir and Arastoopour's work and Willits and Arnarson's work is the same, the major differences between the two studies are non-equipartition and unequal particle size

properties considered in the Iddir and Arastoopour model. Willits and Arnarson assumed a multicomponent mixture where all the particles fluctuate about the same mass average velocity and having the same granular temperature. Iddir and Arastoopour (2005) considered a multiphase granular flow where each phase is represented by particles having different properties, velocities, and granular temperatures. The following is the model developed by Iddir and Arastoopour (2005) that has been incorporated in the MFIX computer code (Benyahia 2008).

2.6.1 Model Development

The present model has been obtained by considering a mixture of N solid phases (N is the number of solid phases); each phase is composed of smooth inelastic hard spheres, and it was also assumed the collision of particles is the dominant interaction force between two particles. The assumption of hard spheres suggests that the collisions are almost instantaneous, so that binary collisions may safely be assumed. Each particulate phase i contains particles of mass m_i and diameter d_i that collide with each other in the phase i. The collisions/interaction between particle i and other particles of different phases occurs at the interface between phase i and the other particulate phases. Each particle in the phase i moving with instantaneous velocity $\vec{c}_i$ is subject to an external force $\vec{F}_{iext}$. At any time t, the probable number of particles per unit of volume, $d\vec{r}$, with velocity varying between $\vec{c}_i$ and $\vec{c}_i + d\vec{c}_i$, is the product of the single velocity distribution function $f_i^1(\vec{c}, \vec{r}, t)$ and the variation of the velocity $d\vec{c}_i$

$$n_i(\vec{r}, t) = \int f_i^1(\vec{c}_i, \vec{r}, t) d\vec{c}_i \tag{2.68}$$

Hence, the mean value of any property of phase i, $\psi_i(\vec{c}_i)$ is defined as

$$< \psi_i >= \frac{1}{n_i} \int \psi_i(\vec{c}_i) f_i^1(\vec{c}_i, \vec{r}, t) d\vec{c}_i \tag{2.69}$$

Thus, the equation of change for the particle property of phase i may be expressed as

$$\sum_{p=1}^{N} < (\psi_{ci})\big|_p > = \frac{\partial}{\partial t}(n_i < \psi_i >) + \nabla \cdot (n_i < \psi_i \vec{c}_i >) - \frac{n_i}{m_i} < \vec{F}_{iext} \cdot \frac{\partial \psi_i}{\partial \vec{c}_i} > \tag{2.70}$$

$\sum_{p=1}^{N}(\psi_{ci})\big|_p$ is defined as the difference between the postcollisional and the precollisional properties of particle i due to all possible collisions with all the particles in the mixture. The collision of particle i with the other particles in the same phase results in the constitutive relation for each phase, and the interaction of phase i with other phases results in interfacial forces between particulates phases. The average of $\sum_{p=1}^{N}(\psi_{ci})\big|_p$ is defined as

$$\begin{aligned}\sum_{p=1}^{N} < (\psi_{ci})\big|_p > &= \sum_{p=1}^{N} < \psi_i^{'} - \psi_i > \big|_p \\ &= \sum_{p=1}^{N} \iiint \left(\psi_i^{'} - \psi_i\right) f_{ip}^2(\vec{r}_i, \vec{c}_i; \vec{r}_p, \vec{c}_p) d_{ip}^2 \left(\vec{c}_{ip} \cdot \vec{k}_{ip}\right) d\vec{k}_{ip} d\vec{c}_i d\vec{c}_p\end{aligned} \tag{2.71}$$

$f_{ip}^2 = f_{ip}^2(\vec{c}_i, \vec{r}_i; \vec{c}_p, \vec{r}_p)$ is the complete pair distribution function defined as the probability of finding, at time t, two particles i and p, such that they are centered on $\vec{r}_i$ and $\vec{r}_p$ and have velocities within the range $\vec{c}_i$, $\vec{c}_i + d\vec{c}_i$ and $\vec{c}_p$, $\vec{c}_p + d\vec{c}_p$

Following Jenkins and Savage (1983), the assumption of chaos along with the consideration of the correlation function allows us to write the pair distribution function as the product of the single velocity distributions, f_i^1 and f_p^1, weighted by the spatial pair distribution function at contact $g_{ip}(\varepsilon_i, \varepsilon_p)$,

$$f_{ip}^2\left(\vec{c}_i, \vec{r} - \frac{d_{ip}}{2}\vec{k}; \vec{c}_p, \vec{r} + \frac{d_{ip}}{2}\right) = g_{ip}(\varepsilon_i, \varepsilon_p) \cdot f_i^1\left(\vec{c}_i, \vec{r} - \frac{d_{ip}}{2}\vec{k}\right) \cdot f_p^1\left(\vec{c}_p, \vec{r} + \frac{d_{ip}}{2}\right) \tag{2.72}$$

where

$\vec{c}_{ip} = \vec{c}_i - \vec{c}_p$ is the relative instantaneous velocity and $d_{ip} = \frac{d_i + d_p}{2}$

$\vec{k}_{ip}$ is the unit vector connecting the centers of the two particles, located at $\vec{r}_i$ and $\vec{r}_p$, respectively, and directed from i to p. In the remaining text, we consider $\vec{k}_{ip} = \vec{k}$.

The collisional rate of production per unit of volume, $\sum_{p=1}^{N}\left(< \psi_i^{'} - \psi_i >\right)\big|_p$, was evaluated by Jenkins and Mancini (1989) as a sum of a symmetric (γ_{cip}) and antisymmetric (χ_{cip}) terms

$$\sum_{p=1}^{N} < \psi_i^{'} - \psi_i > \big|_p = \sum_{p=1}^{N} \left(-\nabla \cdot \chi_{cip} + \gamma_{cip}\right) \tag{2.73}$$

where

$$\chi_{cip} = -\frac{d_{ip}^3}{2}\iiint\left(\psi_i^{'} - \psi_i\right)f_{ip}^2\left(\vec{c}_i, \vec{r} - \frac{d_{ip}}{2}\vec{k}; \vec{c}_p, \vec{r} + \frac{d_{ip}}{2}\right)\vec{k}\left(\vec{c}_{ip}\cdot\vec{k}\right)d\vec{k}d\vec{c}_i d\vec{c}_p \tag{2.74}$$

$$\gamma_{cip} = d_{ip}^2\iiint\left(\psi_i^{'} - \psi_i\right)f_{ip}^2\left(\vec{c}_i, \vec{r} - \frac{d_{ip}}{2}\vec{k}; \vec{c}_p, \vec{r} + \frac{d_{ip}}{2}\right)\left(\vec{c}_{ip}\cdot\vec{k}\right)d\vec{k}d\vec{c}_i d\vec{c}_p \tag{2.75}$$

Here χ_{cip} and γ_{cip} are the collisional fluxes and sources, respectively. Substituting Eqs. (2.74) and (2.75) into the equation of change, Eq. (2.71), the continuity, momentum, and fluctuating energy equations were obtained for ψ_i equal to m_i, $m_i\vec{c}_i$, and $\frac{1}{2}m_i C_i^2$, respectively.

2.6.2 Continuity Equation

The continuity equation for the solid-phase i can be written as

$$\frac{\partial\varepsilon_i\rho_i}{\partial t} + \nabla\cdot\left(\varepsilon_i\rho_i\vec{v}_i\right) = 0 \tag{2.76}$$

$\varepsilon_i\rho_i = n_i m_i$ is the mass of phase i per unit volume of mixture, ε_i is its solid volume fraction, and ρ_i is density of phase i. Here $\vec{v}_i = <\vec{c}_i>$ is the mean velocity of the particle i. The instantaneous velocity $\vec{c}_i$ is defined as the sum of the average velocity, $\vec{v}_i$, and peculiar velocity, $\vec{C}_i$,

$\vec{c}_i = \vec{v}_i + \vec{C}_i$ with $<\vec{C}_i> = 0$

2.6.3 Momentum Equation

The momentum equation for phase i may be expressed as

$$\varepsilon_i\rho_i\frac{D}{Dt}(\vec{v}_i) + \nabla\cdot\left(\sum_{p=1}^{N}\overline{P}_{cip} + \overline{P}_{ki}\right) - \frac{\varepsilon_i\rho_i}{m_i}\vec{F}_{iext} = \sum_{p=1}^{N}\vec{F}_{Dip} \tag{2.77}$$

$$\text{with } \frac{D}{Dt} \text{ is the material derivative} \tag{2.78}$$

$$\overline{P}_{ki} = \rho_i\varepsilon_i <\vec{C}_i\vec{C}_i> \quad \text{is the kinetic pressure tensor} \tag{2.79}$$

$$\overline{P}_{cip} = \chi_{cip}(m_i \vec{c}_i) \text{ is the collisional pressure tensor} \tag{2.80}$$

$$\vec{F}_{Dip} = \gamma_{cip}(m_i \vec{c}_i) \text{ is the collisional momentum source} \tag{2.81}$$

2.6.4 Fluctuating Energy Equation

The fluctuating energy equation for solid-phase i can be expressed as

$$\frac{3}{2}\frac{\varepsilon_i \rho_i}{m_i}\frac{D\theta_i}{Dt} + \nabla \cdot \left(\vec{q}_{ki} + \sum_{p=1}^{N} \vec{q}_{cip}\right) - \left(\overline{P}_{ki} + \sum_{p=1}^{N} \overline{P}_{cip}\right) : \nabla \vec{v}_i = \sum_{p=1}^{N} \left(N_{ip} - \vec{v}_i \cdot \vec{F}_{Dip}\right) \tag{2.82}$$

where

$$\theta_i = \frac{1}{3} m_i < \vec{C}_i \cdot \vec{C}_i > , \tag{2.83}$$

θ_i is the granular temperature or the fluctuating granular energy of the solid-phase I,

$$\vec{q}_{ki} = \rho_i \varepsilon_i < \vec{C}_i C_i^2 > \text{ is the kinetic heat flux,} \tag{2.84}$$

$$\vec{q}_{cip} = \chi_{cip}\left(m_i c_i^2\right) \text{ is the collisional energy flux,} \tag{2.85}$$

$$N_{ip} = \gamma_{cip}\left(m_i c_i^2\right) \text{is the collisional energy dissipation flux.} \tag{2.86}$$

In the above governing equations, the relevant variables describing the flow field are the average velocities, the solid volume fractions, and the granular temperatures evaluated at location $\vec{r}$ of the center of the particle at time t.

2.6.5 Kinetic Equation

The kinetic equations that characterize the flow of a multiphase system are

$$\left(\frac{\partial}{\partial t} + \vec{c} \cdot \nabla + \frac{\vec{F}_{iext}}{m_i} \cdot \nabla_{\vec{c}}\right) f_i^1 =$$
$$\sum_{p=1}^{N} \frac{d_{ip}^2}{4} \int\int \left[g_{ip}\left(\vec{r}, \vec{r} + \vec{k} d_{ip}/2\right) f_i^1(\vec{c}_{i1}, \vec{r}, t) f_i^1\left(\vec{c}_{i2}, \vec{r} + \vec{k} d_{ip}/2, t\right) \right.$$
$$\left. - g_{ip}\left(\vec{r}, \vec{r} - \vec{k} d_{ip}/2\right) f_p^1(\vec{c}_{p1}, \vec{r}, t) f_p^1\left(\vec{c}_{p2}, \vec{r} + \vec{k} d_{ip}/2, t\right) \right] \left(\vec{c}_{ip} \cdot \vec{k}\right) d\vec{c}_p d\vec{k} \tag{2.87}$$

where $g_{ip}(\vec{r})$ is the spatial-pair radial distribution function when the particles i and p are in contact. A solution of Eq. (2.87) near the equilibrium was obtained using the Chapman–Enskog method (Ferziger and Kaper 1972; Chapman and Cowling 1970),

$$f_i^1 = f_i^0(1 + \varphi_i) \tag{2.88}$$

where f_i^0 is the Maxwellian velocity distribution

$$f_i^0 = n_i \left(\frac{m_i}{2\pi\theta_i}\right)^{3/2} \exp\left[-\frac{m_i C_i^2}{2\theta_i}\right] \tag{2.89}$$

and φ_i is a perturbation to the Maxwellian velocity distribution. It is a linear function of the first derivative of n_i, θ_i, and $\vec{v}_i$. Note that φ_i is function of the phase mean velocity, $\vec{v}_i$, and not the total flow velocity, because, as mentioned in the introduction, each kind of particle is treated as a separate phase and the interaction is at the interface. The radial distribution function $g_{ip}(\varepsilon_i, \varepsilon_p)$ describes a multisized mixture of hard spheres at contact. Iddir and Arastoopour (2005) modified the Lebowitz (1964) radial distribution function. This approach is in agreement with the results of molecular dynamics (MD) simulation obtained by Alder and Wainwright (1967) at both lower and higher solid volume fractions. This equation can be written as

$$g_{ip}(\varepsilon_i, \varepsilon_p) = \frac{\left[d_p g_{ii}(\varepsilon_i, \varepsilon_p) + d_i g_{pp}(\varepsilon_i, \varepsilon_p)\right]}{2d_{ip}} \tag{2.90}$$

$$\text{where} \quad g_{ii}(\varepsilon_i, \varepsilon_p) = \frac{1}{\left(1 - (\varepsilon_i + \varepsilon_p)/\varepsilon_{\max}\right)} + \frac{3d_i}{2} \sum_{p=1}^{N} \frac{\varepsilon_p}{d_p} \tag{2.91}$$

The expression of $g_{pp}(\varepsilon_i, \varepsilon_p)$ is obtained by simply interchanging the indices i and p.

For a more detailed explanation for constitutive relation expressions for all solid phases, see Iddir and Arastoopour (2005).

2.6.6 *Example: Numerical Simulation of Simple Shear Flow*

A binary solid mixture (1 and 2) with the same density was sheared between two infinite parallel plates set to move with relative velocities $\pm V_0/2$. The motion of the granular mixture was in only the x-direction and was considered fully developed so that all the flow parameters are only a function of y. In this study, x and y are the axes parallel and perpendicular to the plates, respectively, as shown in Fig. 2.1. In

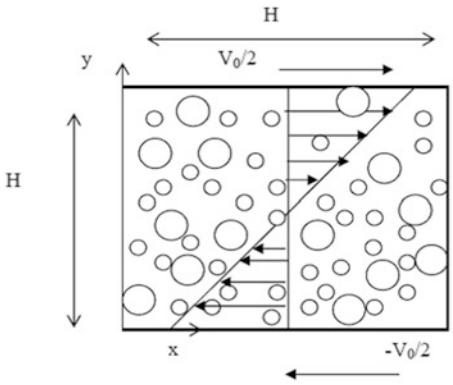

Fig. 2.1 Simple shear flow of a binary mixture (This figure was originally published in *AIChE Journal* 51, 2005 and has been reused with permission)

this example, the steady-state regime was considered, where the thermal equilibrium may be reached when the viscous effect due to continuous shearing is balanced by the dissipation due to collisions.

Simple shear flow is characterized by a linear profile of the velocity field (the shear rate, dv/dy, is constant). In this situation, the external forces are neglected, and the particles in the mixture move with the same center of mass average velocity, $\vec{v}$. This means that the granular temperatures, solid volume fractions, and gradient of the velocities are all uniform throughout the flow zone. Therefore, fluctuating energy equations for phases 1 and 2 reduce to the following nonlinear algebraic equations

$$-\left[\mu_{11}+\frac{\alpha_{12}}{2}\left(\frac{1}{\theta_1}+\frac{1}{\theta_2}\right)\right]\left(\frac{dv}{dy}\right)^2=N_{11}+N_{12} \tag{2.92}$$

$$-\left[\mu_{22}+\frac{\alpha_{12}}{2}\left(\frac{1}{\theta_1}+\frac{1}{\theta_2}\right)\right]\left(\frac{dv}{dy}\right)^2=N_{22}+N_{21} \tag{2.93}$$

where

$$\mu_{11}=\left[\frac{5}{16d_1^2g_{11}}\left(1+\frac{4}{5}(1+e)g_{11}\varepsilon_1\right)^2+\frac{4d_1(1+e)\varepsilon_1^2\rho g_{11}}{5m_1}\right]\sqrt{\frac{m_1\theta_1}{\pi}} \tag{2.94}$$

$$\mu_{22}=\left[\frac{5}{16d_2^2g_{22}}\left(1+\frac{4}{5}(1+e)g_{22}\varepsilon_2\right)^2+\frac{4d_2(1+e)\varepsilon_2^2\rho g_{22}}{5m_2}\right]\sqrt{\frac{m_2\theta_2}{\pi}} \tag{2.95}$$

$$\alpha_{12}=\frac{\sqrt{\pi}}{48}d_{12}^4g_{12}\frac{m_2m_1}{m_0^2}\left(\frac{m_1m_2}{\theta_1\theta_2}\right)^{3/2}(1+e)\rho^2\varepsilon_2\varepsilon_1\frac{1}{5}R_1 \tag{2.96}$$

$$N_{ip} = \frac{3}{4} d_{ip}^2 (e+1) g_{ip} \varepsilon_i \varepsilon_p \left(\frac{m_i m_p}{\theta_i \theta_p} \right)^{3/2} \frac{\sqrt{\pi}}{m_0} \cdot \left\{ B_{ip} \cdot R_5 + (e-1) \frac{m_p}{m_0} \frac{1}{6} \cdot R_1 \right\} \quad (2.97)$$

$$m_0 = m_1 + m_2 \quad (2.98)$$

$$B_{ip} = \frac{m_i m_p (\theta_p - \theta_i)}{2 m_0 \theta_i \theta_p} \quad (2.99)$$

$$R_1 = \frac{1}{A_{ip}^{3/2} D_{ip}^3} + \frac{9 B_{ip}^2}{A_{ip}^{5/2} D_{ip}^4} + \frac{30 B_{ip}^4}{2 A_{ip}^{7/2} D_{ip}^5} + \cdots \quad (2.100)$$

$$R_5 = \frac{1}{A_{ip}^{5/2} D_{ip}^3} + \frac{5 B_{ip}^2}{A_{ip}^{7/2} D_{ip}^4} + \frac{14 B_{ip}^4}{A_{ip}^{9/2} D_{ip}^5} + \cdots \quad (2.101)$$

The system of Eqs. (2.92) and (2.93) was solved numerically for θ_1 and θ_2, for the same flow parameters used by Galvin et al. (2005). The large particle mass, m_1 is 1. The ratio of the plate spacing to the large particle diameter H/d_1 is 4.45 or 9.8, depending on the total solid volume fraction and the solid volume fraction ratio. The ratio of H/d_1 was chosen in the MD simulation to avoid cluster formation (Hopkins and Louge 1991; Liss and Glasser 2001; Clelland and Hrenya 2002; Alam et al. 2002). Furthermore, the shear rate was set to a constant value of $V_0/H = \gamma = 1$.

The calculated granular temperatures for different diameter ratios using the Iddir and Arastoopour (2005) model were compared with the Jenkins and Mancini (1987) theoretical results and the MD simulation results of Galvin et al. (2005).

Figure 2.2 shows the variation of the fluctuating temperature ratio with the particle size ratio at different restitution coefficients for $\varepsilon_1/\varepsilon_2 = 0.5$. The Iddir and Arastoopour model predicts well the non-equipartition of energy of the two interacting particles for inelastic collisions. As observed by several investigations in the literature (e.g., Clelland and Hrenya 2002), the fluctuating granular temperature of the large particles increases relative to that of the small particles with an increase in large to small diameter ratio.

In the range of parameters investigated, equipartition was observed in two cases: first, when the restitution coefficient is higher than 0.99 and, second, when the two particles have the same mechanical properties ($\rho_1 = \rho_2$ and $d_1 = d_2$). We noticed that the restitution coefficient is the most important parameter responsible for non-equipartition. The effect of the restitution coefficient on the deviation of the granular temperature of two particles from each other is enhanced by the size disparity. For example, for $e = 0.99$, the ratio θ_1/θ_2 increases very slowly with the size ratio; however, for $e = 0.8$, a strong increase was observed for higher particle diameter ratios. Figure 2.3 shows the comparison between the calculated fluctuating energy ratio as a function of the diameter ratio based on the Iddir and Arastoopour (2005) model with the MD simulation and the theoretical results of

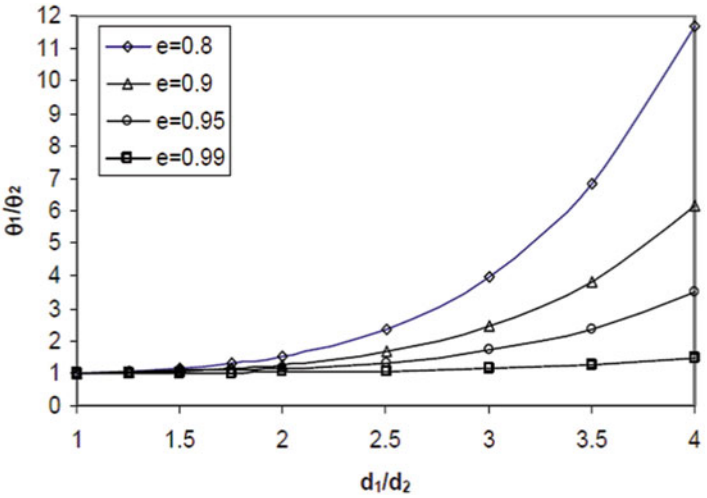

Fig. 2.2 Variation of the granular energy ratio with the diameter ratio for different restitution coefficients. $\rho_1/\rho_2 = 1$, $\varepsilon_T = 0.5$, and $\varepsilon_1/\varepsilon_2 = 0.5$. The subscripts 1 and 2 stand for large and small particles, respectively (This figure was originally published in *AIChE Journal* 51, 2005 and has been reused with permission)

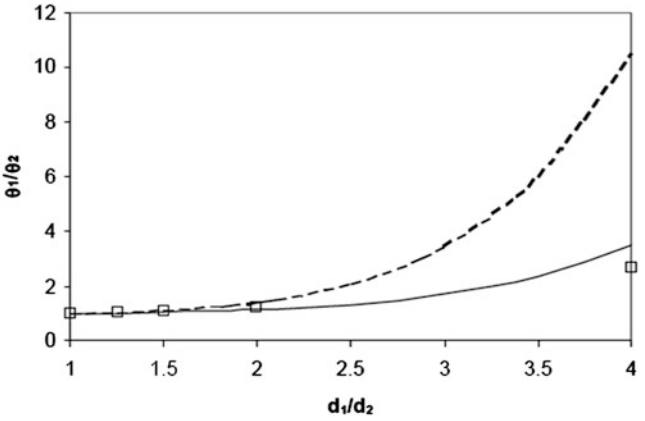

Fig. 2.3 Variation of the granular energy with the diameter ratio for $e = 0.95$, $\varepsilon_T = 0.5$, and $\varepsilon_1/\varepsilon_2 = 0.5$. Comparison of Iddir and Arastoopour model (2005) (*solid line*) with the theory of Jenkins and Mancini (1987) (*dashed line*) and the MD simulation results of Galvin et al. (2005) (*squares*) (This figure was originally published in *AIChE Journal* 51 (2005) and has been reused with permission)

Jenkins and Mancini (1987) at $\varepsilon_T = 0.5, \varepsilon_1/\varepsilon_2 = 0.5$, and a restitution coefficient of 0.95. Results given by the Iddir and Arastoopour (2005) model compared very well with the MD simulation results compared to those obtained by Jenkins and Mancini (1987). The deviation of the Jenkins and Mancini theory from the MD simulation

and the Iddir and Arastoopour results is more pronounced for low restitution coefficients and high diameter ratios. At a diameter ratio less than 1.5, both theories exhibit a good agreement with the MD simulation results.

2.7 Frictional Behavior of Granular Matters

Many industrially important gas–solid systems often include slow and dense solid flows, which is dominated by sustained frictional contacts between the particles. For simulations of these dense flows, in addition to the kinetic and collisional stresses (i.e., kinetic theory), the model should account for the frictional stresses as well, which could be calculated based on soil mechanics principles.

Makkawi and Ocone (2005) have reviewed the modeling approaches to include the frictional effects. The most common approach to consider the effect of frictional stresses is the kinetic frictional model based on the addition of stress from the two limiting regimes at a critical solid volume fraction (ε_{cr}) (Johnson and Jackson 1987; Syamlal et al. 1993; Ocone et al. 1993)

$$\tau_s = \tau_{kinetics-Collision} + \tau_{friction}$$

where

$$\tau_{friction} = 0 \quad \text{for } \varepsilon < \varepsilon_{cr} \tag{2.102}$$

$$\mu_s = \mu_{kinetics-Collision} + \mu_{friction}$$

where

$$\mu_{friction} = 0 \quad \text{for } \varepsilon < \varepsilon_{cr} \tag{2.103}$$

or switching between the two limiting regimes (Laux 1998; Makkawi and Ocone 2005) at a critical solid volume fraction as

$$\tau_s = \begin{cases} \max\left(\tau_{kinetics-Collision}, \tau_{friction}\right) & @\ \varepsilon > \varepsilon_{cr} \\ \tau_{kinetics-Collision} & @\ \varepsilon < \varepsilon_{cr} \end{cases}$$

This approach is based on the assumptions of Savage (1998) that consider the solid stress comes from the kinetic, collisional, and frictional contributions in an additive manner, where the frictional contributions appear only at higher solid volume fractions (i.e., greater than 0.5). Although, this approach lacks a strong physical justification and the hypothetical assumption of the critical solid volume fraction remains without experimental proof (Makkawi and Ocone 2005), the theory has been shown to capture the qualitative features of slow dense solid flows (Srivastava and Sundaresan 2003).

Most of the reported frictional stress models in the literature (Makkawi and Ocone 2005) and CFD codes such as Ansys and MFIX are based on the critical state theory of soil mechanics, where the shear stress τ_{fr} is described in terms of a frictional viscosity based on the work of Schaeffer (1987). Under a normal stress, a well-compacted granular material will shear only when the shear stress attains a critical magnitude. This is described by a Mohr–Coulomb law based on the laws of sliding friction. However, the Mohr–Coulomb law does not provide any information on how the granular material deforms and flows; rather, it describes the onset of yielding (Dartevelle 2003).

Schaeffer (1987) derived the following expression for the frictional stress, by assuming the system to be perfectly rigid-plastic, incompressible, non-cohesive, Coulomb powder with a yield surface of von Mises type, and the eigenvectors of the strain rate and stress tensors are parallel, as

$$\tau_{fr} = \frac{\sqrt{2} p_c \sin\varphi}{|S|} S \tag{2.104}$$

or equivalently

$$\mu_{fr} = \frac{p_c \sin\varphi}{\sqrt{4 II_{2D}}} \tag{2.105}$$

where φ is the angle of internal friction, II_{2D} is the second invariant of the deviatoric stress tensor S, and p_c is the critical state pressure. According to Srivastava and Sundaresan (2003), p_c increases monotonically with ε and is expected to become very large (i.e., diverge) as ε approaches random close packing ε_{max}. Various expressions have been proposed for the functional dependence of p_c on ε in the literature (Srivastava and Sundaresan 2003; Atkinson and Bransby 1978; Schaeffer 1987; Tardos 1997; Johnson and Jackson 1987; Savage 1998; Prakash and Rao 1988; Syamlal et al. 1993).

Johnson and Jackson (1987) proposed a critical state solid frictional pressure that allows for a slight compressibility with very limited particle concentration change (Makkawi and Ocone 2005). The Johnson and Jackson correlation for frictional pressure can be written as

$$p_f = p_c = \begin{cases} 0 & \text{elsewhere} \\ Fr. \dfrac{(\varepsilon_s - \varepsilon_{\min})^q}{(\varepsilon_{\max} - \varepsilon_s)^p} & \varepsilon_{\min} = 0.5 \le \varepsilon_s \le \varepsilon_{\max} = 0.63,\ q = 2,\ p = 3 \end{cases} \tag{2.106}$$

where Fr is a coefficient with different values reported in the literature from 0.05 to 5 (Johnson and Jackson 1987; O'Brien et al. 2010). The coefficient Fr was modified by others (Nikolopoulos et al. 2013; Abbasi 2013) assuming to be a function of the volume fraction as $Fr = 0.1\varepsilon_s$ while limiting the solid volume fraction to values less

than 0.629 to prevent divergence. Note that p_c is the critical state frictional pressure and many studies assumed the critical state frictional pressure is equal to solid frictional pressure p_f (Nikolopoulos et al. 2012; Abbasi and Arastoopour 2011; Tsuo and Gidaspow 1990), although clearly it is not an accurate assumption.

Srivastava and Sundaresan (2003) modified the Schaeffer expression for the frictional stress and also the Johnson and Jackson (1987) expression for the frictional pressure (see Eq. 2.108), to approximately account for strain rate fluctuations and slow relaxation of the assembly to the yield surface following Savage's (1998) argument of existence of fluctuations in the strain rate, even in purely quasi-static flow. The standard deviation σ of the fluctuations is related to the granular temperature of the powder θ (taken from the rapid granular flow regime) and the particle diameter d_p, as $\sigma = b\frac{\theta^{\frac{1}{2}}}{d_p}$, where b is a constant of order unity.

Laux (1998) suggested a correlation of the following form:

$$\mu_{fr} = \left[\frac{3\left|\xi_s \nabla . \vec{u}_s - \frac{p_f}{\varepsilon_s}\right|}{2\sqrt{3.II_{2D}}}\right]\left(\frac{6\sin\varphi}{9 - \sin^2\varphi}\right) \tag{2.107}$$

where p_f is calculated based on the following Srivastava and Sundaresan (2003) equation:

$$\frac{p_f}{p_c} = \left(1 - \frac{1}{n\sqrt{2}\sin\varphi}\frac{\nabla . \vec{u}_s}{\sqrt{S : S + \left(\theta/{d_p}^2\right)}}\right)^{\frac{1}{n-1}} \tag{2.108}$$

The angle of repose and, in turn, frictional forces for solid particles are significantly affected by the value of the compactness factor (n). The value for compactness factor (n) may be determined by comparing the experimental angle of repose with the calculated values for solid packing (Ghadirian 2016). Based on the above equation, if the granular material dilates as it deforms, $\nabla . u_s > 0$, then $p_f < p_c$ if it compacts as it deforms, $\nabla . u_s > 0$, then $p_f > p_c$ and when it deforms at constant volume, $\nabla . u_s = 0$, which is the critical state, $p_f = p_c$. This behavior is in line with the experimental measurements (see Das 1997). The value of n (the compactness factor) is different in the dilation and compaction parts of the system. Srivastava and Sundaresan (2003) suggested a value of $\frac{\sqrt{3}}{2}sin\varphi$ for the dilation branch, to ensure that the granular assembly is not required to sustain tensile stress on the yield surface. They also pointed out that n for the compaction branch can be any value marginally greater than one. They suggested that a value of 1.03 be used when no additional information is available. This value is measured for glass beads by Jyotsna and Rao (1997). It is worth mentioning that decreasing the value of n in the compactness branch will cause more deviation from the critical state frictional pressure. In other words, n may be an indicator for nonlinearity of the τ-σ relation.

With such a formulation, numerical singularity is avoided in regions where $S:S$ is zero as long as the granular temperature θ is nonzero. If, however, the physical system does contain regions where both $S:S$ and θ are zero (e.g., in a bin discharge problem, the stagnant shoulders at the bottom corners of the bin), the model will fail (Srivastava and Sundaresan 2003). However, their model captures four qualitative behaviors of a dense granular flow: (1) the height-independent rate of discharge of particles from a bin, (2) the dilation of particle assembly near the exit orifice, (3) the significant effect of the interstitial air on the discharge behavior of fine particles, and (4) the occurrence of pressure deficit above the orifice. In addition, in a bubbling fluidized bed, the model captured the significant effect of frictional stresses on the bubble shape.

Tardos et al. (2003) proposed another approach for intermediate granular flows, which smoothly merges the slow–intermediate regime with the rapid dilute flow (i.e., nonadditive approach). The continuous function may be written as (Nikolopoulos et al. 2012)

$$\mu_s = \mu_{kin} + \mu_{col} + \mu_{fric} \tag{2.109}$$

The basic assumption of this model is that the stress during particle flow is not constant but fluctuates around an average value. The model is restricted to the simple geometry of the Couette device and to an incompressible material:

$$\tau_s = p_s \sin\varphi.\tanh\left(\frac{\sqrt{\mathrm{K}\pi}}{2}\right) \tag{2.110}$$

where p_s is the solid pressure and is calculated from the kinetic theory. φ is the angle of internal friction, and K is a parameter defined in terms of the average strain rate $\langle S\rangle$ and its standard deviation, σ, such that $K = \left[\frac{\langle S\rangle}{2\sigma}\right]^2$. As concluded by Makkawi and Ocone (2005), by comparing various approaches, the superiority of these approaches is a matter of open debate and subject to further experimental validations.

Up to this point, all of the discussed approaches were based on the von Mises/Mohr–Coulomb law that, as mentioned earlier, does not provide any information on how the granular material deforms and flows. Although these models can properly simulate dilatancy, they do not capture consolidation (Dartevelle 2003). Therefore, the standard von Mises/Coulomb yield criterion cannot model the effect of compressibility phenomena (i.e., changes of bulk density) occurring in the returning system of circulating fluidized bed units and subsequently results in severe underestimation of the exerted frictional viscous forces (Nikolopoulos et al. 2013).

To overcome the shortcomings of the von Mises/Coulomb yield criterion, several modifications are proposed in the literature (Dartevelle 2003), such as the Gray yield criterion (Gray et al. 1991). The Gray yield criterion can be written as

$$f(\sigma,\ \tau) = \tau_p : \tau_p - (sin\varphi)^2\left[\left(p_p - \lambda\nabla\cdot\mu_s - \sigma\right)^2 - \sigma^2\right] = 0 \tag{2.111}$$

It should be mentioned that the Gray criterion reduces to the von Mises/Coulomb criterion if $\left(\rho_p - \lambda\nabla\cdot\mu_s - \sigma\right) = 0$ and $\sigma = p_p$ (in other words, these two yield criteria are the same if and only if $\nabla\cdot\mu_s = 0$, which is the case only at the critical state of the soil mechanics where solids deform without volume changes). The Gray yield criterion is based on the approximation that normal stresses in the particulate phase are caused not only by the pressure but also by the viscous normal stresses.

According to Dartevelle (2003), the plastic potential theory combined with the critical state approach can successfully describe the phenomenon of dilatancy, consolidation, and independence between the rate-of-strain tensor and the stress tensor. Using this approach assuming a slightly compressible, dry, non-cohesive, and perfectly rigid-plastic system, the expression for the frictional viscosity may be written

$$\mu_{fr} = \frac{p_s \sin^2\varphi}{\varepsilon_s\sqrt{4\sin^2\varphi.II_{2D} + (\nabla.\vec{u}_s)^2}} \tag{2.112}$$

and solid-phase bulk viscosity as

$$\xi_s = \frac{p_s}{\varepsilon_s\sqrt{4\sin^2\varphi.II_{2D} + (\nabla.\vec{u}_s)^2}} \tag{2.113}$$

Equation (2.113) reduces to Eq. (2.105) if, $\nabla.\vec{u}_s = 0$, corresponds to the critical state of soil mechanics and linear τ-σ relation. A detailed discussion and derivation of the models can be found in Dartevelle (2003).

Nikolopoulos et al. (2012)) have pointed out that the numerical results indicate that the values calculated by the Laux (Eq. 2.107) and Dartevelle (Eq. 2.112) expressions are of the same order of magnitude for values of solid volume fractions lower than 0.5. However, the Laux expression predicts higher solid frictional viscosity compared to the Dartevelle model for solid volume fractions higher than 0.55. Nikolopoulos et al. (2012) also showed that the results of simulations using the Dartevelle (2003) model are less accurate compared to the results of simulations using the Laux model in calculating the angle of repose.

2.8 Mass, Momentum, and Constitutive Equations

Tables 2.1 and 2.2 summarize the governing equations and constitutive equations for different regimes of fluid–particle flow.

Table 2.1 Two-fluid model governing equations

Conservation of mass

Gas phase

$$\frac{\partial}{\partial t}(\varepsilon_g \rho_g) + \nabla.(\varepsilon_g \rho_g \vec{v}_g) = \dot{m}_g \tag{T-1}$$

Solid phase

$$\frac{\partial}{\partial t}(\varepsilon_s \rho_s) + \nabla.(\varepsilon_s \rho_s \vec{v}_s) = \dot{m}_s \tag{T-2}$$

$$\varepsilon_g + \varepsilon_s = 1 \tag{T-3}$$

Conservation of momentum

Gas phase

$$\frac{\partial}{\partial t}\left(\varepsilon_g \rho_g \vec{v}_g\right) + \nabla \cdot \left(\varepsilon_g \rho_g \vec{v}_g \vec{v}_g\right) = -\varepsilon_g \nabla P + \nabla \cdot \tau_g + \varepsilon_g \rho_g g - \beta_{gs}\left(\vec{v}_g - \vec{v}_s\right) \tag{T-4}$$

Solid phase

$$\frac{\partial}{\partial t}\left(\varepsilon_s \rho_s \vec{v}_s\right) + \nabla \cdot \left(\varepsilon_s \rho_s \vec{v}_s \vec{v}_s\right) = -\varepsilon_s \nabla P + \nabla \cdot \tau_s - \nabla p_s + \varepsilon_s \rho_s g + \beta_{gs}\left(\vec{v}_g - \vec{v}_s\right) \tag{T-5}$$

Conservation of species

Gas phase

$$\frac{\partial}{\partial t}\left(\varepsilon_g \rho_g y_j\right) + \nabla \cdot \left(\varepsilon_g \rho_g \vec{v}_g y_j\right) = R_j \tag{T-6}$$

Solid phase:

$$\frac{\partial}{\partial t}(\varepsilon_s \rho_s y_i) + \nabla.(\varepsilon_s \rho_s \vec{v}_s y_i) = R_j \tag{T-7}$$

Conservation of solid phase fluctuating energy

$$\frac{3}{2}\left[\frac{\partial\left(\rho_s \varepsilon_s \theta\right)}{\partial t} + \nabla \cdot \left(\rho_s \varepsilon_s \theta v_s\right)\right] = \left(-P_s \mathbf{I} + \tau_s\right) : \nabla v_s + \nabla \cdot \left(k_s \nabla \theta\right) - \gamma + \phi_{gs} \tag{T-8}$$

Table 2.2 Two-fluid model constitutive equations

Gas phase stress

$$\tau_g = \varepsilon_g \mu_g \left[\nabla \vec{v}_g + \left(\nabla \vec{v}_g\right)^T\right] - \frac{2}{3}\varepsilon_g \mu_g \left(\nabla \cdot \vec{v}_g\right) I \tag{T-9}$$

Solid phase stress

$$\tau_s = \varepsilon_s \mu_s \left[\nabla \vec{v}_s + \left(\nabla \vec{v}_s\right)^T\right] - \varepsilon_s \left(\xi_s - \frac{2}{3}\mu_s\right) \nabla \cdot \vec{v}_s I \tag{T-10}$$

Collisional dissipation of solid fluctuating energy

$$\gamma_s = 3\left(1 - e^2\right)\varepsilon_s^2 \rho_s g_0 \theta \left(\frac{4}{d_p}\sqrt{\frac{\theta}{\pi}}\right) \tag{T-11}$$

Radial distribution function

$$g_0 = \left[1 - \left(\frac{\varepsilon_s}{\varepsilon_{s,\max}}\right)^{1/3}\right]^{-1} \tag{T-12}$$

Solid phase pressure

$$p_s = p_{kinetic} + p_{collision} = \varepsilon_s \rho_s \theta_s + 2\rho_s (1 + e_{ss}) \varepsilon_s^2 g_o \theta_s \qquad \varepsilon_s < \varepsilon_{s,fr} \tag{T-13}$$

$$p_s = p_{kinetic} + p_{collision} + p_{friction} \qquad \varepsilon_s \geq \varepsilon_{s,fr} \tag{T-14}$$

$$p_{critical} = Fr.\frac{(\varepsilon_s - \varepsilon_{\min})^q}{(\varepsilon_{\max} - \varepsilon_s)^p}, \qquad \varepsilon_{\min} = 0.5 \leq \varepsilon_s \leq \varepsilon_{\max} = 0.63, \quad Fr = 0.1\varepsilon_s, \quad q = 2, p = 3 \tag{T-15}$$

$$\frac{p_{friction}}{p_{critical}} = \left(1 - \frac{1}{n\sqrt{2}\sin\phi} \frac{\nabla . \vec{u}_s}{\sqrt{S : S + (\theta / d_p{}^2)}}\right)^{1/n-1} \tag{T-16}$$

Solid phase shear viscosity

$$\mu_s = \mu_{kin} + \mu_{col} + \mu_{fr} \tag{T-17}$$

$$\mu_{kin} = \frac{4}{5}\varepsilon_s \rho_s d_p g_0 (1 + e)\sqrt{\frac{\theta}{\pi}} \tag{T-18}$$

$$\mu_{col} = \frac{10\rho_s d_p \sqrt{\pi\theta}}{96(1+e) g_0 \varepsilon_s}\left[1 + \frac{4}{5} g_0 \varepsilon_s (1 + e)\right]^2 \tag{T-19}$$

$$\mu_{fr} = \left[\frac{3\left|\xi_s \nabla \vec{u}_s - \frac{p_s}{\varepsilon_s}\right|}{2\sqrt{3.II_{2D}}}\right]\left(\frac{6\sin\phi}{9 - \sin^2\phi}\right) \qquad \text{Laux (1998)} \tag{T-20}$$

(continued)

Table 2.2 (continued)

Solid phase bulk viscosity

$\xi_s = \frac{4}{3}\varepsilon_s \rho_s d_p g_0 (1+e)\sqrt{\frac{\theta}{\pi}}$	$\varepsilon_s < \varepsilon_{s,fr}$	Lun et al. (1984)	(T-21)
$\xi_s = \frac{p_s}{\varepsilon_s \sqrt{4\sin^2\phi . II_{2D} + \left(\nabla . \vec{u}_s\right)^2}}$	$\varepsilon_s \geq \varepsilon_{s,fr}$	Dartevelle (2003)	(T-22)

Conductivity of the fluctuating energy

$$\kappa_s = \frac{150\rho_s d_p \sqrt{\theta\pi}}{384(1+e)g_0}\left[1+\frac{6}{5}\varepsilon_s g_0 (1+e)\right]^2 + 2\rho_s \varepsilon_s^2 d_p (1+e) g_0 \sqrt{\frac{\theta}{\pi}} \quad \text{(T-23)}$$

where

$$\mathbf{q} = \kappa_s \nabla\theta \quad \text{(T-24)}$$

Granular energy exchange between phases

Laminar flow $\varphi_{gs} = -3\beta_{gs}\theta$ Gidaspow et al. (1992) (T-25)

Disperse turbulent flow $\varphi_{gs} = \beta_{gs}(\sqrt{2k_f}\sqrt{3\theta} - 2k_f)$ Sinclair and Mallo (1998) (T-26)

k_f is the turbulent kinetic energy of the gas phase.

Johnson and Jackson (1987) boundary condition for particles

$$v_{s,w} = -\frac{6\mu_s \varepsilon_{s,\max}}{\sqrt{3}\pi\phi\rho_s \varepsilon_s g_0 \sqrt{\theta}} \frac{\partial v_{s,w}}{\partial x} \quad \text{(T-27)}$$

$$\theta_w = -\frac{\kappa\theta}{\gamma_w}\frac{\partial\theta_w}{\partial x} + \frac{\sqrt{3}\pi\phi\rho_s \varepsilon_s v_{s,slip}^2 g_0 \theta^{3/2}}{6\varepsilon_{s,\max}\gamma_w} \quad \text{(T-28)}$$

$$\gamma_w = \frac{\sqrt{3}\pi\left(1-e_{sw}^2\right)\varepsilon_s \rho_s g_0 \theta^{3/2}}{4\varepsilon_{s,\max}} \quad \text{(T-29)}$$

(continued)

Table 2.2 (continued)

Interphase exchange (drag) coefficient

Modified Wen and Yu model (1966) for concentrated or non-homogeneous solid phase:

$$\beta_{gs} = \frac{3}{4}\frac{(1-\varepsilon_g)\varepsilon_g}{d_p}\rho_g\left|v_g - v_s\right|C_{D0}.H_d \tag{T-30}$$

where H_d is the heterogeneity factor (see Chapter 3 for more details)

$$Re_p < 1000; \qquad C_{D0} = \frac{24}{\mathrm{Re}_p}\left(1 + 0.15\,\mathrm{Re}_p^{0.687}\right) \tag{T-31}$$

$$Re_p \geq 1000; \qquad C_{D0} = 0.44 \tag{T-32}$$

$$\mathrm{Re}_p = \frac{\rho_g \varepsilon_g \left|\vec{v}_g - \vec{v}_s\right| d_p}{\mu_g} \tag{T-33}$$

Syamlal and O'Brien drag model (Syamlal et al. 1993) for very dilute or homogeneous solid phase:

$$\beta_{gs} = \frac{3}{4}\frac{(1-\varepsilon_g)\varepsilon_g}{d_p.v_{ts}^2}\rho_g\left|v_g - v_s\right|C_{D0}.\left(\frac{\mathrm{Re}_p}{v_{ts}}\right) \tag{T-34}$$

where v_{ts} is the particle terminal velocity,

$$v_{ts} = 0.5(A - 0.06\,\mathrm{Re}_p + \sqrt{(0.06\,\mathrm{Re}_p)^2 + 0.12\,\mathrm{Re}_p(2B - A) + A^2}) \tag{T-35}$$

with A and B having a form of

$$A = \varepsilon_g^{4.14} \qquad \text{and} \qquad B = \begin{cases} a\varepsilon_g^{1.28} & , \varepsilon_g \leq 0.85 \\ \varepsilon_g^{b} & , \varepsilon_g > 0.85 \end{cases} \tag{T-36}$$

a and $b$are the adjustable parameters.

2.9 Nomenclature

A	Avogadro's number
$\mathbf{c}$	Velocity space, m/s
$\vec{c}_s$	Instantaneous particle velocity in i direction, m/s
$\vec{C}_s$	Peculiar particle velocity, m/s
$d_{ip} = (d_i + d_p)/2$	Average diameter of particles i and p, m
$d_{s\ and,}\ d_p$	Diameter of particle, m
E	Internal energy, J
e	Restitution coefficient
e_{sw}	Particle–wall restitution coefficient frequency distribution of velocities of particles
$\vec{F}_{Dip}$	Momentum source (drag between solid phases), N
f_s^0	Maxwellian velocity distribution function
f_s^1	Single velocity distribution function
f_{ip}^2	Pair velocity distribution function
g	Gravity acceleration, m/s^2
g_0	Radial distribution function
g_{ip}	Radial distribution function at contact between particles i and p
g_{ss}	Radial distribution function at contact between particles of the same phase
H	Gap between two plates, m
$\bar{I}$	Identity tensor
k_B	The Boltzmann constant (1.3805×10^{-23} J/K)
$\vec{k} = \vec{k}_{ip}$	Unit vector connecting the centers of the two particles
K_f	Turbulent kinetic energy of fluid, m^2/s^2
k_s	Granular conductivity, kg/m·s
M	Molecular weight, kg/kmol
m_s	Mass of particle of phase s, kg
$m_0 = m_i + m_p$	Total mass of two colliding particles, kg
N	Number of moles
n	Compact factor
n_s	Number density of phase s
N_{ip}	Energy dissipation
$\overline{P}_c$	Collisional pressure tensor, N/m^2
$\overline{P}_k$	Kinetic pressure tensor, N/m^2
p_c	Critical state pressure, N/m^2
p_f	Frictional pressure, N/m^2
Q	Momentum flux, N/m^2
$\vec{q}_c$	Collisional flux, J/s·m^2
$\vec{q}_k$	Kinetic flux, J/s·m^2
R_j	Rate of heterogeneous reaction between phases, mol/m^2·s
Re_p	Particle Reynolds number

$\langle S \rangle$	Average strain rate
$\boldsymbol{r}$	Position
S	Deviatoric stress tensor
T	Average of random kinetic energy
$\mathbf{v}$	Hydrodynamic velocity, m/s
$\vec{v}$	Center of mass mean velocity, m/s
$\vec{v}_s$	Mean velocity of phase s, m/s
$\vec{V}_0$	Velocity of plates, m/s
$\vec{v}_{s,para}$	Particle slip velocity parallel to wall, m/s
v_{ts}	Solid particle terminal velocity, m/s
y_i	Species mass fraction

Subscripts

1	Large
2	Small
cr	Critical
fr	Frictional
g	Gas phase
col	Collisional
kin	Kinetic
max	Maximum
T	Total
s	Solid phase
w	Wall

Greek Symbols

χ_{ip}	Collisional flux, J/s·m^2
ε_s	Solid volume fraction of phase s
ε_T	Total solid volume fraction
φ_s	Perturbation to Maxwellian distribution function
γ_{ip}	Collisional source of granular temperature, J/m^2·s
μ	Viscosity, kg/m. s
μ_{ss}	Granular viscosity of phase s, kg/m. s
μ_{ip}	Mixture granular viscosity, kg/m. s
ρ_s	Solid density of phase s, kg/m^3
θ_s	Fluctuating granular energy m^2/s^2
θ_m	Mixture fluctuating granular energy, m^2/s^2
τ_N	Mixture normal stress, N/m^2
τ_s	Solid-phase shear stress, N/m^2
τ_t	Mixture shear stress, N/m^2
ψ_s	Property of particle
θ	Granular temperature (random kinetic energy per unit mass), m^2/s^2
ϕ	Specularity coefficient

φ Angle of internal friction
φ_{gs} Granular energy exchange between phases
ρ Bulk density, kg/m^3
ε_s Volume fraction of solids
ρ_s Solid density, kg/m^3
II_{2D} Second invariant of the deviatoric stress tensor
γ Shear rate, 1/s
β Interface momentum exchange coefficient
γ Collisional energy dissipation, J/m^3·s
ξ Solid-phase bulk viscosity, kg/m·s

References

Abbasi E (2013) Computational fluid dynamics and population balance model for simulation of dry sorbent based CO_2 capture process, PhD dissertation. Illinois Institute of Technology, Chicago, IL

Abbasi E, Arastoopour H (2011) CFD simulation of CO_2 sorption in a circulating fluidized bed using deactivation kinetic model. In: Knowlton TM (ed) Proceeding of the tenth international conference on circulating fluidized beds and fluidization technology, CFB-10, ECI, New York, pp 736–743

Alam M, Luding S (2003) Rheology of bidisperse granular mixtures via event-driven simulations. J Fluid Mech 476:69–103

Alam M, Willits JT, Arnarson BÖ, Luding S (2002) Kinetic theory of a binary mixture of nearly elastic disks with size and mass disparity. Phys Fluids 14(11):4085–4087

Alder BJ, Wainwright TE (1967) Velocity autocorrelations for hard spheres. Phys Rev Lett 18 (23):988

Arastoopour H (2001) Numerical simulation and experimental analysis of gas/solid flow systems: 1999 Fluor-Daniel Plenary lecture. Powder Technol 119(2):59–67

Arastoopour H, Lin SC, Weil SA (1982) Analysis of vertical pneumatic conveying of solids using multiphase flow models. AIChE J 28(3):467–473

Atkinson JH, Bransby PL (1978) The mechanics of soils: an introduction to critical state soil mechanics. McGraw-Hill Book Company, London, New York

Benyahia S (2008) Verification and validation study of some polydisperse kinetic theories. Chem Eng Sci 63(23):5672–5680

Benyahia S, Syamlal M, O'Brien TJ (2005) Evaluation of boundary conditions used to model dilute, turbulent gas/solids flows in a pipe. Powder Technol 156(2):62–72

Chapman S, Cowling TG (1970) The mathematical theory of non-uniform gases: an account of the kinetic theory of viscosity, thermal conduction and diffusion in gases. Cambridge University Press, Cambridge

Clelland R, Hrenya CM (2002) Simulations of a binary-sized mixture of inelastic grains in rapid shear flow. Phys Rev E 65(3):031301

Condiff DW, Lu WK, Dahler JS (1965) Transport properties of polyatomic fluids, a dilute gas of perfectly rough spheres. J Chem Phys 42(10):3445–3475

Dartevelle S (2003) Numerical and granulometric approaches to geophysical granular flows. Michigan Technological University, Houghton, MI

Das BM (1997) Advanced soil mechanics, 2nd edn. Taylor and Francis, Washington, DC

Ding J, Gidaspow D (1990) A bubbling fluidization model using kinetic theory of granular flow. AIChE J 36(4):523–538

Feitosa K, Menon N (2002) Breakdown of energy equipartition in a 2D binary vibrated granular gas. Phys Rev Lett 88(19):198301

Ferziger JH, Kaper HG (1972) Mathematical theory of transport processes in gases. North-Holland Publishing Company, Amsterdam
Galvin JE, Dahl SR, Hrenya CM (2005) On the role of non-equipartition in the dynamics of rapidly flowing granular mixtures. J Fluid Mech 528:207–232
Garzó V, Dufty JW (2002) Hydrodynamics for a granular binary mixture at low density. Phys Fluids 14(4):1476–1490
Ghadirian E (2016) PhD thesis, Illinois Institute of Technology
Gidaspow D (1994) Multiphase flow and fluidization: continuum and kinetic theory descriptions. Academic, California
Gidaspow D, Huilin L (1998) Equation of state and radial distribution functions of FCC particles in a CFB. AIChE J 44(2):279–293
Gidaspow D, Jiradilok V (2009) Computational techniques, Energy science, engineering and technology series. NOVA, New York
Gidaspow D, Bezburuah R, Ding J (1991) Hydrodynamics of circulating fluidized beds: kinetic theory approach (No. CONF-920502-1). Illinois Inst. of Tech., Chicago, IL, Dept. of Chemical Engineering
Goldshtein A, Shapiro M (1995) Mechanics of collisional motion of granular materials. Part 1. General hydrodynamic equations. J Fluid Mech 282:75–114
Gray DD, Stiles JM, Celik I (1991) Theoretical and numerical studies of constitutive. Contract No. DE-FC21-87MC24207
Hopkins MA, Louge MY (1991) Inelastic microstructure in rapid granular flows of smooth disks. Phys Fluids A 3(1):47–57
Huilin L, Wenti L, Rushan B, Lidan Y, Gidaspow D (2000) Kinetic theory of fluidized binary granular mixtures with unequal granular temperature. Phys A Stat Mech Appl 284(1):265–276
Huilin L, Gidaspow D, Manger E (2001) Kinetic theory of fluidized binary granular mixtures. Phys Rev E 64(6):061301
Iddir H, Arastoopour H (2005) Modeling of multitype particle flow using the kinetic theory approach. AIChE J 51(6):1620–1632
Iddir H, Arastoopour H, Hrenya CM (2005) Analysis of binary and ternary granular mixtures behavior using the kinetic theory approach. Powder Technol 151(1):117–125
Jenkins JT, Mancini F (1987) Balance laws and constitutive relations for plane flows of a dense, binary mixture of smooth, nearly elastic, circular disks. J Appl Mech 54(1):27–34
Jenkins JT, Mancini F (1989) Kinetic theory for binary mixtures of smooth, nearly elastic spheres. Phys Fluids A 1(12):2050–2057
Jenkins JT, Richman MW (1985) Kinetic theory for plane flows of a dense gas of identical, rough, inelastic, circular disks. Phys Fluids 28(12):3,485–3,494
Jenkins J, Savage SB (1983) Theory for the rapid flow of identical, smooth, nearly elastic, spherical particles. J Fluid Mech 130(1):187–202
Johnson PC, Jackson R (1987) Frictional-collisional constitutive relations for granular materials, with application to plane shearing. J Fluid Mech 176:67–93
Jyotsna R, Rao KK (1997) A frictional–kinetic model for the flow of granular materials through a wedge-shaped hopper. J Fluid Mech 346:239–270
Kim H, Arastoopour H (2002) Extension of kinetic theory to cohesive particle flow. Powder Technol 122(1):83–94
Laux H (1998) Modeling of dilute and dense dispersed fluid-particle flow. Norwegian University of Science and Technology, Trondheim
Lebowitz JL (1964) Exact solution of generalized Percus-Yevick equation for a mixture of hard spheres. Phys Rev 133(4A):A895
Liss ED, Glasser BJ (2001) The influence of clusters on the stress in a sheared granular material. Powder Technol 116(2):116–132
Lun CKK, Savage SB, Jeffrey DJ, Chepurniy N (1984) Kinetic theories for granular flow: inelastic particles in Couette flow and slightly inelastic particles in a general flowfield. J Fluid Mech 140:223–256

Makkawi Y, Ocone R (2005) Modelling the particle stress at the dilute-intermediate-dense flow regimes: a review. KONA Powder Part J 23:49–63

Nikolopoulos A, Nikolopoulos N, Varveris N, Karellas S, Grammelis P, Kakaras E (2012) Investigation of proper modeling of very dense granular flows in the recirculation system of CFBs. Particuology 10(6):699–709

Nikolopoulos A, Nikolopoulos N, Charitos A, Grammelis P, Kakaras E, Bidwe AR, Varela G (2013) High-resolution 3-D full-loop simulation of a CFB carbonator cold model. Chem Eng Sci 90:137–150

O'Brien TJ, Mahalatkar K, Kuhlman J (2010) Multiphase CFD simulations of chemical looping reactors for CO_2 capture. In: 7th international conference on multiphase flow, ICMF 2010, Tampa, FL

Ocone R, Sundaresan S, Jackson R (1993) Gas-particle flow in a duct of arbitrary inclination with particle-particle interactions. AIChE J 39(8):1261–1271

Prakash JR, Rao KK (1988) Steady compressible flow of granular materials through a wedge-shaped hopper: the smooth wall, radial gravity problem. Chem Eng Sci 43(3):479–494

Savage SB (1998) Analyses of slow high-concentration flows of granular materials. J Fluid Mech 377:1–26

Savage SB, Jeffrey DJ (1981) The stress tensor in a granular flow at high shear rates. J Fluid Mech 110:255–272

Savage SB, Sayed M (1984) Stresses developed by dry cohesionless granular materials sheared in an annular shear cell. J Fluid Mech 142:391–430

Schaeffer DG (1987) Instability in the evolution equations describing incompressible granular flow. J Differ Equ 66:19–50

Sinclair JL, Mallo T (1998) Describing particle-turbulence interaction in a two-fluid modelling framework. In Proc. of ASME fluids engineering division summer meeting (FEDSM'98), Washington, DC, June 21–25, pp 7–14

Srivastava A, Sundaresan S (2003) Analysis of a frictional-kinetic model for gas-particle flow. Powder Technol 129:72–85

Syamlal M, Rogers W, O'Brien TJ (1993) MFIX documentation: theory guide. National Energy Technology Laboratory, Department of Energy, Technical Note DOE/METC-95/1013 and NTIS/DE95000031

Tardos GI (1997) A fluid mechanistic approach to slow, frictional flow of powders. Powder Technol 92(1):61–74

Tardos GI, McNamara S, Talu I (2003) Slow and intermediate flow of frictional bulk powder in the Coquette geometry. Powder Technol 131:23–39

Tartan M, Gidaspow D (2004) Measurement of granular temperature and stresses in risers. AIChE J 50(8):1760–1775

Tsuo YP, Gidaspow D (1990) Computation of flow patterns in circulating fluidized beds. AIChE J 36:885–896

Wen CY, Yu YH (1966) Mechanics of fluidization. Chem Eng Prog Symp Ser 62:100

Wildman RD, Parker DJ (2002) Coexistence of two granular temperatures in binary vibrofluidized beds. Phys Rev Lett 88(6):064301

Willits JT, Arnarson BÖ (1999) Kinetic theory of a binary mixture of nearly elastic disks. Phys Fluids 11(10):3116–3122

Zamankhan P (1995) Kinetic theory of multicomponent dense mixtures of slightly inelastic spherical particles. Phys Rev E 52(5):4877

Chapter 3
Homogeneous and Nonhomogeneous Flow of the Particle Phase

3.1 Introduction

For simulation, design, and scale-up of commercial fluidized bed and gas–particle flow systems, a computationally feasible approach may be obtained from the averaged continuum equations of motion for both fluid and particles, which is often called the two-fluid model (TFM) (Arastoopour and Gidaspow 1979b, c; Gidaspow 1994; Arastoopour 2001). The continuum approach generally relies on closures for the solids stresses that most often are derived from granular kinetic theory in the kinetic–collisional regime and from soil mechanics in the dense–frictional regime. The averaging process leading to the TFM equations erases the details of flow at the level of individual particles; but their consequences appear in the averaged equations through terms such as drag force, for which one must develop constitutive relations (Gidaspow 1994; Arastoopour 2001; Sinclair and Jackson 1989). For example, in the momentum balance equations, constitutive relations are needed for the gas–particle interaction forces. Gas–particle flows in fluidized beds and riser reactors are inherently oscillatory, and they manifest in nonhomogeneous structures over a wide range of length and timescales. Thus, if one sets out to solve the microscopic TFM for gas–particle flows, grid sizes of the order of 10-particle diameter or smaller become essential (Igci et al. 2008; Benyahia 2012b). Moreover, such fine spatial resolution reduces the time steps required, further increasing the needed computational time. For most devices of practical (commercial) interest, it is nearly impossible to resolve all heterogeneous flow structures in large-scale industrial risers using a computational grid size of the order of a few particle diameters. In addition, such extremely fine spatial grids and small time steps are unaffordable and require significant computational time and use of significant computational facilities.

Gas–particle flows in large fluidized beds and risers often are simulated by solving discretized versions of the TFM equations over a coarse spatial grid. Such coarse grid simulations do not resolve the small-scale (i.e., subgrid scale)

H. Arastoopour et al., *Computational Transport Phenomena of Fluid-Particle Systems*,
Mechanical Engineering Series, DOI 10.1007/978-3-319-45490-0_3

spatial structures (Igci et al. 2008; Milioli et al. 2013). The effect of the large-scale structures using coarse grids must be accounted for through appropriate modifications to the closures.

One of the major sources of numerical inaccuracy for the TFM originates from the models used for the calculation of drag force (Nikolopoulos et al. 2013; Abbasi and Arastoopour 2011; Jang et al. 2010). The homogeneous drag models (Arastoopour et al. 1990; Syamlal and O'Brien 2003; Gidaspow 1994; Wen and Yu 1966) assume a homogeneous structure inside the control volumes, which is not valid due to the formation of clusters (dense phase) in the concentrated particulate phase (e.g., $\epsilon_s > 2\,\%$). The effective drag coefficient in the coarse grid simulations will be lower than that in the homogeneous TFM to reflect the tendency of the gas to flow more easily around the clusters (bypass the clusters) than through a homogeneous distribution of the particles (Igci et al. 2011; Benyahia 2009; Sarkar et al. 2014; Ghadirian and Arastoopour 2016).

Qualitatively, this is equivalent to an effectively larger apparent size for the particles. Therefore, any coarse grid continuum simulation of gas–solid flows should include subgrid corrections to the homogeneous drag force acting on the particles. As a matter of fact, the overprediction of drag force by the homogeneous models is significant and can lead to overprediction of solid circulation rates and underestimation of pressure drops in circulating fluidized beds (CFB) and overprediction of bed expansion in bubbling fluidized beds (BFB).

Arastoopour and Gidaspow (1979a) were the first to include the effect of clusters in the drag force between phases in gas–solid systems by assuming an effective particle diameter larger than the actual particle diameter and therefore reducing the drag force between phases. Recently, several approaches have been proposed to account for the effect of the small unresolved scales on the interphase momentum exchange when using the TFMs on coarse computational grids. Among them, two approaches have gained significant attention in the literature: filtered or subgrid and energy minimization multi-scale (EMMS).

Igci et al. (2008) and Milioli et al. (2013) derive residual correlations from filtering fully resolved simulations on a two-dimensional (2d) periodic domain with several average particle volume fractions. Igci et al. (2011) showed that the filtered TFM approach has shown promise to be a tool to simulate gas–particle flows of fluid catalytic cracking (FCC) particles in the industrial-scale riser of a CFB. Benyahia and Sundaresan (2012) also showed that the subgrid models for coarse grid simulations of continuum models may also be used for coarse grid simulations of discrete particle models.

The EMMS approach (Li and Kwauk 1994; Wang and Li 2007; Benyahia 2012a; Li et al. 2012; Ghadirian and Arastoopour 2016), on the other hand, is based on the assumption that heterogeneous structures (i.e., clusters) with different sizes form and contribute to the drag reduction between the gas and particulate phases. The resulting underdetermined set of equations is then solved by minimizing a function, called the stability condition. Physically, the stability criterion is the net energy exchange between phases to suspend and transport the solids.

3.2 Filtered or Subgrid Model

The TFM equations are coarse-grained through a filtering operation that amounts to spatial averaging over some chosen filter length scale. In these filtered (coarse-grained) equations, the consequences of the flow structures occurring on a scale smaller than a chosen filter size appear through residual correlations for which one must derive or postulate constitutive models (Igci et al. 2008). If constructed properly, and if the several assumptions innate to the filtering methodology hold true, the filtered equations should produce a solution with the same macroscopic features as the finely resolved kinetic theory model solution; however, obtaining this solution should come at less computational cost.

According to Igci et al. (2008), if $\varepsilon_s(y,t)$ denotes the particle volume fraction at location y and time t *is* obtained by solving the microscopic TFM, the filtered particle volume fraction $\overline{\varepsilon}_s(x,t)$ can be defined as

$$\overline{\varepsilon}_s(x,\ t)\ = \int_V G(x,\ y)\varepsilon_s(y,\ t)dy \tag{3.1}$$

where *G(x,y)* is a weight function that depends on x and y and V denotes the region over which the gas–particle flow occurs. The weight function satisfies $\int G(x,y)\, dy = 1$. By choosing how rapidly *G(x,y)* decays with distance measured from x, one can change the filter size. Igci et al. (2008) defined the fluctuation in particle volume fraction as

$$\varepsilon_s{}' = \varepsilon_s - \overline{\varepsilon}_s \tag{3.2}$$

For example, the filtered phase velocities are defined according to

$$\overline{\varepsilon}_s(x,\ t)\overline{v}_s(x,\ t)\ = \int_V G(x,\ y)\varepsilon_s(y,\ t)v_s(y,\ t)dy \tag{3.3}$$

$$\overline{\varepsilon}_g(x,\ t)\overline{v}_g(x,\ t) = \int_V G(x,\ y)\varepsilon_g(y,\ t)v_g(y,\ t)dy \tag{3.4}$$

v_g and v_s denote local gas- and particle-phase velocities appearing in the microscopic TFM.

Igci et al. (2008) then derived filtered continuity and momentum equations along with constitutive relations. For example, filtered gas–particle interaction force includes a filtered gas–particle drag force and a term representing correlated fluctuations in particle volume fraction and the (microscopic TFM) gas-phase stress gradient as

$$\beta_{fil}\left(\widetilde{v}_g - \widetilde{v}_s\right) = \overline{\beta_{micro}\left(\varepsilon_s, \left|v_g - v_s\right|\right)\left(v_g - v_s\right)} - \overline{\varepsilon_s'\nabla\cdot\tau_s'} \tag{3.5}$$

where β_{micro} is the drag coefficient in the microscopic TFM. Igci et al. (2008) also provided an algebraic form for the filtered drag coefficient as

$$\beta_{fil} = \frac{32\, Fr_f^{-2} + 63.02 Fr_f^{-1} + 129}{Fr_f^{-3} + 133.6 Fr_f^{-2} + 66.61 Fr_f^{-1} + 129} \beta_{micro} \tag{3.6}$$

Fr_f is the Froude number based on the filter size and is defined as

$$Fr_f = \frac{v_t^2}{g\Delta_f} \tag{3.7}$$

where v_t is the terminal settling velocity and $\Delta_f$is the filter size.

For further discussions on dependence of the residual correlations on the filter size, filtered particle volume fraction, and filtered slip velocity, all of which serve as a marker for the extent of subfilter-scale in-homogeneity, see Igci et al. (2008) and Milioli et al. (2013).

3.3 Energy Minimization Multi-Scale (EMMS) Approach

The energy minimization multi-scale (EMMS) approach was first proposed by Li and Kwauk (1994) based on the coexistence of both dense and dilute regions in a CFB reactor. The model parameters are found by minimization of the mass-specific energy consumption for suspending and transporting the particles as the stability criteria for flow structure inside the reactor (Benyahia 2012a).

The EMMS model is able to account for heterogeneous solid structures and cluster formation in the system. Benyahia (2012a) concluded that use of the EMMS-based drag model is accurate and necessary for the prediction of the averaged solid mass and pressure profile along the fully developed flow region of the riser.

Equations (T-1) through (T-9) in Table 3.1 show the EMMS drag model based on Wang et al. (2008) and Nikolopoulos et al. (2010). In this approach, the Wen and Yu (1966) drag model is multiplied by a heterogeneity factor, H_d, that is calculated by solving Eqs. (T-1) through (T-9) for minimization of Eq. (T-10). This is a nonlinear optimization problem that should be solved for any combination of u_g, u_s, and ε_g. Finally, the heterogeneity factor is calculated by Eq. (T-12) and is implemented in the computational fluid dynamics (CFD) code. Then the drag expression can be expressed as

$$\beta_{gs} = \frac{3}{4} \frac{(1-\varepsilon_g)\varepsilon_g}{d_p} \rho_g |v_g - v_s| C_{D0} . H_d \tag{3.8}$$

Table 3.2 presents the closure terms for the EMMS equations.

Table 3.1 EMMS governing equations

Force balance for clusters in unit volume of suspension:

$$\frac{3}{4}C_{dc}\frac{f(1-\varepsilon_c)}{d_p}\rho_g v_{sc}|v_{sc}| + \frac{3}{4}C_{di}\frac{f}{d_{cl}}\rho_g v_{si}|v_{si}| = f(1-\varepsilon_c)(\rho_s-\rho_g)(g+a_c) \quad \text{(T-1)}$$

Force balance for dilute phase in unit volume of suspension:

$$\frac{3}{4}C_{df}\frac{(1-f)(1-\varepsilon_f)}{d_p}\rho_g v_{sf}|v_{sf}| = f(1-\varepsilon_f)(\rho_s-\rho_g)(g+a_f) \quad \text{(T-2)}$$

Pressure drop balance between clusters and dilute phase:

$$C_{dc}\frac{(1-\varepsilon_c)}{d_p}\rho_g v_{sc}|v_{sc}| = \frac{f}{(1-f)}\frac{C_{di}}{d_{cl}}\rho_g v_{si}|v_{si}| + C_{df}\frac{(1-\varepsilon_f)}{d_p}\rho_g v_{sf}|v_{sf}| \quad \text{(T-3)}$$

Mass conservation for fluid:

$$v_f(1-f) + v_c f = v_g\varepsilon_g \quad \text{(T-4)}$$

Mass conservation for particles:

$$v_{pf}(1-f) + v_{pc}f = v_p\varepsilon_p \quad \text{(T- 5)}$$

Definition of mean voidage:

$$\alpha_g = f\varepsilon_c + (1-f)\varepsilon_f \quad \text{(T-6)}$$

Definition of voidage inside clusters:

$$\varepsilon_c = \varepsilon_g - n\sigma_\alpha,\ n = 2 \quad \text{(T-7)}$$

Dense phase voidage standard deviation:

$$\sigma_\alpha = \alpha_p\sqrt{\frac{(1-\varepsilon_p)^4}{1+4\varepsilon_p+4\varepsilon_p^2-4\varepsilon_p^3+\varepsilon_p^4}} \quad \text{(T-8)}$$

Mean cluster diameter:

$$d_{cl} = d_p + (0.027 - 10d_p)\varepsilon_p + 32\varepsilon_p^6 \quad \text{(T-9)}$$

Stability condition:

$$N_{ST} = \left|\frac{1}{(1-\alpha_g)\rho_p}\left[m_f F_f v_f + m_c F_c v_c + m_i F_i v_f(1-f)\right]\right| \to min \quad \text{(T-10)}$$

Effective drag force:

$$F_{EMMS} = \varepsilon_g\left[f(1-\varepsilon_c)(g+a_c) + (1-f)(1-\varepsilon_f)(g+\varepsilon_f)\right](\rho_s-\rho_g) \quad \text{(T-11)}$$

$$H_d(\varepsilon_g) = \frac{F_{EMMS}}{F_{Wen\ \&\ Yu}} \quad \text{(T-12)}$$

Table 3.2 Closure terms for the EMMS model

	Dense phase	Dilute phase	Interphase
Effective drag coefficient	$C_{dc} = c_{d0c}\varepsilon_c^{-4.65}$	$C_{df} = c_{d0f}\varepsilon_f^{-4.65}$	$C_{di} = c_{d0i}(1-f)^{-4.65}$
Standard drag coefficient	$C_{d0c} = \frac{24}{Re_c} + \frac{3.6}{Re_c^{0.313}}$	$C_{d0f} = \frac{24}{Re_f} + \frac{3.6}{Re_f^{0.313}}$	$C_{d0i} = \frac{24}{Re_i} + \frac{3.6}{Re_i^{0.313}}$
Reynolds number	$Re_c = \frac{\rho_d d_p}{\mu_g}\lvert v_{sc}\rvert$	$Re_f = \frac{\rho_d d_p}{\mu_g}\lvert v_{sf}\rvert$	$Re_i = \frac{\rho_d d_{cl}}{\mu_g}\lvert v_{if}\rvert$
Slip velocity	$v_{sc} = v_c - \frac{\varepsilon_c v_{pc}}{1-\varepsilon_c}$	$v_{sf} = v_f - \frac{\varepsilon_f v_{pf}}{1-\varepsilon_f}$	$v_{si} = (1-f)\left(v_f - \frac{\varepsilon_f v_{pc}}{1-\varepsilon_c}\right)$
Drag force	$F_c = C_{dc}\frac{\pi d_p^2}{4}\frac{\rho_g}{2}v_{sc}\lvert v_{sc}\rvert$	$F_f = C_{df}\frac{\pi d_p^2}{4}\frac{\rho_g}{2}v_{sf}\lvert v_{sf}\rvert$	$F_i = C_{di}\frac{\pi d_p^2}{4}\frac{\rho_g}{2}v_{si}\lvert v_{si}\rvert$
Number of particles in cluster	$m_c = \frac{f(1-\varepsilon_c)}{\frac{\pi d_p^3}{6}}$	$m_f = \frac{(1-f)(1-\varepsilon_f)}{\frac{\pi d_p^3}{6}}$	$m_i = \frac{f}{\frac{\pi d_{cl}^3}{6}}$

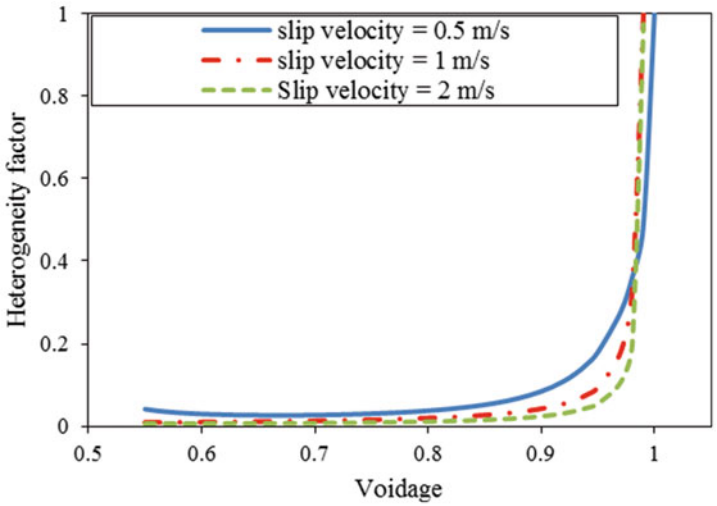

Fig 3.1 Heterogeneity factor (H_d) as a function of voidage at different slip velocities (This figure was originally published in *Powder Technol* 288, 2016 and has been reused with permission)

Ghadirian and Arastoopour (2016) calculated the heterogeneity factor H_d (the ratio of drag force for nonhomogeneous solid-phase flow using the EMMS approach to drag force calculated using the Wen and Yu drag expression for a homogeneous solid-phase flow system) as a function of voidage at different specific slip velocities for flow of gas and particles with 185 μm diameter and 2500 kg/m^3 density. Figure 3.1 shows the calculated heterogeneity factor H_d at slip velocities of 0.5, 1, and 2 m/s. As this figure shows, in very dilute regions of the system, the solid flow pattern approaches toward homogeneous flow. At regions with a solid volume fraction of less than 0.1, H_d initially decreases sharply, and then, for a wide range of

solid volume fraction greater than 0.15, it levels off at a value of about 0.02 for slip velocities between 0.5 and 2 m/s. This makes the EMMS calculated drag force for the nonhomogeneous solid phase significantly lower than the prediction of any homogeneous drag model. The sudden decrease in H_d is because of the presence of clusters that allow the gas to bypass the solids and therefore results in a considerable decrease in the drag force between phases. This figure also suggests that variations in H_d with respect to the solid volume fraction are more significant than H_d variations with respect to the slip velocity. Therefore, we may neglect the effect of slip velocity variation in most of the gas–solid flow systems.

Ghadirian and Arastoopour (2016) simulated bed expansion using 2D TFM CFD equations for both homogeneous and nonhomogeneous particle phases. They concluded that using a nonhomogeneous drag expression, such as EMMS, predicts the bed expansion with noticeably higher accuracy (20 % or less), while homogeneous models used in their study continued to overpredict the bed expansion by up to about 70 % in comparison with the correlation developed based on the experimental data of Krishna (2013).

Figure 3.2 shows the bed expansion factor (final bed height/initial bed height) for the EMMS (developed for 185 μm and 2500 kg/m^3 density particles) and two homogeneous models as well as the experimentally based correlation of Krishna (2013). To demonstrate the effect of particle type (particle size and density) on the heterogeneity of the system, the results of another set of simulations using the EMMS approach derived for FCC particles (Lu et al. 2009) are also shown in this

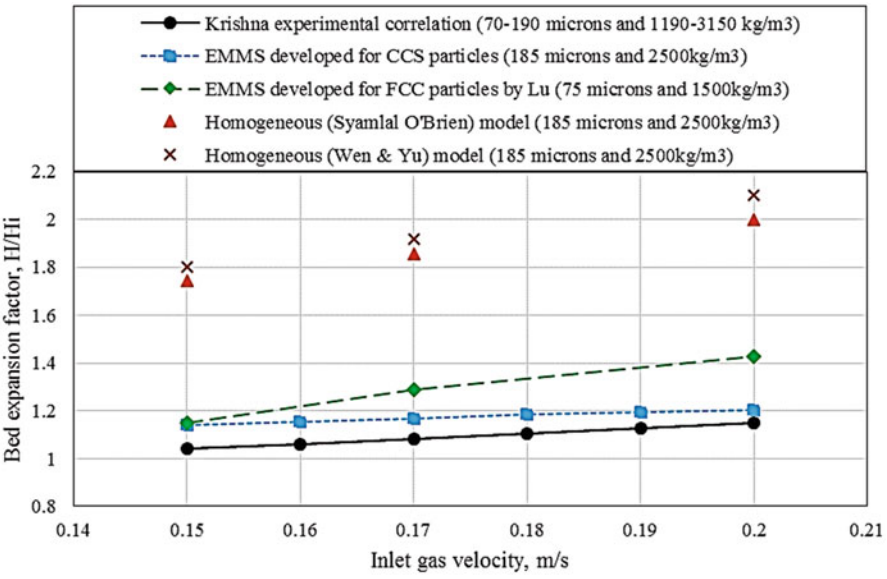

Fig. 3.2 Comparison of bed expansion factor as a function of inlet gas velocity using different drag models with experimental data (This figure was originally published in *Powder Technol* 288, 2016 and has been reused with permission)

figure. In the latter case, the EMMS approach was derived by Lu et al. (2009) for FCC particles (75 μm and 1500 kg/m^3), but the resulting heterogeneity factor is used to simulate 185 μm bed expansion and 2500 kg/m^3 particle density.

Figure 3.2 also shows that the homogeneous models predict a very high value for bed expansion with about 70 % deviation from the experimental correlation. Using the EMMS model, the bed expansion factor shows only less than 10 % deviation from the experimental values that could be within the experimental error. This graph also shows that the bed expansion calculated based on the EMMS approach derived for FCC particles improves the bed expansion predictions compared to the homogeneous model. It predicts experimental values within a 20 % deviation.

3.4 Nomenclature

a_c	Acceleration of particles in dense phase, m/s^2
a_f	Acceleration of particles in dilute phase, m/s^2
C_{Dc}	Effective drag coefficient in dense phase
C_{Df}	Effective drag coefficient in dilute phase
C_{Di}	Effective drag coefficient in interphase
d_p	Particle diameter, m
d_{cl}	Cluster diameter, m
f	Clusters volume fraction (m^3 of clusters/m^3 in control volume)
F	Drag force, N
Fr	Froude number
g	Gravitational acceleration, m/s^2
G	Weight function in filtered model
H_d	Heterogeneity index
m_c	Number of particles inside clusters per unit volume
m_f	Number of particles in dilute phase per unit volume
m_i	Number of cluster in control volume per unit volume
n	Constant in the equation of ε_c
N_{st}	Energy interchanged between flow phases, W/kg
v_g	Real gas velocity of gas in control volume, m/s
v_s	Real particle velocity in control volume, m/s
v_c	Superficial gas velocity in dense phase, m/s
v_f	Superficial gas velocity in dilute phase, m/s
v_{sc}	Superficial slip velocity in dense phase, m/s
v_{sf}	Superficial slip velocity in dilute phase, m/s
v_{si}	Superficial slip velocity in interphase, m/s
v_{pc}	Superficial particle velocity in dense phase, m/s
v_{pf}	Superficial particle velocity in dilute phase, m/s
v_t	Terminal settling velocity, m/s

Greek Symbols

β	Momentum exchange coefficient, kg/m^3 s
β_{micro}	Drag coefficient in microscopic two-fluid model
β_{fil}	Filtered drag coefficient
μ_g	Gas dynamic viscosity, kg/m. s
ρ_g	Gas density, kg/m^3
ρ_s	Particle density, kg/m^3
ε_g	Voidage, m^3 of gas/m^3 in control volume
ε_s	Volume fraction of particles, m^3 of particles/m^3 in control volume
ε_c	Voidage in dense volume, m^3 of gas/m^3 of dense phase
ε_f	Voidage in dilute volume, m^3 of gas/m^3 of dilute phase
ε_{mf}	Voidage at minimum fluidization
$\overline{\varepsilon}_s$,	Filtered particle volume fraction
ε_s'	Fluctuation in particle volume fraction
$\overline{\varepsilon}_g$,	Filtered gas volume fraction
ε_g'	Fluctuation in gas volume fraction
Δ_f	Filter size, m
σ_α	Dense phase voidage standard deviation

References

Abbasi E, Arastoopour H (2011) CFD simulation of CO_2 sorption in a circulating fluidized bed using deactivation kinetic model. In: Knowlton TM (ed) Proceeding of the tenth international conference on circulating fluidized beds and fluidization technology, CFB-10, ECI, New York, pp 736–743

Arastoopour H (2001) Numerical simulation and experimental analysis of gas/solid flow systems: 1999 Fluor-Daniel Plenary lecture. Powder Technol 119(2):59–67

Arastoopour H, Gidaspow D (1979a) Analysis of IGT pneumatic conveying data and fast fluidization using a thermohydrodynamic model. Powder Technol 22(1):77–87

Arastoopour H, Gidaspow D (1979b) Vertical countercurrent solids gas flow. Chem Eng Sci 34 (8):1063–1066

Arastoopour H, Gidaspow D (1979c) Vertical pneumatic conveying using four hydrodynamic models. Ind Eng Chem Fundam 18(2):123–130

Arastoopour H, Pakdel P, Adewumi M (1990) Hydrodynamic analysis of dilute gas-solids flow in a vertical pipe. Powder Technol 62:163–170

Benyahia S (2009) On the effect of subgrid drag closures. Ind Eng Chem Res 49(11):5122–5131

Benyahia S (2012a) Analysis of model parameters affecting the pressure profile in a circulating fluidized bed. AIChE J 58(2):427–439

Benyahia S (2012b) Fine-grid simulations of gas-solids flow in a circulating fluidized bed. AIChE J 58(11):3589–3592

Benyahia S, Sundaresan S (2012) Do we need sub-grid scale corrections for both continuum and discrete gas-particle flow models? Powder Technol 220:2–6

Ghadirian E, Arastoopour H (2016) CFD simulation of a fluidized bed using the EMMS approach for the gas-solid drag force. Powder Technol 288:35–44

Gidaspow D (1994) Multiphase flow and fluidization: continuum and kinetic theory descriptions. Academic, NewYork

Igci Y, Andrews AT, Sundaresan S, Pannala S, O'Brien T (2008) Filtered two-fluid models for fluidized gas-particle suspensions. AlChE J 54(6):1431–1448

Jang J, Rosa C, Arastoopour H (2010) CFD simulation of pharmaceutical particle drying in a bubbling fluidized bed reactor. In: Kim SD et al (eds) Fluidization XIII. ECI, New York, pp 853–860

Krishna BSVSR (2013) Predicting the bed height in expanded bed adsorption column using RZ correlation. Bonfring Int J Ind Eng Manage Sci 3(4):107

Li J, Kwauk M (1994) Particle-fluid two-phase flow: the energy-minimization multi-scale method. Metallurgy Industry Press, Beijing

Li F, Song F, Benyahia S, Wang W, Li J (2012) MP-PIC simulation of CFB riser with EMMS-based drag model. Chem Eng Sci 82:104–113

Lu B, Wang W, Li J (2009) Searching for a mesh-independent sub-grid model for CFD simulation of gas–solid riser flows. Chem Eng Sci 64(15):3437–3447

Milioli CC, Milioli FE, Holloway W, Agrawal K, Sundaresan S (2013) Filtered two-fluid models of fluidized gas-particle flows: new constitutive relations. AIChE J 59(9):3265–3275

Nikolopoulos A, Atsonios K, Nikolopoulos N, Grammelis P, Kakaras E (2010) An advanced EMMS scheme for the prediction of drag coefficient under a 1.2 MW CFBC isothermal flow—Part II: numerical implementation. Chem Eng Sci 65(13):4089–4099

Nikolopoulos A, Nikolopoulos N, Charitos A, Grammelis P, Kakaras E, Bidwe AR, Varela G (2013) High-resolution 3-D full-loop simulation of a CFB carbonator cold model. Chem Eng Sci 90:137–150

Sarkar A, Xin S, Sundaresan S (2014) Verification of sub-grid filtered drag models for gas-particle fluidized beds with immersed cylinder arrays. Chem Eng Sci 114:144–154

Sinclair JL, Jackson R (1989) Gas–particle flow in a vertical pipe with particle–particle interactions. AIChE J 35(9):1473–1486

Syamlal M, O'Brien TJ (2003) Fluid dynamic simulation of O_3 decomposition in a bubbling fluidized bed. AIChE J 49(11):2793–2801

Wang W, Li J (2007) Simulation of gas-solid two-phase flow by a multi-scale CFD approach—extension of the EMMS model to the sub-grid level. Chem Eng Sci 62(1):208–231

Wang J, Ge W, Li J (2008) Eulerian simulation of heterogeneous gas-solid flows in CFB risers: EMMS-based sub-grid scale model with a revised cluster description. Chem Eng Sci 63 (6):1553–1571

Wen CY, Yu YH (1966) Mechanics of fluidization. Chem Eng Prog Symp Ser 62:100–111

Chapter 4
Polydispersity and the Population Balance Model

4.1 Introduction to Polydisperse Systems and the Method of Moments Solution Technique

In fluid–particle flow systems, when the disperse-phase (e.g., particle phase) property distribution is wide or changing due to the particulate processes (such as changes in size distribution due to breakage, agglomeration, attrition, or growth or changes in disperse-phase density due to heterogeneous chemical reactions), use of average values for disperse-phase properties is no longer accurate. Successful computational fluid dynamics (CFD) simulations of polydisperse flows must include the distribution of particulate phase properties and its variation caused by the particulate processes.

One method to account for polydispersity in the system is using a multi-fluid model by dividing the disperse phase into different classes based on the desired property by assigning one fluid for each class. As discussed in Chap. 2, Iddir and Arastoopour (2005) extended the kinetic theory to granular mixtures of different mechanical properties (size, density, and/or restitution coefficient) for multi-type particle systems where each particle group was considered as a separate phase with different average velocity and granular energy. An alternative method to account for polydispersity of the particulate phase is based on the population balance approach. This approach is expected to be computationally more attractive and is also able to account for changes in the disperse-phase property distributions.

The population balance equation (PBE) is a balance equation based on the number density function and accounts for the spatial and temporal evolutions of the particulate phase internal variable distribution function in a single control volume. This equation is an integrodifferential equation and involves both integrals and derivatives of the distribution function.

Ramkrishna (2000) and Vanni (2000) provided a comprehensive review of the subject of PBE in terms of formulation of PBE, solution techniques, applications,

H. Arastoopour et al., *Computational Transport Phenomena of Fluid-Particle Systems*,
Mechanical Engineering Series, DOI 10.1007/978-3-319-45490-0_4

and theoretical considerations. Solution methods of PBE include method of successive approximations, method of Laplace transform, method of moments (MOM), method of weighted residuals (MWR), discrete formulations for the solution, and the Monte Carlo method. Among them, MOM is widely accepted as a computationally attractive method and has gained significant attention.

MOM is based on solving the distribution function transport equation in terms of its lower-order moments. For fluid–particle flow systems, some of the variables in PBE need to be calculated from the CFD model, and, in turn, solution of PBE gives some of the phase properties needed in the CFD model. Therefore, PBE and CFD need to communicate via a two-way coupling. However, in its original form, this method is capable of modeling only very simple particulate processes due to some mathematical limitations (e.g., closure problem) (Strumendo and Arastoopour 2008). To overcome these limitations, different solution methods have been proposed by many researchers. The various forms of MOM can be expressed in four categories:

4.1.1 Classical Method of Moments (MOM)

In this approach, the functional form of the property (i.e., size) distribution function is assumed, while the unknown parameters in the distribution function are independent of the internal variables and can be computed as a function of the moments (Barrett and Webb 1998). Although in some cases these methods can provide good results and at the same time are not computationally intensive, the obvious drawbacks are that they are not general and they require that the functional form of the distribution function does not change during the process (Strumendo and Arastoopour 2008).

4.1.2 Quadrature Method of Moments (QMOM)

In this approach, no explicit assumption is made regarding the form of the size distribution function, and the integrals appearing in the moment equations are computed numerically by means of quadrature formulas. This technique was first presented by McGraw (1997) and later applied to different processes by others (Barrett and Webb 1998; Marchisio et al. 2003a, b). Using this approach, McGraw computed the evolution of the moment equations correctly and efficiently (from a computational point of view). Different from the methods of the first category, this method can be considered general because no explicit assumption is made regarding the functional form of the distribution function. On the other hand, in QMOM, the solution is given in terms of the moments, while the size distribution function disappears from the governing equations. The reconstruction of the distribution function from the moments (Diemer and Olson 2002a, b), if possible, can be rather

complex (Strumendo and Arastoopour 2008). In QMOM, reconstruction of the distribution function is achieved using the moment-inversion algorithm through approximation of the distribution function by Dirac delta functions. However, the positivity of the number density function cannot be guaranteed by QMOM (Yuan 2013). To overcome this problem, the conditional quadrature method of moments (CQMOM) has been proposed by Yuan and Fox (2011). In CQMOM, the moment-inversion algorithm is based on one-dimensional (1D) adaptive quadrature of conditional velocity moments and is shown to always yield realizable distribution functions (i.e., nonnegative quadrature weights). CQMOM can be used to compute exact N-point quadratures for multi-valued solutions (also known as the multivariate truncated moment problem) and provides optimal approximations of continuous distributions. In order to control numerical errors arising in volume averaging and spatial transport, an adaptive 1D quadrature algorithm is formulated for use with CQMOM (Yuan and Fox 2011). However, one drawback still exists with CQMOM, which is the inability of the method to provide explicit values for the density function.

To overcome this problem, Yuan et al. (2012) proposed a method called extended quadrature method of moments (EQMOM) by generalizing the quadrature formula with kernel density functions with finite or infinite support parameters**.** The parameter value is determined by fixing one additional moment. The advantage of this method over the QMOM is that, with one additional moment, it is possible to reconstruct a smooth and nonnegative distribution function that closely reproduces the moment set (Marchisio and Fox 2013). Compared to CQMOM, it uses explicit values for the distribution function. For details of this method, see Yuan (2013).

4.1.3 Direct Quadrature Method of Moments (DQMOM)

This is another version of the quadrature-based methods that has been proposed by Marchisio and Fox (Marchisio and Fox 2005) to overcome some disadvantages of QMOM when dealing with (1) multivariate distributions and (2) systems with a strong dependency of the disperse-phase velocity on the internal variables (Strumendo and Arastoopour 2008). DQMOM differs from QMOM because the abscissas and the weights of the quadrature approximation are tracked directly (rather than the moments, as in QMOM). Furthermore, an explicit expression for the particle distribution function is given in terms of a summation of Dirac delta functions. However, this method also suffers from the previously mentioned drawbacks of QMOM and CQMOM due to the use of Dirac delta function approximation.

4.1.4 *Finite Size Domain Complete set of Trial Functions Method of Moments (FCMOM)*

Strumendo and Arastoopour (Strumendo and Arastoopour 2008, 2010) introduced a new version of method of moments called Finite size domain Complete set of trial functions Method of Moments (FCMOM), which can be regarded as the fourth category of these methods. The method has unique advantages including fast convergence to the exact solution and provision of the solution of PBE in terms of the moments of the distribution and the reconstructed distribution function itself, which makes it distinct from other available approaches. The method has been validated against available analytical solutions or self-similar solutions for the growth, aggregation, dissolution, and simultaneous growth and aggregation cases in both univariate and bivariate homogeneous flows. In addition, FCMOM has been formulated for inhomogeneous systems without breakage or aggregation, and its performance was excellent in all of the cases (Strumendo and Arastoopour 2008, 2010). The applicability of the method in simulations of a complex system (e.g., inhomogeneous with particulate processes) using the multiphase CFD approach was recently studied by Abbasi and Arastoopour (2013). In this chapter, we will discuss the fundamentals of PBE and FCMOM and the coupling of FCMOM with the two-fluid model (TFM).

4.2 Population Balance Equation

The population balance equation (PBE) is a balance equation based on the number density function $f(\xi; \mathbf{x}, t)$, where ξ and $\mathbf{x}$ are internal and external coordinates, respectively. PBE accounts for the spatial and temporal evolutions of the number density function in a single control volume. Depending on the system of interest, the number density function $f(\xi; \mathbf{x}, t)$ may have only one internal coordinate (i.e., particle size) or multiple coordinates, such as particle size and surface area (Marchisio et al. 2003a). Here we consider only a univariate system with the particle size ($\boldsymbol{\xi}$) being the only internal coordinate.

For an inhomogeneous particulate system, the general governing equation becomes

$$\frac{\partial f(\boldsymbol{\xi};\mathbf{x},t)}{\partial t} + \frac{\partial}{\partial x_i}\left[v_p(\boldsymbol{\xi};\mathbf{x},t) f(\boldsymbol{\xi};\mathbf{x},t)\right] + \frac{\partial}{\partial \xi_j}\left[\frac{\partial \xi_j}{\partial t} f(\boldsymbol{\xi};\mathbf{x},t)\right] - \frac{\partial}{\partial x_i}\left[D_{pt}(\boldsymbol{\xi};\mathbf{x},t)\frac{f(\boldsymbol{\xi};\mathbf{x},t)}{\partial x_i}\right] = h(\boldsymbol{\xi};\mathbf{x},t) \tag{4.1}$$

The terms on the left-hand side are the accumulation term, convective term with respect to the external coordinate, convective term with respect to the internal

coordinate, and diffusive term, respectively. In the third term, $\frac{\partial \xi_i}{\partial t}$ is the flux in ξ-*space* (Marchisio et al. 2003a) or, in other words, the growth rate of the internal variable ξ (e.g., size). v_p and D_{pt} are particle-phase velocity and turbulent diffusivity, respectively, which generally are functions of time, location, and internal coordinates.

The source term $h(\xi; \mathbf{x}, t)$ on the right-hand side accounts for the net rate of introduction of new particles into the system. It assumes that aggregation/coalescence and breakage are the only mechanisms causing birth and death of particles or droplets in the system. The aggregation/coalescence source term could be written in the form of the right-hand side of the classical Smoluchowski equation (Smoluchowski 1917):

$$\frac{df(\xi; \mathbf{x}, t)}{dt} = \frac{1}{2}\int_0^{\xi} \beta(\xi - \eta, \eta).f\left(\xi - \eta; \mathbf{x}, t\right).f(\eta; \mathbf{x}, t)d\eta - f(\xi; \mathbf{x}, t).\int_0^{\infty} \beta(\xi, \eta).f(\eta; \mathbf{x}, t)d\eta \tag{4.2}$$

On the right-hand side of Eq. (4.2), the first term accounts for birth of particles with size ξ due to aggregation or coalescence of two smaller particles with size $\xi - \eta$ and η; the second term represents the death of particles with size ξ due to aggregation or coalescence with particles of all other sizes. β is the aggregation kernel, which gives the frequency that particles of size $\xi - \eta$ and η collide to form particles of size ξ. Aggregation/coalescence usually depends on particle-particle interactions, local shear rate, and fluid-particle properties.

Similarly, the net rate of introduction of new particles of size ξ into the system due to breakage can be defined as

$$\frac{df(\xi; \mathbf{x}, t)}{dt} = \int_{\xi}^{\infty} a(\eta).b\left(\xi|\eta\right).f(\eta; \mathbf{x}, t)d\eta - a(\xi)f(\xi; \mathbf{x}, t) \tag{4.3}$$

where a is the breakage kernel which gives the rate of breakage of a particle of a certain size and $b(\xi\ /\eta)$ is the daughter-size distribution function on breakage of particles of size λ (Marchisio et al. 2003a; Marchisio and Fox 2005).

4.3 Finite Size Domain Complete set of Trial Functions Method of Moments (FCMOM) Approach

In all of the solution methods based on the method of moments (MOM), the key is writing the transport equation (PBE) in terms of the lower-order moments of the number density function, f, in a closed form (Marchisio et al. 2003a). The i^{th} moment of the number density function is defined as

$$\mu_i = \int_0^{\infty} \xi^i . f(\xi; \mathrm{x}, t) d\xi \tag{4.4}$$

Using FCMOM, the solution of PBE is sought in the finite interval between the minimum and maximum values of the particle property (e.g., size), instead of in the [0,∞] range (Strumendo and Arastoopour 2008). In general form, the evolution of the number density function is tracked by imposing moving boundary conditions. After reformulating PBE in the standard interval [−1, +1] by a coordinate transformation as Strumendo and Arastoopour (2008),

$$\overline{\xi} = \frac{\{\xi - [\xi_{\min}(t) + \xi_{\max}(t)]/2\}}{[\xi_{\min}(t) + \xi_{\max}(t)]/2} \text{ and } \overline{\xi} \in [-1, +1] \tag{4.5}$$

where the dimensionless (divided by an appropriate scale factor) size distribution function $\overline{f}\left(\overline{\xi}; x, t\right)$ is represented as a series expansion by a complete system of orthonormal functions (e.g., Legendre polynomials). Writing the distribution function in terms of a series expansion of Legendre polynomials gives

$$\overline{f}\left(\overline{\xi}; \mathbf{x}, t\right) \approx \sum_{n=0}^{M-1} c_n(t, \mathbf{x}) . \phi_n\left(\overline{\xi}\right) \tag{4.6}$$

where the coefficient c_n e can be expressed in terms of the moments

$$c_n = \sqrt{\frac{2n+1}{2}} . \frac{1}{2^n} . \sum_{v=0}^{n} (-1)^{n-v} . \frac{(2v)!}{[(2v-n)!]} . \left\{ \frac{1}{[(n-v)!] . [(v)!]} \right\} . \mu_{2v-n} \tag{4.7}$$

and where the terms with negative moments order ($2v - n < 0$) are omitted (Strumendo and Arastoopour 2008).

The orthonormal functions, $\phi_n\left(\overline{\xi}\right)$, associated with the Legendre polynomials $P_n\left(\overline{\xi}\right)$ are

$$\phi_n\left(\overline{\xi}\right) = \sqrt{\frac{2n+1}{2}} . P_n\left(\overline{\xi}\right) \tag{4.8}$$

Therefore, a set of transport equations for the moments of the distribution function, f, could be derived from the general PBE (4.1) in the interval of [−1, +1], as presented in Eq. (4.9):

$$\begin{aligned} &\frac{\partial \mu_i}{\partial t} + v_{p,j} \frac{\partial \mu_i}{\partial x_j} - \frac{\partial}{\partial x_j} \left[\int_{-1}^{+1} D'_{pt} \frac{\partial \overline{f'}}{\partial x_j} \left(\overline{\xi}\right)^i d\overline{\xi} \right] \\ &\quad = -\left(MB + MB_{Conv} + MB_{Diff1} + MB_{Diff2} + MB_{Diff3} + IG\right) + S \end{aligned} \tag{4.9}$$

On the right-hand side of the moments evolution, Eq. (4.9), the first five terms are due to the coordinate transformation, IG is due to the Integration of the Growth term, and S is the source term due to the aggregation and breakage. These terms are:

$$MB = -\left\{\left[\overline{f'_{+1}} - (-1)^i.\overline{f'_{-1}}\right] - i.\mu_{i-1}\right\}.\frac{1}{(\xi_{\max} - \xi_{\min})}.\left(\frac{d\xi_{\min}}{dt} + \frac{d\xi_{\max}}{dt}\right)$$
$$-\left\{\left[\overline{f'_{+1}} - (-1)^{i+1}.\overline{f'_{-1}}\right] - (i+1).\mu_i\right\}.\frac{1}{(\xi_{\max} - \xi_{\min})}.\left(-\frac{d\xi_{\min}}{dt} + \frac{d\xi_{\max}}{dt}\right) \tag{4.10}$$

$$MB_{Conv} = -\left\{\left[\overline{f'_{+1}} - (-1)^i.\overline{f'_{-1}}\right] - i.\mu_{i-1}\right\}.\frac{v_{p,j}}{(\xi_{\max} - \xi_{\min})}.\left(\frac{\partial\xi_{\min}}{\partial x_j} + \frac{\partial\xi_{\max}}{\partial x_j}\right)$$
$$-\left\{\left[\overline{f'_{+1}} - (-1)^{i+1}.\overline{f'_{-1}}\right] - (i+1).\mu_i\right\}.\frac{v_{p,j}}{(\xi_{\max} - \xi_{\min})}.\left(-\frac{\partial\xi_{\min}}{\partial x_j} + \frac{\partial\xi_{\max}}{\partial x_j}\right) \tag{4.11}$$

$$MB_{Diff1} = \frac{1}{(\xi_{\max} - \xi_{\min})}\left(\frac{\partial\xi_{\min}}{\partial x_j} + \frac{\partial\xi_{\max}}{\partial x_j}\right)\int_{-1}^{+1}\frac{\partial D'_{pt}}{\partial x_j}\frac{\partial\overline{f'}}{\partial\overline{\xi}}(\overline{\xi})^i d\overline{\xi}$$
$$+\frac{1}{(\xi_{\max} - \xi_{\min})}\left(-\frac{\partial\xi_{\min}}{\partial x_j} + \frac{\partial\xi_{\max}}{\partial x_j}\right)\int_{-1}^{+1}\frac{\partial D'_{pt}}{\partial x_j}\frac{\partial\overline{f'}}{\partial\overline{\xi}}(\overline{\xi})^{i+1} d\overline{\xi} \tag{4.12}$$

$$MB_{Diff2} = \frac{2}{(\xi_{\max} - \xi_{\min})}\left(\frac{\partial\xi_{\min}}{\partial x_j} + \frac{\partial\xi_{\max}}{\partial x_j}\right)\int_{-1}^{+1} D'_{pt}\frac{\partial^2\overline{f'}}{\partial x_j\partial\overline{\xi}}(\overline{\xi})^i d\overline{\xi}$$
$$+\frac{2}{(\xi_{\max} - \xi_{\min})}\left(-\frac{\partial\xi_{\min}}{\partial x_j} + \frac{\partial\xi_{\max}}{\partial x_j}\right)\int_{-1}^{+1} D'_{pt}\frac{\partial^2\overline{f'}}{\partial x_j\partial\overline{\xi}}(\overline{\xi})^{i+1} d\overline{\xi}$$
$$-\frac{1}{(\xi_{\max} - \xi_{\min})^2}\left[\left(\frac{\partial\xi_{\min}}{\partial x_j} + \frac{\partial\xi_{\max}}{\partial x_j}\right)\right]^2\int_{-1}^{+1} D'_{pt}\frac{\partial^2\overline{f'}}{\partial\overline{\xi}^2}(\overline{\xi})^i d\overline{\xi}$$
$$-\frac{1}{(\xi_{\max} - \xi_{\min})^2}.2.\left(\frac{\partial\xi_{\min}}{\partial x_j} + \frac{\partial\xi_{\max}}{\partial x_j}\right)\left(-\frac{\partial\xi_{\min}}{\partial x_j} + \frac{\partial\xi_{\max}}{\partial x_j}\right)\int_{-1}^{+1} D'_{pt}\frac{\partial^2\overline{f'}}{\partial\overline{\xi}^2}(\overline{\xi})^{i+1} d\overline{\xi}$$
$$-\frac{1}{(\xi_{\max} - \xi_{\min})^2}\left(-\frac{\partial\xi_{\min}}{\partial x_j} + \frac{\partial\xi_{\max}}{\partial x_j}\right)^2\int_{-1}^{+1} D'_{pt}\frac{\partial^2\overline{f'}}{\partial\overline{\xi}^2}(\overline{\xi})^{i+2} d\overline{\xi}$$
$$-\frac{2}{(\xi_{\max} - \xi_{\min})^2}\left(-\frac{\partial\xi_{\min}}{\partial x_j} + \frac{\partial\xi_{\max}}{\partial x_j}\right)\left(\frac{\partial\xi_{\min}}{\partial x_j} + \frac{\partial\xi_{\max}}{\partial x_j}\right)\int_{-1}^{+1} D'_{pt}\frac{\partial\overline{f'}}{\partial\overline{\xi}}(\overline{\xi})^i d\overline{\xi}$$
$$+\frac{1}{(\xi_{\max} - \xi_{\min})}\left(\frac{\partial^2\xi_{\min}}{\partial x_j{}^2} + \frac{\partial^2\xi_{\max}}{\partial x_j{}^2}\right)\int_{-1}^{+1} D'_{pt}\frac{\partial\overline{f'}}{\partial\overline{\xi}}(\overline{\xi})^i d\overline{\xi}$$
$$-\frac{1}{(\xi_{\max} - \xi_{\min})}.\left[\left(\frac{\partial^2\xi_{\min}}{\partial x_j{}^2} - \frac{\partial^2\xi_{\max}}{\partial x_j{}^2}\right) + \frac{2}{(\xi_{\max} - \xi_{\min})}\left(-\frac{\partial\xi_{\min}}{\partial x_j} + \frac{\partial\xi_{\max}}{\partial x_j}\right)^2\right]$$
$$\times\int_{-1}^{+1} D'_{pt}\frac{\partial\overline{f'}}{\partial\overline{\xi}}(\overline{\xi})^{i+1} d\overline{\xi} \tag{4.13}$$

$$
\begin{aligned}
MB_{Diff3} = & \frac{1}{(\xi_{\max}-\xi_{\min})}\left(\frac{\partial \xi_{\min}}{\partial x_j}+\frac{\partial \xi_{\max}}{\partial x_j}\right)\int_{-1}^{+1}\frac{\partial D'_{pt}}{\partial \overline{\xi}}\frac{\partial \overline{f'}}{\partial x_j}\left(\overline{\xi}\right)^i d\overline{\xi} \\
& + \frac{1}{(\xi_{\max}-\xi_{\min})}\left(-\frac{\partial \xi_{\min}}{\partial x_j}+\frac{\partial \xi_{\max}}{\partial x_j}\right)\int_{-1}^{+1}\frac{\partial D'_{pt}}{\partial \overline{\xi}}\frac{\partial \overline{f'}}{\partial x_j}\left(\overline{\xi}\right)^{i+1} d\overline{\xi} \\
& - \frac{1}{(\xi_{\max}-\xi_{\min})^2}\left[\left(\frac{\partial \xi_{\min}}{\partial x_j}+\frac{\partial \xi_{\max}}{\partial x_j}\right)\right]^2\int_{-1}^{+1}\frac{\partial D'_{pt}}{\partial \overline{\xi}}\frac{\partial \overline{f'}}{\partial \overline{\xi}}\left(\overline{\xi}\right)^i d\overline{\xi} \\
& - \frac{1}{(\xi_{\max}-\xi_{\min})^2}.2.\left(\frac{\partial \xi_{\min}}{\partial x_j}+\frac{\partial \xi_{\max}}{\partial x_j}\right)\left(-\frac{\partial \xi_{\min}}{\partial x_j}+\frac{\partial \xi_{\max}}{\partial x_j}\right)\int_{-1}^{+1}\frac{\partial D'_{pt}}{\partial \overline{\xi}}\frac{\partial \overline{f'}}{\partial \overline{\xi}}\left(\overline{\xi}\right)^{i+1} d\overline{\xi} \\
& - \frac{1}{(\xi_{\max}-\xi_{\min})^2}\left(-\frac{\partial \xi_{\min}}{\partial x_j}+\frac{\partial \xi_{\max}}{\partial x_j}\right)^2\int_{-1}^{+1}\frac{\partial D'_{pt}}{\partial \overline{\xi}}\frac{\partial \overline{f'}}{\partial \overline{\xi}}\left(\overline{\xi}\right)^{i+2} d\overline{\xi}
\end{aligned}
\tag{4.14}
$$

and

$$
IG = \frac{2}{(\xi_{\max}-\xi_{\min})}.\left\{\left[G'_{+1}\overline{f'_{+1}}-(-1)^i.G'_{-1}\overline{f'_{-1}}\right]-i.\int_{-1}^{1}G'\overline{f'}.\left(\overline{\xi}\right)^{i-1}.d\overline{\xi}\right\} \tag{4.15}
$$

where

$$
G' = \frac{d\overline{\xi}}{dt} \tag{4.16}
$$

In the above terms, the subscripts of −1 and +1 refer to the value of that term at the minimum and maximum limits of the range [−1, +1], respectively.

In the derivation of Eq. (4.9), it has been assumed that the particulate phase is incompressible, i.e., $\frac{\partial v_{p,i}}{\partial x_j}=0$, where v_p is the particulate phase velocity. Moreover, it is assumed that the particles are convected with an average phase velocity $v_p(\mathbf{x},t)$, which means the particle velocity is independent of the internal property (e.g., size). In this case, the need for a spatial diffusion term would arise (Mazzei 2013). Mazzei (2011, 2013) has investigated the importance of diffusion when dealing with segregation dynamics of polydisperse systems and has shown that either a size-dependent velocity or a spatial diffusion term is necessary to model the segregation in polydisperse systems. He proposed a method to replace the average phase velocity $v_p(\mathbf{x},t)$ with a size-conditioned velocity field. In this case, he showed that, because the advective term features a size-dependent velocity field, the equation presents no diffusive flux in physical space. Having that in mind and for the sake of brevity, the diffusive term was omitted from the governing equation, that reduces Eqs. (4.9–4.17):

$$
\frac{\partial \mu_i}{\partial t}+v_{p,j}\frac{\partial \mu_i}{\partial x_j}=-(MB+MB_{Conv}+IG)+S \tag{4.17}
$$

S is the source term and accounts for the introduction of new particles into the system, which we assume is due only to the aggregation as defined by Eq. (4.2). To handle this term using FCMOM, it is necessary to define a finite version of the Smoluchowski equation as proposed by Strumendo and Arastoopour (2008):

$$h(\xi;\mathbf{x},t) = \frac{1}{2}H(\xi-2\xi_{\min})\int_{\xi_{\min}}^{\xi-\xi_{\min}}\beta(\xi-\eta,\eta).f\left(\xi-\eta,t\right).f(\eta,t)d\eta - f(\xi,t).H[(\xi_{\max}-\xi_{\min})-\xi].\int_{\xi_{\min}}^{\xi_{\max}-\xi}\beta(\xi,\eta).f(\eta,t)d\eta \tag{4.18}$$

In the finite version of the Smoluchowski equation, a minimum and maximum size, $\xi_{\min}$ and $\xi_{\max}$, are set, and aggregations leading to particles larger than $\xi_{\max}$ are neglected by using $\xi_{\max}-\xi$ as the upper limit of integration in the second term on the right-hand side of Eq. (4.13), by introducing the Heaviside step function H. By choosing values of $\xi_{\max}$ large enough and setting $\xi_{\min}=0$, the solution of the finite version of the Smoluchowski equation converges to the solution of its classical version (Eq. 4.2).

Therefore, the dimensionless form of the source term, S, becomes

$$S = \frac{\xi_{\max}-\xi_{\min}}{4}\sum_{n=0}^{M-1}\sum_{m=0}^{M-1}c_m c_n E_{mni} - \frac{\xi_{\max}-\xi_{\min}}{2}\sum_{n=0}^{M-1}\sum_{m=0}^{M-1}c_m c_n F_{mni} \tag{4.19}$$

E_{mni} and F_{mni} are coefficients that can be pre-calculated as a function of $\xi_{\min}$ and $\xi_{\max}$:

$$E_{mni} = \int_{-2+\xi_r}^{1}\int_{-1}^{\overline{\xi}+1-\xi_r}\overline{\xi}^i\beta\left[\frac{\xi_{\max}-\xi_{\min}}{4}.\left(\overline{\xi}-\overline{\eta}\right),\frac{\xi_{\max}-\xi_{\min}}{4}.(\overline{\eta}-v_r)\right] .\phi_m\left(\overline{\xi}-\overline{\eta}-v_r\right)\phi_n(\overline{\eta})\,d\overline{\eta}d\overline{\xi} \tag{4.20}$$

$$F_{mni} = \int_{-2+\xi_r}^{2-\xi_r}\int_{-1}^{1-\overline{\xi}-\xi_r}\overline{\xi}^i\phi_m\left(\overline{\xi}\right).\beta\left[\frac{\xi_{\max}-\xi_{\min}}{4}.\left(\overline{\xi}+\xi_r\right),\frac{\xi_{\max}-\xi_{\min}}{4}.(\overline{\eta}+\xi_r)\right] .\phi_n(\overline{\eta})\,d\overline{\eta}d\overline{\xi} \tag{4.21}$$

where

$$\xi_r = \frac{\xi_{\max}+\xi_{\min}}{\xi_{\max}-\xi_{\min}} \tag{4.22}$$

In general, moments evolution equations must be coupled with the moving boundary conditions providing the governing equations for $\xi_{\min}(t, \mathbf{x})$ and $\xi_{\max}(t,\mathbf{x})$. The moments evolution equations and the moving boundary conditions form a set of partial differential equations when the variables are the moments of the distribution function $\mu_i(t, \mathbf{x})$, and two moving boundaries, $\xi_{min}(t,\mathbf{x})$ and $\xi_{\max}(t, \mathbf{x})$. The initial conditions for the moments are computed from the initial property (e.g., size) distribution function. However, in the case of pure aggregation in which $\xi_{\min}$ and $\xi_{\max}$ are set initially to constant values, the problem is no longer a moving boundary problem, and the terms MB and MB_{Conv} will become zero. In this case, the final form of the moment transport equation is

$$\frac{\partial \mu_i}{\partial t} + \nabla.\left(\mu_i.v_p\right) = \frac{\xi_{\max} - \xi_{\min}}{4} \sum_{n=0}^{M-1} \sum_{m=0}^{M-1} c_m c_n E_{mni} - \frac{\xi_{\max} - \xi_{\min}}{2} \sum_{n=0}^{M-1} \sum_{m=0}^{M-1} c_m c_n F_{mni} \tag{4.23}$$

A detailed explanation of the FCMOM method and derivation of the governing equation can be found in two papers by Strumendo and Arastoopour (2008, 2010).

4.4 CFD-PBE Coupling for Gas–Particle Flow Systems

To develop a coupled CFD-PBE model, it is necessary to implement and solve PBE in CFD codes. Therefore, a set of transport equations based on the moments of the property distribution function may be added to any CFD code. Here, the ANSYS Fluent commercial code was selected.

ANSYS Fluent is a finite-volume-based solver that solves the differential equations for the conservation of mass and momentum and other appropriate scalars on a discretized domain using a computational grid. The solver integrates the governing equations on the individual control volumes to construct algebraic equations for the discrete-dependent variables ("unknowns") such as velocities, pressure, volume fractions, and conserved scalars. After that, it linearizes the discretized equations and solution of the resultant linear equation system to yield updated values of the dependent variables. Fluent solves this linear system using a point-implicit (Gauss–Seidel) linear equation solver in conjunction with an algebraic multigrid (AMG) method.

In ANSYS Fluent, it is possible to add and solve additional transport equations for any user-defined scalars (UDS). The equation for a generic scalar ϕ_p^k associated to the disperse-phase p is

$$\frac{\partial \varepsilon_p \rho_p \phi_i^p}{\partial t} + \nabla.\left(\varepsilon_p \rho_p v_p \phi_i^p - \varepsilon_p D_p^k \nabla \phi_i^p\right) = S_{\phi\,\mathrm{i}}^p \tag{4.24}$$

where ε_p, ρ_p, and v_p are volume fraction, physical density, and velocity of the disperse phase, respectively.

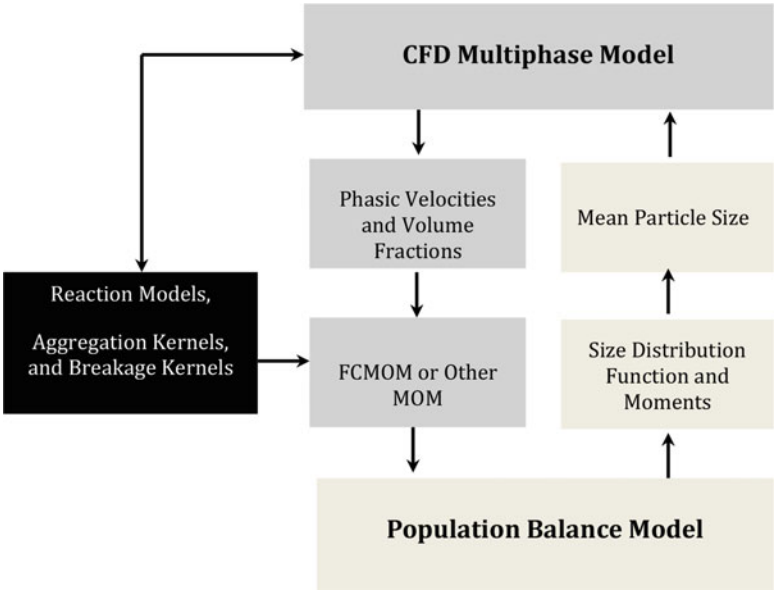

Fig. 4.1 CFD-PBE coupling algorithm (This figure was originally published in *Chemical Engineering Science* 102, 2013 and has been reused with permission)

By omitting the diffusive term and defining each scalar as

$$\phi_i^p = \mu_i \tag{4.25}$$

where μ_i is the ith moment of the size distribution function and multiplying the source by $\varepsilon_p \rho_p$, it is possible to obtain the moment transport equation (PBE) reported in Eq. (4.23) in the generic form of Eq. (4.24). The source terms for the different moment equations are calculated and returned by a proper user-defined function (UDF). Figure 4.1 describes the CFD-PBE algorithm developed by Abbasi and Arastoopour (2013). The CFD multiphase model essentially provides phasic velocities and volume fractions in every iteration. This information is passed to the UDS transport equations through a UDF to calculate the source terms based on the FCMOM method using different models for particulate processes (e.g., aggregation) or possible chemical reactions (Abbasi and Arastoopour 2013).

The population balance model block consists of a set of UDS transport equations being solved and provides the size distribution function and the moments in each computational cell for each iteration. The moments of the distribution function provide the mean particle size at each computational cell that is reported back to the CFD model to be used in calculations of interphase exchange properties (e.g., drag). The mean diameter, which is changing temporally and spatially, represents the different sizes of the particles in the disperse phase.

4.5 Verification and Validation of FCMOM

To numerically validate the proposed implementation procedure, three cases have been studied. The first case is a linear growth problem when the growth rate of the particle size is proportional to the size itself. This kind of behavior is typical in particle growth processes due to volumetric chemical reactions as studied by McMurry and Wilson (1983) and Strumendo and Arastoopour (2008). The second case is a homogeneous aggregation problem when the aggregation kernel is proportional to the summation of the sizes of the two aggregating particles.

For the first two cases, there are analytical solutions provided by McGraw (1997) and Scott (1968), respectively. Therefore, comparison of the numerical results with the analytical solutions is possible, which ensures appropriate implementation of the source terms and correct numerical integration of the differential equations.

The third case is the application of FCMOM in CFD simulations of an oil–water emulsion flow in a backward-facing step geometry including the aggregation/coalescence process as proposed by Silva et al. (2008). In this case, treatment of the convective term was studied and results were verified against the solution obtained by the QMOM method for the same case.

4.5.1 Linear Growth

McGraw (1997) has shown that a homogeneous growth problem with linear growth rate can be shown as

$$G = \frac{d\xi}{dt} = K.\xi \tag{4.26}$$

and in transformed form

$$G' = \frac{d\overline{\xi}}{dt} = K.\left[\frac{\xi_{\min} + \xi_{\max}}{2} + \frac{\xi_{\max} - \xi_{\min}}{2}.\overline{\xi}\right] \tag{4.27}$$

For any initial distribution function $\overline{f'}\left(\overline{\xi}, 0\right)$, there is an exact analytical solution given by

$$\overline{f'}\left(\overline{\xi}, t\right) = \overline{f'}\left(\overline{\xi}, 0\right).e^{-K.t} \tag{4.28}$$

Substituting Eq. (4.27) in Eq. (4.11) and combining with Eq. (4.8) gives the following set of ordinary differential moment equations that are closed regardless of the solution method (e.g., method of moments):

$$\frac{\partial \mu_i}{\partial t} = -K.\mu_i\,;\, i = 0,\ 1,\ 2\cdots \tag{4.29}$$

with an initial size distribution function in the finite domain $[\xi_{\min}(t), \xi_{\max}(t)]$,

$$f(\xi,0) = a.\left[\frac{\xi - \xi_{\min}(0)}{\xi_{\max}(0) - \xi_{\min}(0)}\right]^{q}.\left[\frac{\xi_{\max}(0) - \xi}{\xi_{\max}(0) - \xi_{\min}(0)}\right]^{p} \tag{4.30}$$

And by scaling the distribution function with respect to $\frac{a}{2^{p+q}}$, the dimensionless form of the function becomes

$$\overline{f}(\overline{\xi},0) = (1+\overline{\xi})^{q}.(1-\overline{\xi})^{p} \tag{4.31}$$

Then, a set of equations resulting from Eq. (4.29) was implemented in ANSYS Fluent in the form of Eq. (4.24). The value of K used in this simulation was $0.05\ s^{-1}$, while $q = 2$ and $p = 8$. It is essential to multiply the source term by the flow density ρ_p because of the format of the UDS equations in the solver:

$$\frac{\partial \rho_p \mu_i}{\partial t} = -\left(\rho_p K.\mu_i\right) \tag{4.32}$$

The equations were discretized using a second-order time discretization scheme with a fully implicit integration formula. The advantage of the fully implicit scheme is that it is unconditionally stable with respect to time-step size.

The simulation results are shown in Figs. 4.2 and 4.3. Figure 4.2 shows the initial dimensionless particle size distribution along with the comparison between the numerical simulation, obtained using the first eight moments ($i = 0$–7), and the exact solution at $t = 10\ s$. It shows that the numerical solution closely represents

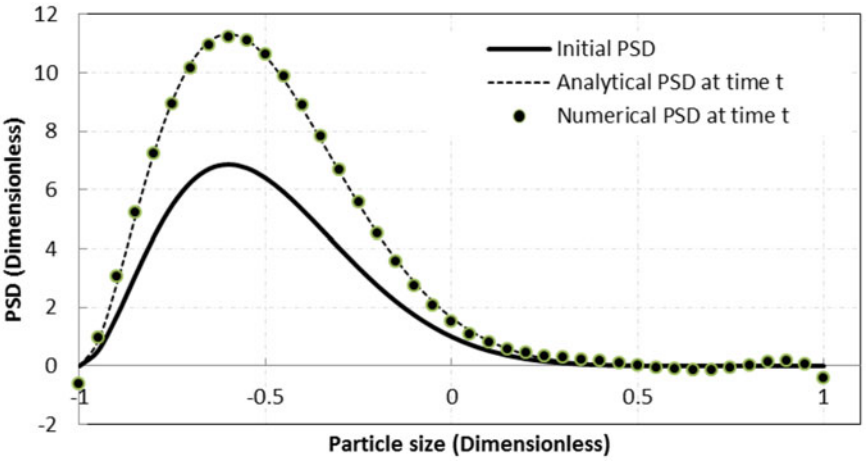

Fig. 4.2 Particle size distribution at $t = 10\ s$ computed using eight moments (This figure was originally published in *Chemical Engineering Science* 102, 2013 and has been reused with permission)

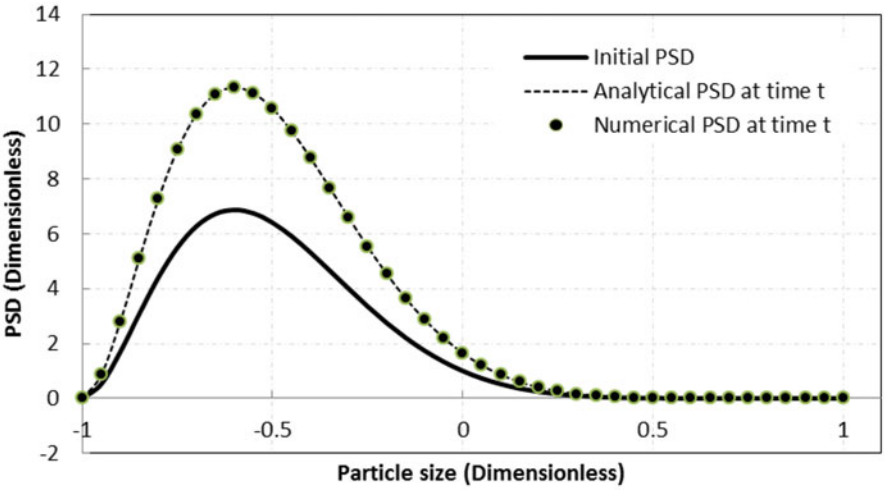

Fig. 4.3 Particle size distribution at $t = 10\ s$ computed using ten moments (This figure was originally published in *Chemical Engineering Science* 102, 2013 and has been reused with permission)

the exact solution; however, it poses some negative values in the tails of the size distribution curve that are not physically possible. Figure 4.3 indicates that the final size distribution can be accurately predicted by increasing the number of moments from 8 to 10. The same conclusion has been made by Strumendo and Arastoopour (2008) as they showed the convergence of FCMOM for various particle growth processes.

4.5.2 Homogeneous Aggregation

Convergence and accuracy of FCMOM for different homogeneous aggregations has been studied by Strumendo and Arastoopour (2008). For a homogeneous aggregation/coalescence case starting from a Gaussian-like distribution,

$$f(\xi, 0) = \frac{N_o(\upsilon+1)^{\upsilon+1}}{\xi_o \Gamma(\upsilon+1)} \left(\frac{\xi}{\xi_o}\right)^{\upsilon} e^{-\frac{\xi}{\xi_o}(\upsilon+1)} \tag{4.33}$$

where N_o and ξ_o are initial number of droplets and initial average droplet size, respectively, and the aggregation/coalescence process is governed by the sum aggregation kernel

$$\beta = \beta_o(\xi + \eta) \tag{4.34}$$

where β_o is the aggregation constant.

Scott (1968) has provided an analytical solution for Eq. (4.2) giving the dimensionless size distribution function at any time:

$$\overline{f}\left(\overline{\xi},\tau\right) = (1-\tau).e^{-\overline{\xi}(\tau+\upsilon+1)}\sum_{k=0}^{\infty}\frac{\tau^{k}\overline{\xi}^{\upsilon+k(\upsilon+2)}(\upsilon+1)^{(k+1)(\upsilon+1)}}{(k+1)!\Gamma[(k+1)(\upsilon+1)]} \tag{4.35}$$

The aggregation kernel defines the net rate of aggregation/coalescence and depends on:

1. Frequency of collisions between droplets of size ξ and droplets of size η
2. Efficiency of aggregation (i.e., the probability of a droplet of size ξ coalescing with a particle of size η)

In Eq. (4.35), $\overline{\xi}$ is dimensionless droplet size defined as ξ/ξ_o, and $\overline{f}$ is dimensionless size distribution function defined as $\frac{f(\xi,t)}{N_o/\xi_o}$. τ is related to dimensionless time, T, by,

$$\tau = 1 - e^{-T} \tag{4.36}$$

and T is defined

$$T = \beta_o N_o \xi_o t \tag{4.37}$$

For this case, an approach similar to that described in Sect. 4.5.1 was utilized to implement the governing equations [i.e., Eq. (4.18) without the convective term] for the finite Smoluchowski equation. Initial moments were calculated from Eq. (4.33), while the model parameters were adopted from Scott (1968) with $\xi_o = 4.189 \times 10^{-15} m^3$, $\upsilon = 1$, $N_o = 10^9/4.189$ $particle/m^3$, $\beta_o = 1.53 \times 10^3$ $1/s$, and $\xi_{\max}$ was set to $13\xi_o$.

Figure 4.4 shows that the simulation results obtained using 12 moments at $t = 450$ s ($\tau = 0.5$) are in excellent agreement with the analytical solution.

4.5.3 Nonhomogeneous Aggregation in Emulsion Flow

Silva et al. (2008) proposed a two-dimensional test case to evaluate the performance of the direct quadrature method of moments (DQMOM) (Marchisio and Fox 2005) implemented in CFD codes, ANSYS CFX, and OpenFoam. They defined a fictitious problem of water in oil emulsion laminar flow through a backward-facing step. The same case was adopted for this study.

Figure 4.5 shows the backward-facing step geometry and dimensions. Analysis of the results is shown on the two dashed lines shown in Fig. 4.5, referred to as horizontal and vertical lines. Water in oil emulsion (i.e., dispersed water droplets in

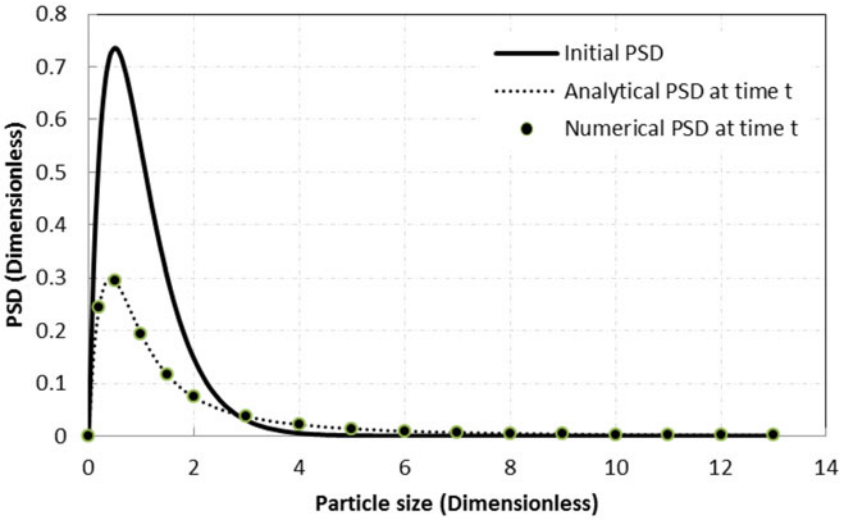

Fig. 4.4 Particle size distribution at $t = 450\ s$ computed using 12 moments (This figure was originally published in *Chemical Engineering Science* 102, 2013 and has been reused with permission)

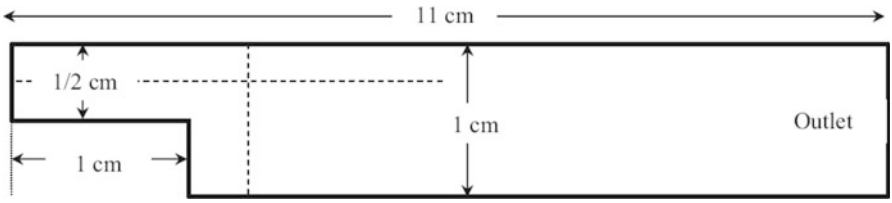

Fig. 4.5 Backward-facing step geometry (This figure was originally published in *Chemical Engineering Science* 102, 2013 and has been reused with permission)

continuous oil flow) enters the domain with a predefined initial droplet size distribution. The droplet size distribution evolves inside the domain as a result of convection and coalescence of the droplets.

Laminar flow in backward-facing step possesses unique features including presence of circulation zones with strong gradients in the laminar regime that makes it suitable for our purpose without bringing other uncertainties such as turbulence modeling into the picture. It is well known that there is a primary circulation zone behind the step in which its length (reattachment length) increases by increasing the Reynolds number. As shown in Fig. 4.6, at higher Reynolds numbers (~300), a secondary circulation zone will form at the channel upper wall due to the adverse pressure gradient coming from sudden expansion at the edge of the step (Biswas et al. 2004).

Existence of circulation zones means longer residence time of the disperse phase in those regions; therefore, a higher degree of coalescence is expected in these zones.

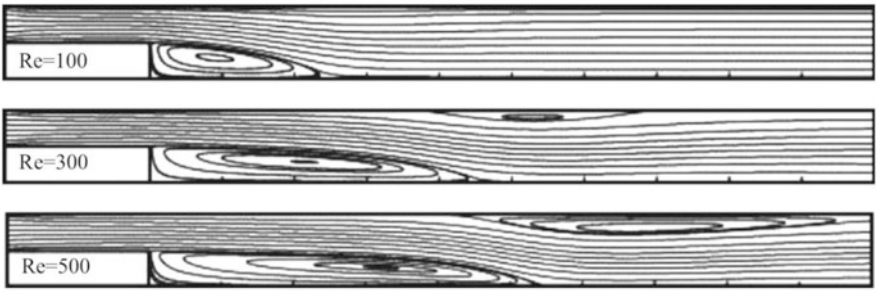

Fig. 4.6 Circulation zones in a laminar backward-facing step flow at different Reynolds number (This figure was originally published in *Chemical Engineering Science* 102, 2013 and has been reused with permission)

Table 4.1 Inlet condition and emulsion properties

Property	Value
Water density (kg/m^3)	1000
Oil density (kg/m^3)	900
Water viscosity (kg/m-s)	0.001
Oil viscosity (kg/m-s)	0.01
Reynolds number	500
Average water droplet size, d_{10} (μm)	12.5
Water content (vol %)	5
Aggregation/coalescence constant, β_o, (m^3/s)	1

Dimensionless initial size distribution of water droplets was defined by Eq. (4.33), and it is assumed that coalescence is the only process that changes the droplet size distribution according to the sum aggregation kernel (Eq. 4.34). A set of governing transport equations for the moments of the droplet size distribution was derived based on Eq. (4.23). In this equation, it is assumed that all of the droplets share the same velocity regardless of their size. Mean droplet diameter, d_{10}, was defined as the ratio of the first-order moment (μ_1) to the zeroth-order moment (μ_0).

The quadrature method of moments, QMOM (Marchisio et al. 2003a, b), which is a built-in population balance solution method in ANSYS Fluent code and FCMOM, was used to generate results using two different numerical techniques. This could consider a verification of one numerical technique versus another. Baseline simulations were performed using 4, 6, and 8 moments based on QMOM to study the sensitivity of the solution to the number of moments and to compare the results obtained by FCMOM and QMOM.

Moreover, the effect of the mesh resolution was studied using both the FCMOM and QMOM methods having 4 moments and using three different uniform hexahedral meshes, referred to as coarse, medium, and fine meshes with 8400, 33,600 and 134,400 cells, respectively. Table 4.1 shows the inlet conditions and flow properties used in the simulations.

Spatial discretization of the governing equations was performed using a first-order upwind scheme along with a first-order and implicit temporal discretization. Pressure–velocity coupling was accomplished using the Phase Coupled SIMPLE algorithm. The time step of 10^{-3} s ensures convergence within 50 iterations per time step. In addition, the higher-order spatial discretization schemes were employed for discretization of the transport equations of both QMOM (Mazzei et al. 2012) and FCMOM and both resulted in moment corruption. Moment corruption means that a certain set of moments are non-realizable; hence, they no longer represent a valid distribution function. For FCMOM, the moments are calculated in the [−1, 1] interval, which results in negative odd and positive even moments. Therefore, moment corruption was observed when moments changed their sign (i.e., an odd moment became positive or an even moment became negative) (Abbasi and Arastoopour 2013).

The same behavior was reported by many other authors. Vikas et al. (2011) and Desjardins et al. (2008) showed that realizability is guaranteed only with the first-order finite volume schemes in spite of the numerical diffusion associated with these schemes. Mazzei et al. (2012) reported that the second-order upwind scheme for a volume-density-function-based QMOM significantly affects the stability of the solution and eventually causes moment corruption. Therefore, the first-order upwind scheme was used for the method of moments techniques. Figures 4.7 and 4.8 show the mean droplet size along the vertical line for different mesh resolutions, using 4 moments in QMOM and FCMOM, respectively. Both graphs show similar

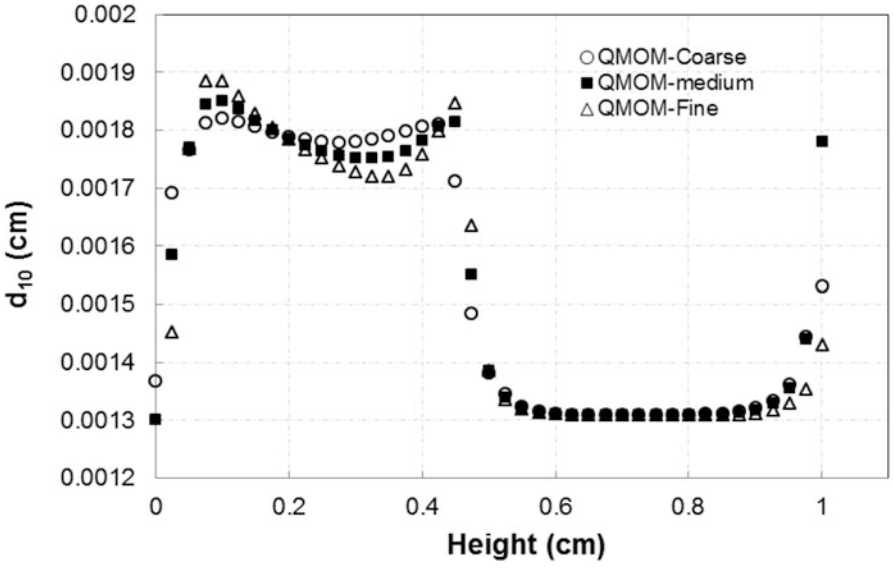

Fig. 4.7 Mean droplet size along the vertical line for different mesh resolutions with QMOM and four moments at t = 1 s (This figure was originally published in *Chemical Engineering Science* 102, 2013 and has been reused with permission)

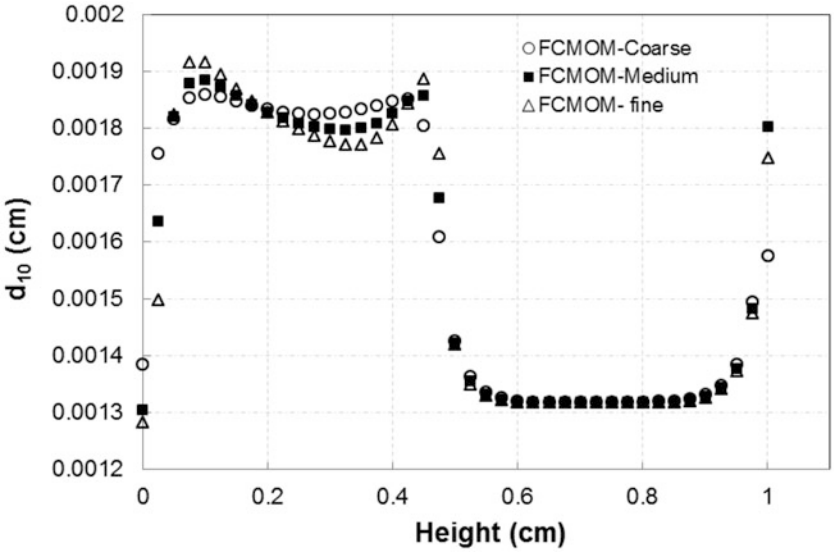

Fig. 4.8 Mean droplet size along the vertical line for different mesh resolutions with FCMOM and four moments at t = 1 s (This figure was originally published in *Chemical Engineering Science* 102, 2013 and has been reused with permission)

behaviors, having larger droplet size in the circulation region because of the longer residence time in this region; however, FCMOM appears to be slightly less sensitive to mesh resolution. Based on the grid independence study, the mesh with medium resolution was chosen for further simulations.

Figure 4.9 shows the mean droplet size along the vertical line for different number of moments calculated by QMOM. In the absence of exact solution and knowing that the error of the QMOM method decreases by increasing the number of moments, QMOM-8 was used as the basis for comparison of all results. The average error for d_{10} calculated by QMOM-4 and QMOM-6 with respect to QMOM-8 was 0.3 % and 0.03 %, respectively.

Figure 4.10 shows the mean droplet size along the vertical line calculated by FCMOM using 4 and 6 moments. Although d_{10} shows the same behavior along the vertical line, it has larger values of average error that reveal greater sensitivity of FCMOM to the number of moments compared to QMOM. The average error for d_{10} calculated by FCMOM-4 and FCMOM-6 with respect to QMOM-8 was 1 % and 0.9 %, respectively. Comparison between the calculated mean droplet sizes using FCMOM-6 and QMOM-8 along the horizontal line is shown in Fig. 4.11.

The mean droplet diameter contours calculated by FCMOM-6 at t = 1 s are presented in Fig. 4.12, which are essentially very close to those of QMOM. The disperse phase enters the domain with a 12.5 μm mean droplet diameter. The values of d_{10} continuously evolve because of the coalescence of droplets. As expected, larger droplets form in the lower and upper circulation zones mainly because of the longer residence time of the dispersed phase in those regions. Therefore, the d_{10}

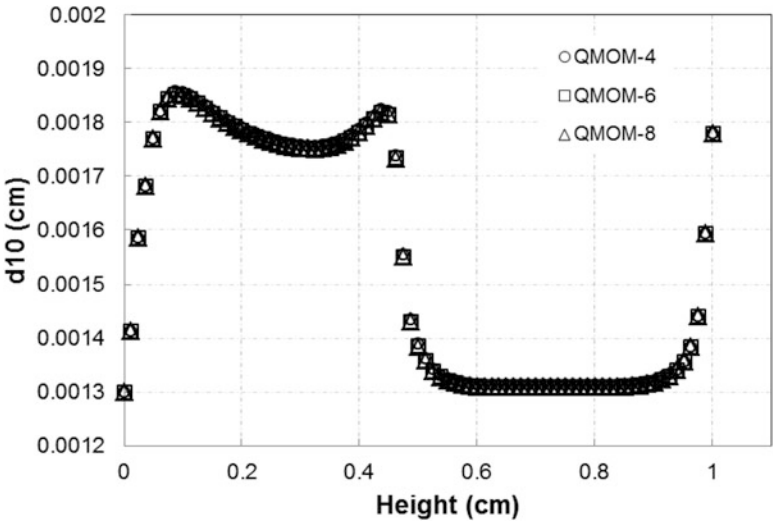

Fig. 4.9 Mean droplet size along the vertical line for different number of moments with QMOM at t = 1 s (This figure was originally published in *Chemical Engineering Science* 102, 2013 and has been reused with permission)

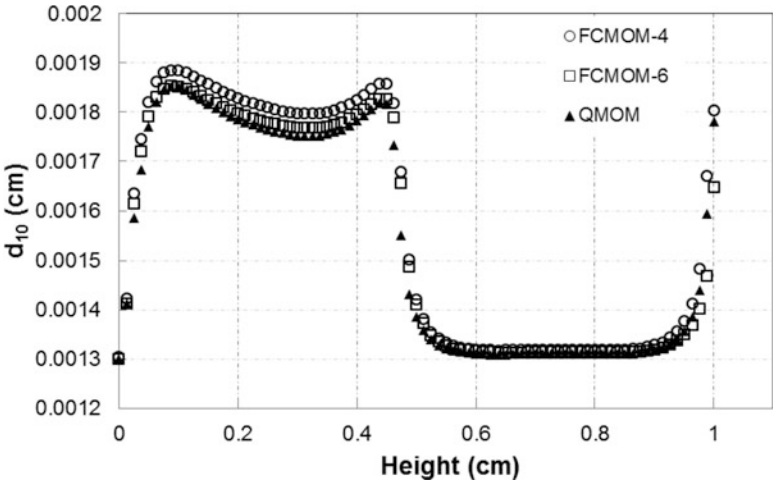

Fig. 4.10 Mean droplet size along the vertical line for different number of moments with FCMOM compared to QMOM-8 at t = 1 s (This figure was originally published in *Chemical Engineering Science* 102, 2013 and has been reused with permission)

profile directly depends on the path-line and velocity field calculated by the code. The velocity field calculations are the same for both the QMOM and FCMOM method; however, the d_{10} contours are slightly different because of the possible inaccuracy in the calculation of moments.

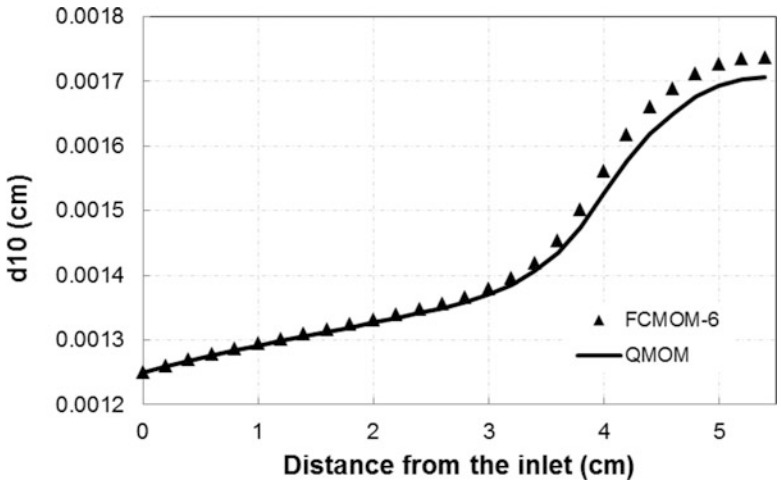

Fig. 4.11 Mean droplet size along the horizontal line for FCMOM-6 compared to QMOM-8 at t = 1 s (This figure was originally published in *Chemical Engineering Science* 102, 2013 and has been reused with permission)

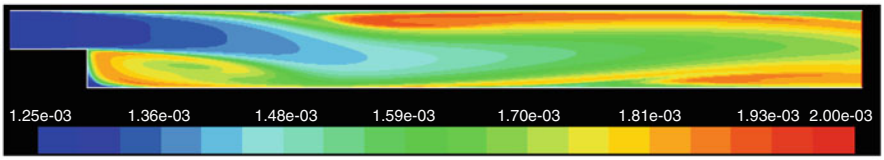

Fig. 4.12 Mean droplet diameter d_{10} contours calculated by FCMOM-6 (contour levels are in cm) at t = 1 s (This figure was originally published in *Chemical Engineering Science* 102, 2013 and has been reused with permission)

A difference between FCMOM and QMOM techniques is that FCMOM converges faster in comparison to QMOM. Figure 4.13 compares the CPU time requirement as a function of the number of grid cells for FCMOM and QMOM in an inhomogeneous aggregation problem using 4 moments. Simulations were performed using a 3.33 GHz Intel Xenon CPU on 6 parallel cores for 50 time steps with the time step size of 10^{-3} s. The comparison of the results clearly shows the better performance of FCMOM over QMOM, especially for a higher number of grid cells. For the finest grid with 134,000 grid cells, the CPU time of FCMOM is about half of that for QMOM (Abbasi and Arastoopour 2013).

Strumendo and Arastoopour (2008) have shown that increasing the number of moments increases the accuracy of FCMOM in homogeneous cases. However, Abbasi and Arastoopour (2013) were not able to reach a converged solution by increasing the number of moments to eight. In fact, tracking higher-order moments has the same effect as using a second-order discretization scheme. In other words, higher-order moments are less stable and will form non-realizable moment sets much faster than lower-order moments. In the earlier stages of the simulation, when

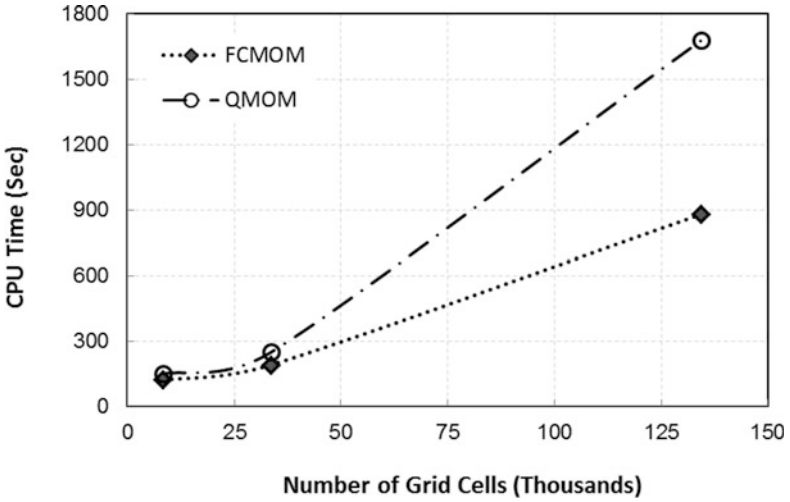

Fig. 4.13 Comparison of the CPU time as a function of the number of grid cells for QMOM and FCMOM (This figure was originally published in *Chemical Engineering Science* 102, 2013 and has been reused with permission)

the disperse phase reached the circulation zone where sharp gradients exist, moment corruption started and the error propagated into the domain that eventually leads to instabilities and divergence of the solution. To make sure that this phenomenon is not due to other factors, Abbasi and Arastoopour (2013) performed various simulations utilizing four times finer mesh, three orders of magnitude smaller time steps, and significantly smaller convergence criteria. In all cases, divergence occurred at the same flow time. Mazzei et al. (2012) also reported that quadrature nodes of the distribution become negative and corrupt the moment set when the number of moments is increased to eight or, as mentioned before, when second-order schemes were used for spatial discretization of moment transport equations, which confirms our observations. McGraw (2006), Wright (2007), and Kah et al. (2012) described this issue as an inherent problem of finite volume convective schemes as each moment is convected correctly but with independent equations. Therefore, the overall transport algorithm does not preserve the moment space and corrupts the relations among the moments.

A remedy proposed in the literature (McGraw 2006; Mazzei et al. 2012) is using moment-correction algorithms to force the moment set to always be valid (i.e., nonnegative Hankel–Hadamard determinants). The algorithm makes the least possible change to the corrupted (invalid) moments in a way that the new moment set meets the validity criteria (i.e., Hankel–Hadamard determinants become nonnegative). An alternative approach can be the use of high-order finite volume schemes similar to those proposed by Vikas et al. (2011) and Kah et al. (2012) that naturally preserve the moment space with very limited numerical diffusion. Such methods guarantee nonnegative distribution functions through an advective transport. However, before moving toward using higher-order finite-volume methods, it should be

noted again that there is an inherent problem associated with these techniques such as FCMOM which approximates the distribution function with a finite number of terms in series expansion of orthogonal functions (e.g., Legendre polynomials). In this case, even with a valid set of moments, particle size distribution (PSD) gains negative values at some points on the internal coordinate, known as the Gibbs phenomenon (Gottlieb and Shu 1997; Arias-Zugasti 2012). Therefore, it seems that the first step toward mitigation is to eliminate, or at least minimize, the effect of the Gibbs phenomenon. There is a rich history of using Gegenbauer (i.e., Legendre, Chebyshev, etc.) polynomials in other engineering fields such as image processing in addition to strategies to overcome the Gibbs phenomenon (Silver et al. 1996; Shu et al. 2010; Yap et al. 2001). For instance, the use of well-developed noise-filtering techniques such as the kernel polynomial method (KPM) (Silver et al. 1996) seems promising in our application of interest.

4.6 Summary and Conclusion

In this chapter, we discussed some of the numerical challenges that arise when dealing with polydisperse systems. Although the PBE method is considered to be one of the most efficient approaches in modeling polydispersity, finding an efficient method to solve it is not trivial. Among many solution methods for PBE, MOM stands out due to its efficiency and suitability for implementation in numerical codes.

The QMOM approach was among the first methods that were introduced to solve the closure problem in the formulation of standard MOM. Later, the method was improved through different versions of DQMOM and other enhanced versions of QMOM such as CQMOM and EQMOM. These methods were aimed to solve different shortcomings of previous methods in dealing with multivariate distribution functions, size-dependent velocity of the particulate phase, reconstruction of the distribution function, and instability of numerical solutions arising in volume averaging and spatial transport in CFD codes.

FCMOM as a computationally efficient solution method for PBE has unique advantages over other methods in its category, such as QMOM. It converges very fast to the exact solution of PBE and provides the solution in terms of both the moments of the distribution and the reconstructed distribution function. FCMOM implementation in ANSYS code and a detailed analysis of the results along with recommendations to improve its performance were provided in this chapter.

4.7 Nomenclature

C_D	Drag coefficient
c_n	Coefficients in size distribution function series expansion
D_p	Diffusivity, m^2/s

d_p Particle diameter, m
E_{mni} Coefficients in moment equations for FSE
F Function in drag model
f Number density function
$\overline{f}$ Dimensionless number density function
F_{mni} Coefficients in moment equations for FSE
G Growth rate, kg/m^3·s
h Net rate of introduction of new particles in PBE
i Moment order
K Constant in growth rate law
M Number of terms in truncated series expansion approximating particle size distribution and number of moments in simulation
N_o Initial number of particles in Gaussian-like distribution
P Legendre polynomials
Re Reynolds number
Re_p Particle Reynolds number
S Source term in PBE
T Dimensionless time
t Time, s
v_k k-phase velocity, m/s
v_p Particulate phase velocity, m/s
$\mathbf{x}$ External coordinate vector in PBE

Greek Symbols

β Aggregation kernel
β_0 Aggregation constant
β_{kj} Drag coefficient between k phase and j phase
ε_k Volume fraction of k phase
μ_i ith moment of number density function
μ_k k-phase viscosity, kg/m. s
η Second internal coordinate in Smoluchowski equation
ξ Internal coordinate in PBE
$\overline{\xi}$ Dimensionless internal coordinate in PBE
ξ_o Initial average particle size in Gaussian-like distribution, m
Γ Gamma function
ρ_k k-phase density, kg/m^3
υ Model parameter Gaussian-like distribution
τ_k k-phase stress tensor, N/m^2
τ_p Particle relaxation time, s
ϕ_n Trial function associated with Legendre polynomials

References

Abbasi E, Arastoopour H (2013) Numerical analysis and implementation of finite domain complete trial functions method of moments (FCMOM) in CFD codes. Chem Eng Sci 102:432–441

Arias-Zugasti M (2012) Adaptive orthogonal collocation for aerosol dynamics under coagulation. J Aerosol Sci 50:57–74

Barrett JC, Webb NA (1998) A comparison of some approximate methods for solving the aerosol general dynamic equation. J Aerosol Sci 29:31–39

Biswas G, Breuer M, Durst F (2004) Backward-facing step flows for various expansion ratios at low and moderate Reynolds numbers. Trans Am Soc Mech Eng J Fluids Eng 126:362–374

Desjardins O, Fox RO, Villedieu P (2008) A quadrature-based moment method for dilute fluid-particle flows. J Comput Phys 227(4):2514–2539

Diemer RB, Olson JH (2002a) A moment methodology for coagulation and breakage problems: part 1—analytical solution of the steady state population balance. Chem Eng Sci 57:2193–2209

Diemer RB, Olson JH (2002b) A moment methodology for coagulation and breakage problems: part 2—moments models and distribution reconstruction. Chem Eng Sci 57:2211–2228

Gottlieb D, Shu CW (1997) On the Gibbs phenomenon and its resolution. SIAM Rev 39 (4):644–668

Iddir H, Arastoopour H (2005) Modeling of multitype particle flow using the kinetic theory approach. AIChE J 51(6):1620–1632

Kah D, Laurent F, Massot M, Jay S (2012) A high order moment method simulating evaporation and advection of a polydisperse liquid spray. J Comput Phys 231(2):394–422

Marchisio DL, Fox RO (2005) Solution of population balance equations using the direct quadrature method of moments. J Aerosol Sci 36(1):43–73

Marchisio DL, Fox RO (2013) Computational models for polydisperse particulate and multiphase systems. Cambridge University Press, New York

Marchisio DL, Pikturna JT, Fox RO, Vigil RD (2003a) Quadrature method of moments for population-balance equations. AIChE J 49:1266

Marchisio DL, Vigil RD, Fox RO (2003b) Implementation of the quadrature method of moments in CFD codes for aggregation–breakage problems. Chem Eng Sci 58:3337–3351

Mazzei L (2011) Limitations of quadrature-based moment methods for modeling inhomogeneous polydisperse fluidized powders. Chem Eng Sci 66(16):3628–3640

Mazzei L, Marchisio DL, Lettieri P (2012) New quadrature-based moment method for the mixing of inert polydisperse fluidized powders in commercial CFD codes. AIChE J 58(10):3054–3069

Mazzei L (2013) Segregation dynamics of dense polydisperse fluidized suspensions modeled using a novel formulation of the direct quadrature method of moments. Chem Eng Sci 101:565–576

McGraw R (1997) Description of aerosol dynamics by the quadrature method of moments. Aerosol Sci Tech 27:255–265

McGraw R (2006) Correcting moment sequences for errors associated with advective transport. http://www.ecd.bnl.gov/pubs/momentcorrection_mcgraw2006.pdf

McMurry PH, Wilson JC (1983) Droplet phase (heterogeneous) and gas phase (homogeneous) contributions to secondary ambient aerosol formation as functions of relative humidity. J Geophys Res 88:5101–5108

Ramkrishna D (2000) Population balances: theory and applications to particulate systems in engineering. Academic, London

Scott WT (1968) Analytic studies of cloud droplet coalescence I. J Atmos Sci 25:54–65

Shu H, Zhang H, Chen B, Haigron P, Luo L (2010) Fast computation of Tchebichef moments for binary and grayscale images. IEEE Trans Image Process 19(12):3171–3180

Silva LFLR, Damian RB, Lage PLC (2008) Implementation and analysis of numerical solution of the population balance equation in CFD packages. Comput Chem Eng 32(12):2933–2945

Silver RN, Roeder H, Voter AF, Kress JD (1996) Chebyshev moment problems: maximum entropy and kernel polynomial methods. In: Maximum entropy and Bayesian methods. Springer, Dordrecht, pp 187–194

Smoluchowski MZ (1917) Versuch einer mathematischen theorie der koagulationskinetik kolloider losungen. Z Phys Chem Z Physik 92:129–168

Strumendo M, Arastoopour H (2010) Solution of population balance equations by the FCMOM for in-homogeneous systems. Ind Eng Chem Res 49(11):5222–5230

Strumendo M, Arastoopour H (2008) Solution of PBE by MOM in finite size domains. Chem Eng Sci 63(10):2624.2640

Vanni M (2000) Approximate population balance equations for aggregation-breakage processes. J Colloid Interface Sci 221(2):143–160

Vikas V, Wang ZJ, Passalacqua A, Fox RO (2011) Realizable high-order finite-volume schemes for quadrature-based moment methods. J Comput Phys 230(13):5328–5352

Wright DL (2007) Numerical advection of moments of the particle size distribution in Eulerian models. J Aerosol Sci 38:352

Yap PT, Raveendran P, Ong SH (2001) Chebyshev moments as a new set of moments for image reconstruction. In: Proceeding of the international joint conference on neural networks, IJCNN'01, 2856–2860

Yuan C, Fox RO (2011) Conditional quadrature method of moments for kinetic equations. J Comput Phys 230(22):8216–8246

Yuan C (2013) Quadrature-based moment methods for polydisperse multiphase flow modeling. Doctoral dissertation, Iowa State University

Yuan C, Laurent F, Fox RO (2012) An extended quadrature method of moments for population balance equations. J Aerosol Sci 51:1–23

Chapter 5
Case Studies

5.1 CFD Simulation of a Pharmaceutical Bubbling Bed Drying Process

Drying is one of the major unit operations in the manufacturing of solid pharmaceuticals. In many pharmaceutical processes, the optimum design of the drying process will significantly enhance the rate and reliability of the production and, in turn, decrease the cost of the pharmaceutical products. Consider a cone-shaped batch fluidized bed drying process with bottom (inlet) and top (outlet) diameters of 0.08 m and 0.19 m, respectively. Pharmaceutical granulated spherical particles with 1200 kg/m^3 density, 287 μm diameter, and 0.0417 kg water/kg dried solid initial moisture content were placed initially in the bed. To remove water from the particles, a stream of high temperature air with 5 m^3/h flow rate and 50 °C temperature was introduced. The fluidized bed is operating in a bubbling regime. The critical moisture content (X_{cr}) that separates the two drying rate periods (namely, the constant rate period and the falling rate period) was estimated to be 0.012 kg water/kg dry solid.

5.1.1 Problem

Develop continuity, momentum, energy, and water species equations and boundary conditions capable of describing this process and calculate the outlet air temperature and moisture content of the particles as a function of time for 10 min of the drying process.

H. Arastoopour et al., *Computational Transport Phenomena of Fluid-Particle Systems*,
Mechanical Engineering Series, DOI 10.1007/978-3-319-45490-0_5

5.1.2 Solution

In addition to the conservation equations (i.e., mass, momentum, and species) and the constitutive equations presented in Tables 2.1 and 2.2, the following conservation of energy equations for both phases were also solved. It is assumed that the particulate phase is homogeneous and the Syamlal et al. (1993) drag model was used as the drag force between phases (Jang and Arastoopour 2014).

5.1.3 Conservation of Energy

The conservation of energy equation for each phase can be written as

$$\frac{\partial\left(\varepsilon_g\rho_g h_g\right)}{\partial t}+\nabla\cdot\left(\varepsilon_g\rho_g\vec{v}_g h_g\right)=-\varepsilon_g\frac{\partial p_g}{\partial t}+\bar{\bar{\tau}}_g : \nabla\vec{v}_g-\nabla\cdot\vec{q}_g+Q_{sg}+\dot{m}_{sg}\Delta H_{vap} \tag{5.1}$$

$$\frac{\partial\left(\varepsilon_s\rho_s h_s\right)}{\partial t}+\nabla\cdot\left(\varepsilon_s\rho_s\vec{v}_s h_s\right)=-\varepsilon_s\frac{\partial p_s}{\partial t}+\bar{\bar{\tau}}_s : \nabla\vec{v}_s-\nabla\cdot\vec{q}_s+Q_{gs}-\dot{m}_{sg}\Delta H_{vap} \tag{5.2}$$

where h is the specific enthalpy, $\vec{q}$ is the heat flux, and Q_{sg} is the rate of heat transfer between the gas and solid phases. The specific enthalpy (h) and the heat flux ($\vec{q}$) in each phase are expressed as

$$h=\int C_p dT \quad \text{and} \quad \vec{q}=k\nabla T \tag{5.3}$$

where k is the thermal conductivity and C_p is the heat capacity

$$Q_{sg}=-Q_{gs}=\frac{6\varepsilon_s}{d_s}\alpha_{sg}\left(T_g-T_s\right) \tag{5.4}$$

The gas–particle heat transfer coefficient α_{gs} was obtained from the Khotari (1967) expression:

$$Nu=\frac{\alpha_{gs}d_p}{k_g}=0.03\mathrm{Re}_p{}^{1/3} \tag{5.5}$$

where Nu is the Nusselt number, d_p is particle diameter, and k_g is thermal conductivity of the gas phase.

The latent heat due to vaporization of moisture is expressed as (Palancz 1983)

$$\Delta H_{vap} = 3168 - 2.4364 \cdot T_g \tag{5.6}$$

The above equation assumes no effect of the solid moisture on the heat of vaporization.

5.1.4 Species Balance Equation for Water

In order to simulate moisture transfer from the solid phase to the gas phase, the following water species transport equations for each phase are considered:

$$\frac{\partial\left(\varepsilon_g \rho_g Y_v\right)}{\partial t} + \nabla \cdot \left(\varepsilon_g \rho_g \vec{v}_g Y_v\right) = \nabla \cdot \left(D_{v,g} \rho_v \varepsilon_g \nabla Y_v\right) + \dot{m} \tag{5.7}$$

$$\frac{\partial(\varepsilon_s \rho_s X_s)}{\partial t} + \nabla \cdot (\varepsilon_s \rho_s \vec{v}_s X_s) = \nabla \cdot (D_{v,s} \rho_s \varepsilon_s \nabla X_s) - \dot{m} \tag{5.8}$$

where Y_v is the moisture content of the gas phase, X_s is the moisture content of the solid phase, $D_{v,g}$ *and* $D_{v,s}$ are the moisture diffusion coefficient in the gas and the solid phases, respectively, and $\dot{m}$ is the moisture mass transfer rate between the gas and the solid phase.

5.1.5 Drying Rate Model (Calculation of $\dot{m}$)

The drying rate is controlled by two mechanisms: the constant drying rate period and the falling rate period. The surface moisture on the particle and the water in the large pores of the particle predominantly influence the constant drying rate period. The moisture trapped or bound within the porous structure of the particles controls the falling rate period.

The expression for the mass transfer rate per unit volume for the constant rate period can be expressed as

$$\dot{m} = K_{sg} . \rho_g \cdot 6/d_p \cdot \left(Y_i^* - Y_v\right) \tag{5.9}$$

where Y_i^* is the moisture content of the saturated drying gas at the surface of the wet particles and Y_v is the moisture content of the gas phase. The mass transfer coefficient K_{sg} can be expressed by the Gunn (1978) equation

$$Sch = \frac{K_{sg} d_s}{Dv_g} = \left(7 - 10\varepsilon_g + 5\varepsilon_g^2\right)\left(1 + 0.7\mathrm{Re}_s^{0.2} Sc^{1/3}\right) + \left(1.33 - 2.4\varepsilon_g + 1.2\varepsilon_g^2\right)\mathrm{Re}_s^{0.7} Sc^{1/3} \tag{5.10}$$

$$Sc = \frac{\mu_g}{\rho_g Dv_g} \quad \text{and} \quad Dv_g = 2.60 \cdot 10^{-5} \cdot \left(\frac{T_s}{T_{ref}}\right)^{3/2} \tag{5.11}$$

$$Y_i^* = 0.622 \frac{p_v}{760 - p_v} \text{ and } p_v = 133.3 \times \exp\left(13.869 - \frac{5173}{T_s}\right) \tag{5.12}$$

where Sch is the Sherwood number, Sc is the Schmidt number, and A_s is the overall external particle surface area to unit volume ratio.

When the moisture content of the solid particles (X_i) reaches a critical value of (X_{cr}), the falling rate period begins. This means that the moisture transfer of the gas and the solid phase at the external surface is significantly decreased so that the diffusion process controls the rate of drying.

The mass transfer rate per unit volume for the falling rate period can be expressed by

$$\dot{m} = \frac{Dv_s \cdot \pi^2}{d_p^2} \cdot \rho_s \cdot \left(X_s - X_f\right) \tag{5.13}$$

Dv_s is assumed to have a typical value of 2×10^{-12} m^2/s. Xs is the volume-averaged moisture content of the particles, and X_f is the final volume-averaged moisture content or volume-averaged equilibrium moisture content of the particles.

For more details regarding governing and constitutive equations, see Jang and Arastoopour (2014).

5.1.6 Boundary Conditions

Initially, the gas velocity was set at zero throughout the entire bed. A uniform velocity profile for the gas phase was applied as an inlet condition. A value for the pressure was specified at the outlet of the fluidized bed. For the gas phase, no-slip and non-penetrating wall conditions were considered. For the solid phase, the slip (Johnson and Jackson 1987) according to Table 2.2,

$$\overline{\tau}_s = -\frac{\pi}{6}\sqrt{3\phi}\frac{\varepsilon_s}{\varepsilon_{s,\max}}\rho_s\, g_0 \sqrt{\theta_s}\, \vec{v}_{s,\mathrm{para}} \tag{5.14}$$

where $\vec{v}_{s,para}$ is the particle slip velocity parallel to the wall and θ is the granular temperature. θ is the specularity coefficient between the particle and the wall, which is defined as the average fraction of relative tangential momentum transferred between the particle and the wall collision. A value for a specularity coefficient

of 0.2 was assumed. The Johnson and Jackson (1987) wall boundary condition for granular temperature was also considered:

$$q_s = \frac{\pi}{6}\sqrt{3\phi}\frac{\varepsilon_s}{\varepsilon_{s,\max}}\rho_s\, g_0\sqrt{\theta_s}\,\vec{v}_{s,\text{para}}\cdot\vec{v}_{s,\text{para}} - \frac{\pi}{4}\sqrt{3}\frac{\varepsilon_s}{\varepsilon_{s,\max}}\left(1-e_{sw}^2\right)\rho_s\, g_0\,\theta_s^{3/2} \tag{5.15}$$

A value of restitution coefficient e_{sw} of 0.2 between the particle and the wall and a value of restitution coefficient e_{ss} of 0.9 between particles were assumed (see Jang and Arastoopour 2014 for a more detailed explanation).

5.1.7 Numerical Solution

The control-volume-based code FLUENT was used to carry out the two-dimensional (2D) computational simulations in this study. The governing equations were then spatially discretized using a second-order upwind scheme. To avoid solution divergence, small time steps on the order of $1 \times 10–4$ were chosen, except for energy and species balance for which convergence was set to occur when the residuals fell below $1 \times 10–6$. To obtain numerical solutions independent of the grid size, 2550 grids were used. Figure 5.1 shows the calculated air temperature exiting from the fluidized bed dryer as a function of time.

Figure 5.2 shows the average water content in the particles in the bed as a function of time. This figure clearly shows that, during the constant rate period, the moisture content is almost linearly decreasing at a higher rate toward the critical moisture content (0.012 kgw/kgs or water content of 1.2 %). After the moisture content of the particles in the bed reached the critical moisture content level, the remaining moisture inside the particles was removed by the diffusion process (falling rate period) at a lower rate. About 70 % of the initial moisture was on the surface of the particles and in large surface pores (removed during the constant drying rate period). The remaining 20 % of the moisture was in the porous structure of the particles (mainly removed during the falling drying rate period). The rest of the 10 % moisture remained as the equilibrium moisture content.

5.2 CFD Simulation of a CO_2 Capture Process in a CFB Reactor

Carbon capture from combustion and utilization of carbon-based fuel, such as fossil fuel, plays a critical role in solving the urgent climate change problem created by CO_2 emission (Extavour and Bunje 2016). In addition, circulating fluidized bed (CFB) reactors have the potential to be among the most important devices in the

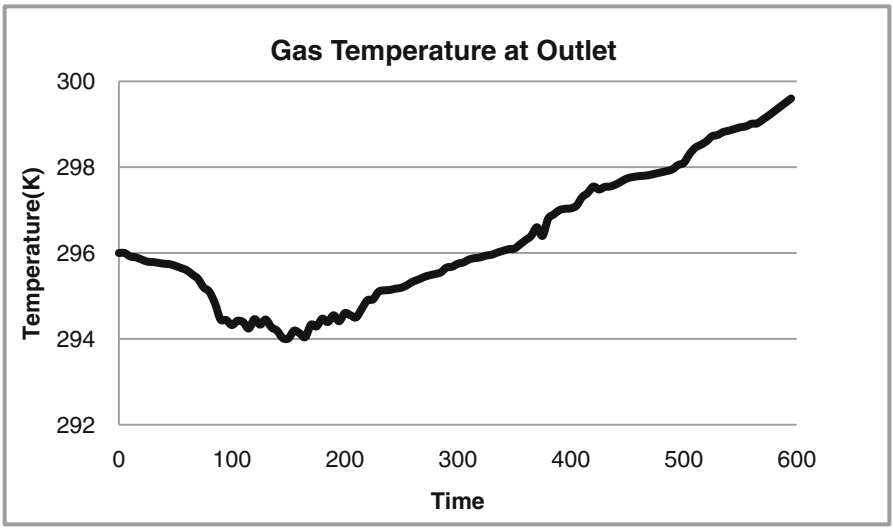

Fig. 5.1 Air temperature exiting from the fluidized bed dryer as a function of time (This figure was originally published in *Powder Techol* 263, 2014 and has been reused with permission)

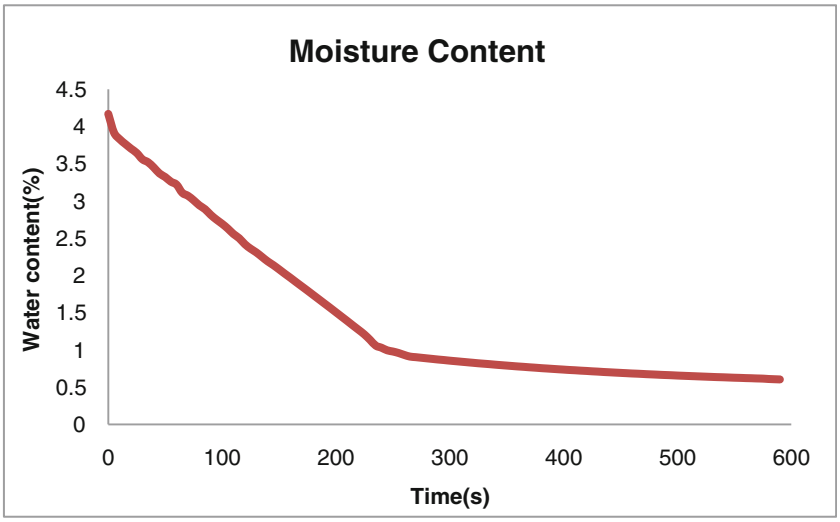

Fig. 5.2 The average water content in the particles in the bed as a function of time (This figure was originally published in *Powder Technol* 263, 2014 and has been reused with permission)

chemical and energy industries. CFB reactors currently are used in fluid catalytic cracking (FCC) applications, with more than seven decades of history and more than 400 units in operation worldwide today (Chen 2011). Furthermore, gasification of coal and biomass, synthesis of olefin from methanol, and chemical looping are

among the relatively new applications of CFB reactors (Sundaresan 2011). Thus, the CFB reactor ensures a continuous carbon dioxide removal process in a relatively compact unit using solid particles. The basic configuration of a CFB reactor consists of a riser where the particles are transported by the gas flow, a cyclone to separate gas and solid at the top of the riser, a standpipe (downcomer) to return the separated solid to the riser inlet, and a flow controlling device (e.g., L-valve) to control the solid flow. In processes that include a regenerable sorbent or catalyst, a second fluidized bed reactor can be added between the downcomer and the L-valve to serve as a regenerator reactor.

5.2.1 Problem

Consider a bench-scale CO_2 capture unit using a solid sorbent to separate CO_2 from a gas stream as shown in Fig. 5.3.

Coal gas enters the bottom of the adsorber and mixes with fresh sorbent. Particles have 185 μm mean diameter and 2480 kg/m^3 density. The sorbent particles mix with the coal gases adsorbing CO_2 into the particle through chemical reaction. The CO_2-laden particles flow up the riser, turn, and flow into the cyclone. CO_2-free gas is separated from particles in the cyclone and exit the system, and the CO_2-laden particles pass through a loop seal and enter the regenerator where CO_2 is released from the sorbent particles by heating up the spent sorbent. The CO_2-lean gas exits the carbon capture unit (C2U) system, and the regenerated sorbent particles continue through the loop to the next loop seal (Shadle et al. 2010). The fresh sorbent particles pass through the loop seal to the adsorber, and the process continues. To maintain gas–particle flow in a CO_2 capture loop, gases need to be injected around the system to keep particles fluidized.

Develop governing equations (continuity, species, and momentum) and numerical simulation, and obtain the outlet CO_2 concentration for the carbonation process in the adsorber and riser sections. In this example, the focus is on the simulation of the reactive gas–solid flow in the adsorber and riser sections. The riser and adsorber have a 3.35 m combined height and 5 cm and 15 cm diameter, respectively.

5.2.2 Solution

The conservation equations (i.e., mass, momentum, and species) and constitutive equation presented in Tables 2.1 and 2.2, for both phases, were solved on a three-dimensional (3D) Cartesian domain. It is assumed that the process is isothermal and particle size is constant and uniform. The Syamlal et al. (1993) drag model was used as the drag force between phases (Abbasi et al. 2015). The Syamlal-O'Brien drag expression contains adjustable parameters that can be used to tune the drag to match the theoretical minimum fluidization velocity to experimentally observed values. It

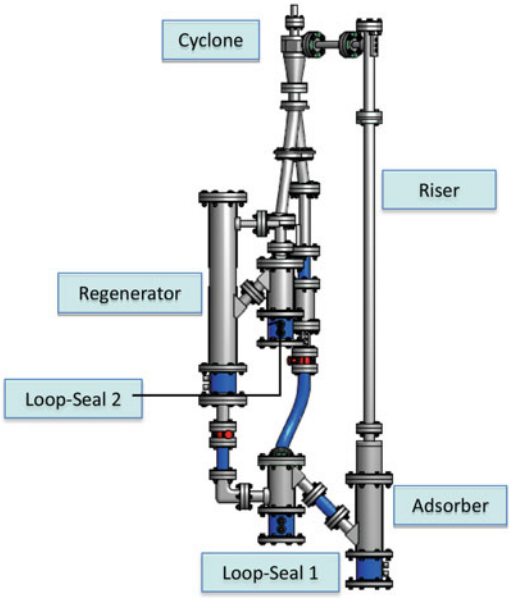

Fig. 5.3 NETL carbon capture unit (C2U) experimental setup (Source: Shadle et al. 2010)

Table 5.1 Summary of simulation cases

Case	Inlet gas velocity (m/s)	Solid circulation rate (g/s)
Baseline	0.15	44
Case 1	0.15	220
Case 2	0.15	440
Case 3	0.1125	220
Case 4	0.0975	220

should be noted that the original drag correlation was derived for homogeneous gas–solid flows and the adjustment reduces the drag to partially account for the heterogeneous gas–solid structure in the fluidized bed.

A summary of all of the simulations performed at different solid circulation rates and gas inlet velocities is presented in Table 5.1. These variables were varied within a range that ensures the fast fluidization regime in the riser. To study the effect of the solid circulation rate, the inlet solid mass flow rate was increased by factors of 5 and 10, while the inlet gas velocity was kept constant at the baseline value. Furthermore, at the inlet solid mass flow rate of 220 g/s (Case 1), the inlet gas velocity was decreased by 25 % and 35 % (Case 3 and Case 4, respectively) to investigate the effect of gas residence time on CO_2 removal. In these simulations, a 50/50 (mole fraction) mixture of CO_2 and N_2 was used as the inlet gas.

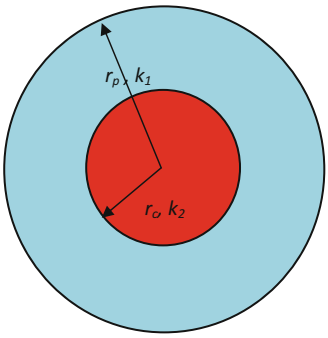

Fig. 5.4 Schematic of the reacting particle (This figure was originally published in *Powder Technol* 286, 2015 and has been reused with permission)

5.2.3 Reaction Kinetic Model

To describe the heterogeneous reaction between the sorbent and CO_2, it was assumed that the particles can be described (see Fig. 5.4) by two distinct zones representing the outer product layer and the inner core (fresh sorbent).

The heterogeneous kinetic model for the reaction between CO_2 and the sorbent based on a two-zone variable diffusivity shrinking core model is described by Abbasi et al. (2013) as

$$\frac{dX}{dt} = -\frac{\frac{3}{r_p}\frac{k_s}{N^o_{MgO}}(C_b - C_e)(1-X)^{\frac{2}{3}}}{1+\frac{k_s}{D_g}r_p(1-X)^{\frac{1}{3}}\left(1-\sqrt[3]{\frac{1-X}{1-X+XZ}}\right)} \quad \text{where} \quad k_s = \begin{vmatrix} k_1 & for\ r_i \geq r_c \\ k_2 & for\ r_i < r_c \end{vmatrix} \tag{5.16}$$

C_b is the CO_2 concentration in the bulk gas, C_e is the equilibrium CO_2 concentration, D_g is the product layer diffusivity of CO_2, r_p is the radius of the particle, k_s is the surface reaction constant rate at each zone, and $N^o{}_{\mathrm{MgO}}$ is the initial number of moles of MgO per unit volume. In the above model, the dependence of the gas diffusion coefficient D_g, through the porous product layer with respect to conversion, was assumed to follow an exponential decay function (Abbasi et al. 2013). The rate of the carbonation reaction can be calculated from the rate of the sorbent conversion obtained from the two-zone variable diffusivity shrinking core model which gives the dX/dt in the following correlation:

$$\dot{R} = \frac{y_{MgO}}{MW_{sorbent}}\frac{dX}{dt} \tag{5.17}$$

5.2.4 Numerical Solution

The operating and inlet conditions were set using the values presented in Table 5.1 and the pressure boundary condition was used at the outlet. Furthermore, at the wall, a no-slip condition for the gas phase and a partial slip condition for the solid phase, based on Johnson and Jackson (1987), with a specularity coefficient of 0.2, were used (see Table 2.2). The restitution coefficient of particle–particle was set to 0.9. The 3D computational domain consists of approximately 87,000 cells.

Figure 5.5 shows the contours of the instantaneous solid volume fraction, CO_2 mole fraction, and reaction rate at $t = 20$ s for a solid circulation rate of 220 g/s. The solid volume fraction contours show a very dense and well-mixed solid phase in the carbonator and a dilute region in the riser. Reaction rate contours also show that most of the CO_2 capture takes place in the carbonator with very little reaction in the riser.

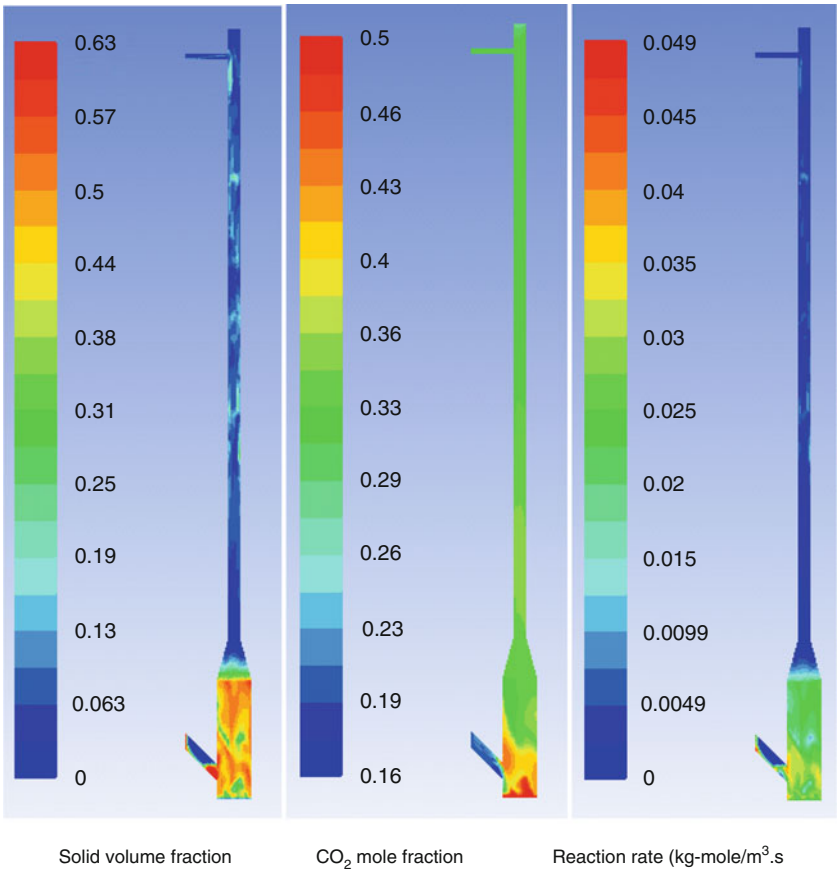

Fig. 5.5 Contours of instantaneous solid volume fraction, CO_2 mole fraction, and reaction rate at $t = 20$ s, for solid circulation rate of 220 g/s (This figure was originally published in *Powder Technol* 286, 2015 and has been reused with permission)

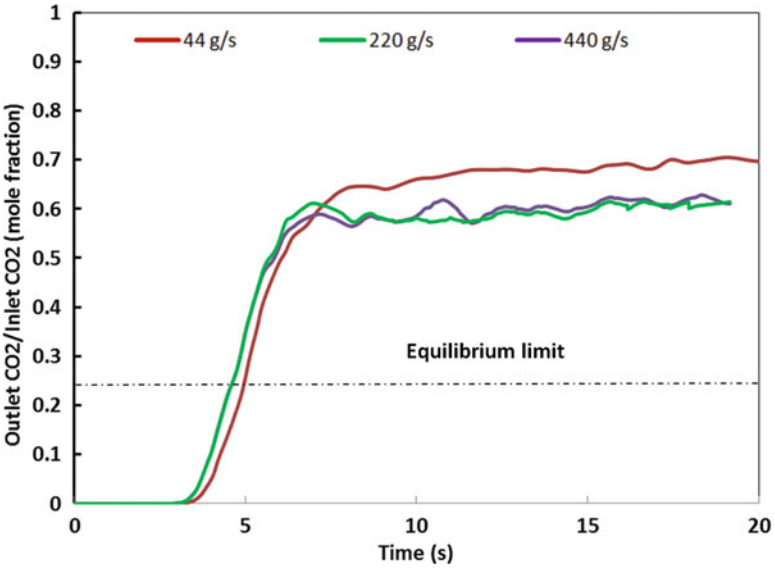

Fig. 5.6 Effect of solid circulation rate on CO_2 removal (This figure was originally published in *Powder Technol* 286, 2015 and has been reused with permission)

The effect of the solids circulation rate on the removal of CO_2 from the 50/50 (mole fraction) mixture of CO_2 and N_2 is presented in Fig. 5.6. It can be seen that, as the solid mass flow rate is increased, the CO_2 exit mole fraction decreases. At the baseline condition (44 g/s), a 30 % CO_2 removal was achieved. At a 5 times higher solid mass flow rate (Case 1), the removal increased to 40 % and, after that, even with a 10 times higher solid mass flow rate (Case 2), no increase in CO_2 removal was observed. Since there is no difference in CO_2 removal by further increasing the solid inlet mass flow rate, it suggests that the process is controlled by the reaction rate and an improvement is expected by decreasing the gas residence time.

The effect of gas residence time was studied by changing the inlet gas velocity and keeping the solid circulation rate constant at 220 g/s. Three cases with inlet gas velocities of baseline (0.15 m/s), and 25 % and 35 % lower gas velocities (0.1125 m/s and 0.0975 m/s) were investigated. As expected and is shown in Fig. 5.7, CO_2 removal increases with increasing gas residence time, providing the gas and solid a longer contact time and a more efficient process. Decreasing the inlet gas velocity by 35 % leads to an additional 20 % CO_2 removal, reaching to 60 % CO_2 removal. The improving effect of longer gas residence time is evident by comparing the concentrations of CO_2 at the exit, which decreases by reducing the inlet gas velocity and higher gas residence time in the reactor. However, even at the lowest inlet gas velocity (0.0975 m/s), the outlet CO_2 concentration is far from the equilibrium limit that is the lowest achievable concentration at this operating condition. Further decreasing the inlet gas velocity is not possible due to the change in the behavior

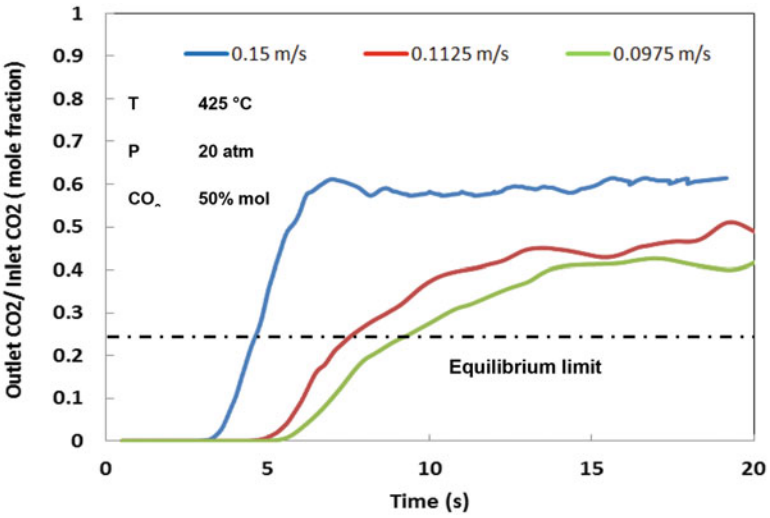

Fig. 5.7 Effect of inlet gas velocity on CO_2 removal (This figure was originally published in *Powder Technol* 286, 2015 and has been reused with permission)

of the fluidized bed, not being at a turbulent/fast fluidization regime. The CFD model can be used to find the optimum reactor design, specifically the geometry of the carbonator, to maximize the gas–solid contact and, hence, CO_2 removal.

5.3 CFD-PBE Simulation of a CO_2 Capture Process Using Solid Sorbents

Experimental data in the literature (Yi et al. 2007) on fresh, carbonated, and regenerated sorbent particles in the CO_2 capture process using solid sorbents have shown that the sorbent particle size distribution essentially remains constant during the carbonation and regeneration processes. However, the mass of the sorbent particle changes during both the sorption (mass gain) and regeneration processes (mass loss), which leads to the changes in the density of the particles. Consequently, the particles go through a structural change (e.g., change in porosity distribution).

5.3.1 Problem

Consider the example provided in Case 2, and assume that the solid sorbent entering the reactor has a unimodal density distribution representing a partially regenerated sorbent as shown in Fig. 5.8 in dimensionless form. The probability density function spans between a minimum density (i.e., 2480 kg/m^3) corresponding to

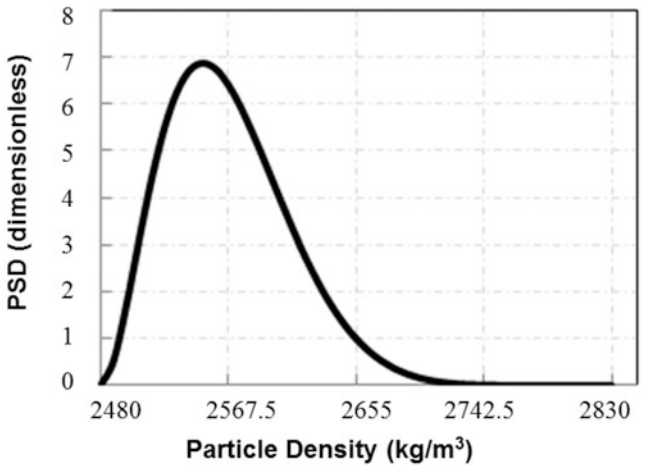

Fig. 5.8 Particle density distribution function at the inlet (This figure was originally published in *Powder Technol* 286, 2015 and has been reused with permission)

the fresh sorbent and a maximum density (i.e., 2830 kg/m^3) corresponding to the fully reacted sorbent. The mean density value at the solid inlet is 2569 kg/m^3. Develop a CFD-based model and numerical solution to calculate the variation in particle density during this carbonation process.

5.3.2 Solution

In this section, the CFD model of Case 2 is coupled with a FCMOM-based population balance equation (PBE) through the two-way coupling algorithm presented in Chap. 4 to account for the temporal and spatial evolution of the sorbent density distribution inside the reactor. In formulation of the PBE, for an inhomogeneous and univariate particulate system, with the particle density being the only internal coordinate, Eq. (4.1) becomes

$$\frac{\partial f(\boldsymbol{\xi};\mathbf{x},t)}{\partial t}+\frac{\partial}{\partial x_i}\left[v_p(\mathbf{x},t)f(\boldsymbol{\xi};\mathbf{x},t)\right]+\frac{\partial}{\partial \xi_j}\left[\frac{\partial \xi_j}{\partial t}f(\boldsymbol{\xi};\mathbf{x},t)\right]=h(\boldsymbol{\xi};\mathbf{x},t) \tag{5.18}$$

In the above equation, it is assumed that the system is nondiffusive (i.e., no diffusion term).

Since, in the FCMOM approach, the solution of the PBE is sought in the finite interval between the minimum and maximum values [ξ_{min}, ξ_{max}] of the particle density, ξ_{min} and ξ_{max} can be considered as the density of the fresh sorbent and the density of the sorbent with complete conversion, respectively.

The final form of the moments transport equations (Eq. 4.9) for this specific case becomes

$$\begin{aligned}
&\frac{\partial \mu_i}{\partial t} + \frac{\partial}{\partial x_j}\left[v_{p,j}\mu_i\right] = -\frac{2}{(\xi_{\max}-\xi_{\min})}.\left\{\left[G'_{+1}\overline{f'_{+1}} - (-1)^i.G'_{-1}\overline{f'_{-1}}\right] - i.\int_{-1}^{1} G'\overline{f'}.(\overline{\xi})^{i-1}.d\overline{\xi}\right\} \\
&\left\{\left[\overline{f'_{+1}} - (-1)^i.\overline{f'_{-1}}\right] - i.\mu_{i-1}\right\}.\frac{1}{(\xi_{\max}-\xi_{\min})}.\left(\frac{d\xi_{\min}}{dt}\right) \\
&\left\{\left[\overline{f'_{+1}} - (-1)^{i+1}.\overline{f'_{-1}}\right] - (i+1).\mu_i\right\}.\frac{1}{(\xi_{\max}-\xi_{\min})}.\left(-\frac{d\xi_{\min}}{dt}\right) \\
&\left\{\left[\overline{f'_{+1}} - (-1)^i.\overline{f'_{-1}}\right] - i.\mu_{i-1}\right\}.\frac{v_{p,j}}{(\xi_{\max}-\xi_{\min})}.\left(\frac{\partial \xi_{\min}}{\partial x_j}\right) \\
&\left\{\left[\overline{f'_{+1}} - (-1)^{i+1}.\overline{f'_{-1}}\right] - (i+1).\mu_i\right\}.\frac{v_{p,j}}{(\xi_{\max}-\xi_{\min})}.\left(-\frac{\partial \xi_{\min}}{\partial x_j}\right)
\end{aligned} \tag{5.19}$$

The moments evolution equation, Eq. (5.19), must be coupled with the moving boundary conditions providing the governing equations for $\xi_{\min}(t,x)$. There is also a source term due to the reaction, and $\xi_{\min}(t,x)$ is convected because of the convective particle movement in the presence of spatially inhomogeneous conditions. The definition of the moving boundary conditions for $\xi_{\min}(t,x)$ is based on the evaluation of (a) the spatial derivatives of $\xi_{\min}(t,x)$ and (b) the velocity $v_{p,\min}(t,x)$ of the particles whose densities are equal to $\xi_{\min}(t,x)$.

The moving boundary condition for $\xi_{\min}(t,x)$ is then given by

$$\frac{\partial \xi_{\min}}{\partial t} + \nabla.v_{p,\min}.\xi_{\min} = G \tag{5.20}$$

where G is the growth rate of the particle density due to the reaction defined as (Abbasi et al. 2015)

$$G = \frac{\partial \xi}{\partial t} = (\xi_2 - \xi_1)\frac{\partial X}{\partial t} \tag{5.21}$$

ξ_2 is the density of the product layer (which is higher density), and ξ_1 is the density of the inner core fresh sorbent (which is lower density) as shown in Fig. 5.4. The partial derivative $\frac{\partial X}{\partial t}$ is provided by the heterogeneous reaction kinetic model between CO_2 and the sorbent based on a two-zone variable diffusivity shrinking core model, as described by Eq. (5.16).

The mean density value was calculated based on the ratio of the second moment of the distribution function (Fig. 5.8) to the first moment of the distribution function (μ_1/μ_0).

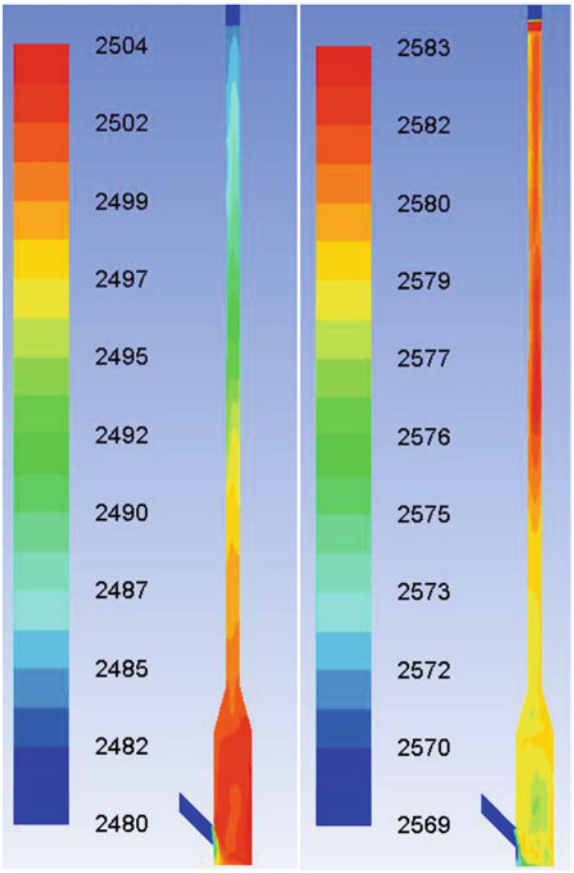

Fig. 5.9 Contours of the time-averaged minimum and mean density of the solid phase at $t = 20$ s (This figure was originally published in *Powder Technol* 286, 2015 and has been reused with permission)

Figure 5.9 shows contours of the time-averaged minimum and mean solid density in the reactor. The minimum density contours of the solid provide valuable information about the location of the fresh sorbent front. Based on Eq. (5.20), the minimum density boundary (fresh sorbent front) moves with the reaction rate, and, because the reaction rate is significantly higher in the lower part of the reactor, the minimum density values rise faster in this region. However, the mean density values, calculated based on the moments of the distribution, are increasing along the height of the reactor.

Although in this specific case the change in the density of the sorbent is not significant and has a very small effect on the hydrodynamics of the system, it can become important in the cases where the sorbent has a significantly higher reaction rate or a higher residence time in a different reactor design.

In addition, the coupled CFD-PBE model is a valuable tool for design and optimization of the reactor and can be useful in the calculation of the regeneration rate and the rate of sorbent make-up to the system. Another application of such a model is studying the effect of particle size distribution on the reactor performance and in the cases in which particle attrition and particle breakage exist.

5.4 Nomenclature

A_s	Overall external particle surface area to unit volume ratio, m^{-1}
C_p	Heat capacity, J/kg·K
C_b	CO_2 concentration in gas, mol/m^3
C_e	Equilibrium CO_2 concentration, mol/m^3
C_i	Concentration at reaction interface, mol/m^3
D_g	Product layer diffusivity, m^2/s
d_p	Particle diameter, m
D_{vg}	Moisture diffusivity of gas phase, m^2/s
D_{vs}	Moisture diffusivity of solid phase, m^2/s
e_{ss}	Particle restitution coefficient
e_{sw}	Restitution coefficient between solid and wall
f	Number density function
$\overline{f}$	Dimensionless number density function
g_0	Radial distribution function at contact during binary collision
h_g	Enthalpy of gas phase per unit mass, J/kg
h_s	Enthalpy of solid phase per unit mass, J/kg
H_{vap}	Heat of vaporization per unit mass, J/kg
k_s	Reaction rate constant, m/s
K_{sg}	Mass transfer coefficient, m/s
m_{sg}	Mass transfer rate, kg/m^3·s
MW	Molecular weight, kg/kmol
$N^o{}_{MgO}$	Initial number of moles of MgO, mol/m^3
Nu	Nusselt number
P_v	Vapor pressure, N/m^2
q	Rate of heat flux, W/K
Q_{sg}	Rate of heat transfer per volume between gas and solid, W/m^3
$\dot{R}$	Rate of carbonation reaction, kmol/kg·s
Re_p	Particle Reynolds number
r_p	Radius of sorbent particle, m
r_c	Radius of unreacted core of sorbent particle, m
Sc	Schmidt number
Sh	Sherwood number
T	Temperature, K
v_g	Gas-phase velocity, m/s
v_p	Particle-phase velocity, m/s
v_s	Solid-phase velocity, m/s
$\vec{v}_{s,para}$	Particle slip velocity parallel to the wall, m/s
X	Sorbent conversion
X_{cr}	Critical moisture content, kg_{water}/kg_{solid}
X_f	Final volume-averaged moisture content, kg_{water}/kg_{solid}
X_s	Volume-averaged moisture content of the solid phase, kg_{water}/kg_{solid}

Y_v Moisture fraction in gas phase
Y_i^* Moisture fraction of saturated drying gas at surface of wet particles

Greek Symbols

ϕ Specularity coefficient between the particle and the wall
μ_i ith moments of density distribution function
α_{gs} Gas–particle heat transfer coefficient, W/m^2·K
ε_k kth phase volume fraction
θ Granular temperature, m^2/s^2
ξ Sorbent density, kg/m^3
ρ_k kth phase density, kg/m^3
τ_k kth phase stress tensor, N/m^2

References

Abbasi E (2013) Computational fluid dynamics and population balance model for simulation of dry sorbent based CO_2 capture process. Doctoral dissertation, Illinois Institute of Technology

Abbasi E, Hassanzadeh A, Abbasian J (2013) Regenerable MgO-based sorbent for high temperature CO_2 removal from syngas: 2. Two-zone variable diffusivity shrinking core model with expanding product layer. Fuel 105:128–134

Abbasi E, Abbasian J, Arastoopour H (2015) CFD–PBE numerical simulation of CO_2 capture using MgO-based sorbent. Powder Technol 286:616–628

Chen YM (2011) Evolution of FCC: past, present, and future-and the challenges of operating a high-temperature CFB system. In: Knowlton TM (ed) Proceeding of the tenth international conference on circulating fluidized beds and fluidization technology, CFB-10, ECI, New York

Extavour M, Bunje P (2016) CCUS: Utilizing CO_2 to reduce emissions. Chem Eng Prog 112.6:55–59

Gunn DJ (1978) Transfer of heat or mass transfer to particles in fixed and fluidized beds. Int J Heat Mass Trans 21:467–476

Jang J, Arastoopour H (2014) CFD simulation of a pharmaceutical bubbling bed drying process at three different scales. Powder Technol 263:14–25

Johnson PC, Jackson R (1987) Frictional collisional constitutive relations for antigranulocytes-materials, with application to plane shearing. J Fluid Mech 176:67–93

Khotari KA (1967) M.Sc. Thesis, Chemical Engineering, Illinois Institute of Technology

Palancz B (1983) A mathematical-model for continuous fluidized-bed drying. Chem Eng Sci 38:1045–1059

Shadle L, Spenik J, Monazam E, et al. (2010) Approach to developing the C2U: a bench-scale carbon capture test unit using supported amine sorbents. NETL CO_2 capture technology meeting, Pittsburgh, PA, 13–17 September 2010. http://www.netl.doe.gov/publications/proceedings/10/co2capture/presentations/monday/Lawrence%20Shadle-ORD.pdf. Accessed 29 June 2016

Sundaresan S (2011) Reflections on mathematical models and simulation of gas-particle flows. In: Knowlton TM (ed) Proceeding of the tenth international conference on circulating fluidized beds and fluidization technology, CFB-10, ECI, New York

Syamlal M, Rogers WA, O'Brien TJ (1993) MFIX documentation, vol 1. Theory Guide, Springfield, VA

Yi CK, Jo SJ, Seo Y et al (2007) Continuous operation of the potassium-based dry sorbent CO_2 capture process with two fluidized-bed reactors. Int J Greenhouse Gas Control 1:31–36

Index

H. Arastoopour et al., *Computational Transport Phenomena of Fluid-Particle Systems*, Mechanical Engineering Series, DOI 10.1007/978-3-319-45490-0